ELECTROMAGNETIC BACKSCATTER MODELLING OF ICEBERGS AT C-BAND IN AN OCEAN ENVIRONMENT

by

© Md. Saimoom Ferdous

A Thesis submitted to the School of Graduate Studies in partial fulfillment of

the requirements for the degree of

Doctor of Philosophy in Electrical Engineering

Memorial University of Newfoundland

May 2020

St. John’s Newfoundland and Labrador

Abstract

This thesis outlines the development of an electromagnetic (EM) backscatter model of icebergs. It is a necessary first step for the generation of in-house synthetic aperture radar (SAR) data of icebergs to support optimum iceberg/ship classifier design. The EM modelling was developed in three stages. At first, an EM backscatter model was developed to generate simulated SAR data chips of iceberg targets at small incidence angles. The model parameters were set to mimic a dual polarized dataset collected at C-Band with the Sentinel-1A satellite. The simulated SAR data chips were compared with signatures and radiometric properties of the satellite data, including total radar cross section (TRCS). A second EM model was developed to mimic the parameters of a second SAR data collection with RADARSAT-2; this second data collection was at larger incidence angles and was fully polarimetric (four channels and interchannel phase). The full polarimetric SAR data allowed for a comparison of modelled TRCS and polarimetric decompositions. Finally, the EM backscatter models were tested in the context of iceberg/ship classification by comparing the performance of various computer vision classifiers using both simulated and real SAR image data of iceberg and vessel targets. This step is critical to check the compatibility of simulated data with the real data, and the ability to mix real and simulated SAR imagery for the generation of skilled classifiers.

An EM backscatter modelling tool called GRECOSAR was used for the modelling work. GRECOSAR includes the ability to generate small scenes of the ocean using Pierson-Moskowitz spectral parameters. It also allows the placement of a 3D target shape into that ocean scene. Therefore, GRECOSAR is very useful for simulating SAR targets, however it can only model single layer scattering from the targets. This was found to be limiting in that EM scattering throughout volume of the iceberg could not be generated. This resulted in EM models that included only surface scattering of the iceberg. In order to generate realistic SAR scenes of icebergs on the ocean, 3D models of icebergs were captured in a series of field programs off the coast of Newfoundland and Labrador, Canada. The 3D models of the icebergs were obtained using a light detection and ranging (LiDAR) and multi-beam sonar data from a specially equipped vessel by a

team of C-CORE. While profiling the iceberg targets, SAR images from satellites were captured for comparison with the simulated SAR images.

The analysis of the real and simulated SAR imagery included comparisons of TRCS, SAR signature morphology and polarimetric decompositions of the targets. In general, these comparisons showed a good consistency between the simulated and real SAR scene. Simulations were also performed with varying target orientation and sea conditions (i.e., wind speed and direction). A wide variability of the TRCS and SAR signature morphology was observed with varying scene parameters.

Icebergs were modelled using a high dielectric constant to mimic melting iceberg surfaces as seen during field work. Given that GRECOSAR could only generate surface backscatter, a mathematical model was developed to quantify the effect of melt water on the amount of surface and volume backscatter that might be expected from the icebergs. It was found that the icebergs in a high state of melt should produce predominantly surface scatter, thus validating the use of GRECOSAR for icebergs in this condition.

Once the simulated SAR targets were validated against the real SAR data collections, a large dataset of simulated SAR chips of ships and icebergs were created specifically for the purpose of target classification. SAR chips were generated at varying imaging parameters and target sizes and passed on to an iceberg/ship classifier. Real and simulated SAR chips were combined in varying quantities (or targets) resulting in a series of different classifiers of varying skill. A good agreement between the classifier's performance was found. This indicates the compatibility of the simulated SAR imagery with this application and provides an indication that the simulated data set captures all the necessary physical properties of icebergs for ship and iceberg classification.

Acknowledgement

First, I would like to express my sincere gratitude to my supervisors in C-CORE, Dr. Peter McGuire and Desmond Power for their generous support, guidance and encouragement throughout my research. The extraordinary leadership, vision and supervision of Dr. Peter and Des always steered me to stay on course and helped overcome obstacles throughout my research. It was possible for me to make it to this level in my PhD journey only because of these two people. My gratitude also goes to my co-supervisor Dr. Thomas Johnson from UBC for supporting and encouraging my research work. He had been mentoring me since I started masters at UBC. I also received guidance and productive discussions from Dr. Michael Collins of University of Calgary. I also thanks Carl Howell for the many discussions on various MATLAB programs. Kelly Dodge, Mark Howell and Pamela Burke helped in data collection, processing and interpretation. All my colleagues at C-CORE were very friendly and inspiring during the four colorful years of my life within that organization. I also thank NSERC (the Natural Sciences and Engineering Research Council) of Canada for funding my research. I am especially grateful to my mother and father, who were the first teachers of my life. They have been selflessly supporting and encouraging to be a good human being and to pursue education and scientific discovery for the betterment of society. My brothers always encouraged and motivated me to excel in my academic affairs. I remember all my near and distant family members and friends who wished me good luck since childhood. To all the teachers in my life including school, college, university and who even taught me a word I am deeply grateful for the invaluable wisdom, philosophy and knowledge you taught. Finally, to my beloved wife Umma Hafsa Himi who was always beside me with much needed inspiration and emotional support.

To all of you, thank you so much.

Table of Contents

List of Tables

List of Figures

List of Abbreviation

Abbreviation	Meaning	First appearance (page number)
3D	Three dimensional	7
AUC	Area Under Curve	86
CAD	Computer Aided Design	13
CP	Compact Polarimetry	2
dBsm	dB per square meter	30
DP	Dual-pol	2
DRDC	Defense Research and Development Canada	4
ESA	European Space Agency	18
EM	Electromagnetic	1
FQ	Fine Quad	40
GPS	Global Positioning System	19
HH	Horizontal sent, horizontal received	4

HV	Horizontal sent, vertical received	4
IEM	Integral Equation Method	5
IW	Interferometric Wide	13
kNN	k-Nearest Neighbor	14
LiDAR	Light Detection and Ranging	11
LOS	Line of Sight	60
MH	Multi-harmonic	17
MURF	Multi-User Request Form	70
NESZ	Noise Equivalent Sigma Zero	5
NN	Neural Net	14
PO	Physical optics	7
PPT	Parts Per Thousand	27
PSU	Practical Salinity Unit	49
QP	Quad-pol	2
RADAR	Radio Detection and Ranging	1
RMS	Root Mean Square	56
ROC	Receiver Operating Characteristic	4
RT	Ray tracing	7
RTM	Radiative Transfer Model	64
SAR	Synthetic Aperture Radar	1
SLC	Single look complex	17
SP	Single-pol	2
SVM	Support Vector Machine	14

TRCS	Total Radar Cross Section	8
VH	Vertical sent, horizontal received	4
VV	Vertical sent, Vertical received	4

List of Symbols

Symbol (unit)	Description	First appearance (page number)
θ (˚)	Look angle	22
θ (˚)	Incidence angle	63
Fc (GHz)	Centre frequency	18
h (m)	Height of the satellite	45
h_s (m)	Significant wave height	22
$\overline{y}_{n,m}$ (m)	Height of each wave components	23
S_z (m^2/Hz)	Wave spectral density	23
ω (rad/s)	Wave components in the wave spectral density	23
k_n(rad/m)	Wave number	23
χ_m(˚)	Propagation directions in the wave spectral density	23
R (m)	Ground range	45
T (sec)	Average wave period	22
β (˚)	Target orientation in degree (measured from -X axis clockwise direction)	22

m (--)	Ocean clutter mean	28
σ (--)	Standard deviation of the ocean clutter	28
σ_0 (--)	Ground range intensity	18
ΔA (m^2)	Pixel area	30
δf(MHz)	Bandwidth	18
F_s (MHz)	Sampling rate	18
τ (μs)	Pulse width	18
φ ($^\circ$)	Incidence angle	18
ϕ ($^\circ$)	Wind direction	55
λ_{creep}(m)	Creeping wavelength	25
λ_{sensor}(m)	Sensor wavelength	25
σ_{xy}^0 (dB)	Scattering from x=water/ice/sea medium, y=surface/volume component	62
k (rad/m)	Wave number in the incident medium	63
σ (m)	rms height of the rough surface	63
ε_r	Relative permittivity	63
R_X	Fresnel reflection coefficient (x= vertical/horizontal polarization)	63
L (m)	Correlation length of a rough surface	64
T_{xyz}	Transmission coefficient between medium *x* and *y* and *z*=direction between medium	64
β_{xe} (m^{-1})	Extinction coefficient composed of absorption and scattering coefficient	64
n (m^{-3})	Air bubble density	65

ρ_{am} (m)	Range-ambiguous distance	65
r (m)	Radius of air bubble	65
d (m)	Thickness of a medium	66

Chapter 1 Introduction and Overview

1.1 Background

Climate change has increased the sea-ice free window in the Arctic, opening the opportunities for increased marine transportation and resource exploration activities. Arctic regions are also frequented by sea ice, thus increasing the need for effective and frequent iceberg charting. In the context of scientific research, global iceberg monitoring is important; climate change has effected an increase in iceberg calving relates and therefore, knowledge of iceberg populations help in the development of long-term weather models (Bigg, Wadley, Stevens, & Johnson, 1997). To safeguard offshore assets and human mobility, it is important to robustly monitor iceberg targets and predict their trajectory and fate in advance so that preventive measures – iceberg management – can be carried out. Technology based solutions now exist to help improve and advance effective iceberg surveillance strategies. The Arctic and Antarctic are subject to frequent inclement weather, dark polar nights and excessive cloud cover. In this context, radio detection and ranging (RADAR) is generally the preferred choice for iceberg monitoring. Specifically, satellite synthetic aperture radar (SAR) has become the defacto choice for Polar ice monitoring and is quickly becoming the preferred technology for routine iceberg monitoring (Power, Youden, Lane, Randell, & Flett, 2001). The last decade has seen an onslaught of new SAR missions, and Polar Regions now enjoy daily – or better – coverage with wide swath SAR imagery.

Satellite based SARs generally operate at single wavelength and fall into many different bands, including P-Band (100-30 cm), L-band (15-30 cm), S-Band (7.5-30 cm), C-band (3.75-7.5 cm) and X-band (2.4-3.75 cm). Presently, there are satellite SARs being developed at higher frequencies (e.g., Ku Band), and missions that can transmit multiple radar wavelengths. Unlike satellite based optical systems (e.g., SPOT, Landsat, MODIS, Sentinel-2, others), SAR is all weather and can image day or night. SAR wavelengths are long enough to be only slightly influenced by atmosphere and penetrate through rain, fog and clouds. SAR also offers polarization diversity. Electromagnetic (EM) radiation reflected from an object is polarized and carries polarimetric information of the object that offers clues regarding the object's physical composition

(i.e., geometry, shape and dielectric properties). A SAR that transmits and receives in a single polarization is called single-pol (SP) SAR. A SAR that transmits single polarization and receives two orthogonal polarization signals is called dual-pol (DP) SAR. A quad-pol (QP) SAR transmits and receives two orthogonal polarizations. The quad-pol system contains full polarimetric information of an object but generally covers less swath width than comparable dual pol systems. So, while QP SARs have a better ability to classify an object based on polarimetry, they are less practical than SP or DP SAR, especially for applications like maritime surveillance requiring frequent and broad area coverage. A compromise between traditional DP and QP SARs is a specific variant of dual polarization that transmits and/or receives a combination of circular, elliptical and linear polarizations. These SARs are called compact polarimetry (CP) and offer the same swath coverage as traditional DP SARs, while having polarimetric capabilities that approach QP SARs. CP is thus a very attractive feature for maritime surveillance and a myriad of applications including ship detection (Atteia & Collins, 2013) , crop condition monitoring (McNairn et al., 2017), oil spill detection (Yin, Yang, Zhou, & Song, 2014), wetland mapping (Mahdianpari, Salehi, Mohammadimanesh, & Brisco, 2017) and sea-ice classification (Geldsetzer et al., 2015). As of the writing of this thesis, there is only one operating satellite – RADARSAT Constellation Mission – that has a working CP mode; nonetheless, other missions are being developed (e.g., the next generation of Cosmo SkyMed and TerraSAR-X satellites) that include this capability.

One of the primary challenges for SAR data-based ocean surveillance in ice-frequented waters is the discrimination of vessel targets from icebergs (Power, Bobby, Howell, Ralph, & Randell, 2011). In the context of iceberg surveillance, vessel targets are considered false alarms and the same is true for icebergs in vessel monitoring applications. The present state of the art in SAR-based vessel and iceberg discrimination is the use of machine learning to train algorithms to distinguish between vessel and iceberg backscatter. Machine learning requires the use of large validated datasets of iceberg and vessel targets. Given the inclement polar weather, the collection of ground truthed iceberg targets can be quite challenging, costly and time consuming. Some Polar Regions are simply inaccessible in a practical sense. In spite of

this, there is a recent instance where over 5000 validated iceberg/ship data were made available for an internet-based computer vision competition, sponsored by C-CORE and Statoil (now Equinor).[1] Although large, this dataset still lacks the ability to provide information of how an iceberg's SAR response could vary with the sea state, satellite parameters and target orientation. One potential solution to the problem is the use of physically-based EM backscatter modelling of iceberg and ship targets in SAR data. The availability of such models could prove to be a crucial and important step in developing in house simulated SAR datasets and should help develop robust iceberg and ship classification algorithms. In addition to the classification application, simulated SAR images of icebergs would be highly beneficial to quantify detectable ranges of sea states for various berg sizes to allow for an optimization of beam mode selection for robust iceberg detection. This thesis will present the effort to date in the development of an EM backscatter model of iceberg targets in an ocean environment.

1.2 Relevant Literature

1.2.1 Iceberg Surveillance with SAR

Iceberg location and movement have long been monitored by radar technology – more specifically SAR – as it can see through the harsh weather, dark polar nights and excessive cloud cover in Arctic and Antarctic regions (Power et al., 2001). This has been a common practise by governments and industry to monitor iceberg locations in ice frequented waters (Randell, Freeman, Power, & Stuckey, 2009). In the literature, few studies have been found on iceberg detection with SAR, perhaps because only a few countries are affected by the presence of icebergs. Early studies of iceberg detection in SP SAR involved isolating clusters of bright pixels (e.g., icebergs) from background dark pixels (e.g., clutter) by a histogram method followed by ad hoc processing steps (Murthy & Haykin, 1987; Orlando, Mann, & Haykin, 1990). Drawbacks of this method include the fact that the histogram highly varies with ocean conditions and target

1 https://www.kaggle.com/c/statoil-IB-classifier-challenge

response can become indistinguishable between different target types. Howell et al. (2004; 2006; 2008) proposed a likelihood ratio based detector method based on work conducted by Defence Research and Development Canada (DRDC) (Liu, C., Vachon, & Geling, 2005) to detect targets (icebergs and ships) followed by a classification algorithm to separate icebergs from ships. The success rate of this method is dependent on selecting the right features, which is sometimes challenging as there could be many intrinsic features that are not necessarily captured by machine learning based approaches. Howell et al. (2008) first compared iceberg/ship classification performances among SP RADARSAT-1 (HH), DP ENVISAT (HH/HV) and QP (HH/HV/VH/VV) airborne EMISAR data. Howell indicated the utility of having multi-pol data for improved iceberg/ship classification performance. In Howell et al. (2012), a more comprehensive study on target detection and classification of vessels and icebergs based on the combinations of polarimetric SAR data was performed by the same team at C-CORE. Detection performance was evaluated using a receiver operating characteristic (ROC) curve and vessel and iceberg discrimination was achieved using a quadrature multivariate feature discriminator that extracts feature vectors from target pixels. Results suggested that the HH-HV combination of DP SAR has maximum potential for vessel/iceberg discrimination, with the HV channel appearing to be more important in many scenarios. Furthermore, it was shown that the QP data performs best in the context of detection and discrimination although for maritime surveillance QP data is fairly limited because of the narrow swath width of existing satellites (e.g., RADARSAT-2). As suggested earlier, CP offers a trade off between QP and DP. Denbina and Collins (2012) published a comparative study between DP and simulated CP data for iceberg detection. Since there were no CP satellites at the time of publication, CP data were simulated from RADARSAT-2 QP data, by combining various channels and resampling the data. This study confirmed the importance of the HV channel and demonstrated that CP data outperforms all linear DP configurations. Ultimately, this research showed the potential for CP in iceberg detection and classification as it overcomes the swath width limitation of QP modes. The utility of the HV channel has been shown by other authors for iceberg detection, including Wesche & Dierking (2012). They found that RADARSAT-2 data performed

better for iceberg detection than RADARSAT-1 and ENVISAT primarily because of the availability of the cross-pol channel (HV or VH) with a suitably low noise equivalent sigma zero (NESZ).

Other authors have also made suggestions about the performance of various polarizations for target detection; most of this work has been conducted in the context of ship detection. In general, HH channel has been found to be better than VV, due to the slightly elevated sea clutter levels of the latter relative to HH (Vachon, PW, Campbell, Bjerkelund, Dobson, & Rey, 1997). This is because of the difference in the Fresnel reflection coefficients for horizontal and vertical directions in the integral equation method (IEM) for ocean surface (Ulaby et al., 2014). On the other hand, HV has better signal to clutter ratio than HH in low incidence angles (Touzi, Charbonneau, Hawkins, & Vachon, 2004). Higher incidence angles are suggested for better detection as less clutter is generated than the low incidence angles (Vachon, Paris W. & Wolfe, 2011).

In terms of the sensor wavelength, to date, iceberg detection has mostly been performed with C-band SAR because of the data availability and government and industry practise; nonetheless, there are some notable examples of X-band iceberg surveillance. Representative examples of iceberg detection research include Akbari & Brekke (2018), Dierking & Wesche (2014) and Kim, Kim, Kim & Hwang (2011).

SAR is extensively used for vessel surveillance as the applications are very similar, involving the detection of bright backscatter on a clutter background. As the list of publications available on SAR-based ship detection is rather extensive, the focus here is on more recent publications that involve some aspect of multi-pol detection of discrimination. For example, Crisp (2004) suggested that DP SAR data provides better performance than SP data while providing greater swath coverage than QP data. Unsurprisingly, this mirrors the conclusions made with iceberg detection. C-CORE, in a series of publications between 2004 and 2012 investigated the use of DP SAR for maritime surveillance (C-CORE, 2012; Howell et al., 2004; Howell et al., 2006; Howell, 2008). Ship detection algorithms have been published for both DP and QP data (see for example Brekke & Anfinsen (2011) and Wang, Li, Zhang, & Guo (Wang, Li, Zhang, & Guo,

2015)). The paper by Brekke & Anfinsen (2011) is one of the few that discusses ship detection in ice prone waters. In terms of CP use in ship detection, a few representative papers include Atteia & Collins (2013), Shirvany, Chabert, & Tourneret (2012), and Yin, Yang, & Zhang (2011). Shirvany et al., (2012) compared CP to several DP configurations and found that the ship detection performed better for CP configuration than DP. Liu et al., (2010) at DRDC showed that CP outperforms DP configurations in ship detection. However, this study used data of much higher resolution than is typically used operationally and the effect of incidence angle and sea states were not discussed. Later, researchers from C-CORE addressed the issue of resolution (C-CORE, 2012) by resampling the data to simulate lower resolution modes of RADARSAT-2 and compared these results to ENVISAT ASAR data. SAR-based ship detection has been performed at several frequencies, and most commonly include C-Band and X-Band. Some representative publications include C-band RADARSAT-1 (Meyer & Hinz, 2009), ENVISAT ASAR (Tello, López-Martínez, Mallorquí, & Greidanus, 2005), RADARSAT-2 (Marino, Walker, & Woodhouse, 2010), X-band TerraSAR-X (Marino & Walker, 2011; Marino & Hajnsek, 2012) and X-Band COSMO-SkyMed (Pastina, Fico, & Lombardo, 2011).

The present state of the art in SAR-based vessel and iceberg discrimination is the use of machine learning to train algorithms to distinguish between vessel and iceberg backscatter (see, for example (C-CORE, 2012; C-CORE, 2016; Howell et al., 2004; Howell et al., 2006; Howell, 2008; Howell, Bobby, Power, Randell, & Parsons, 2012)). Several of the authors have been involved in efforts to develop ship and iceberg classifiers in different types of SAR imagery, starting initially with RADARSAT-1 (unpublished) and then to ENVISAT ASAR (Howell et al., 2004; Howell et al., 2006), RADARSAT-2 (C-CORE, 2012; Howell, 2008) and TerraSAR-X (Howell et al., 2012). Recent efforts (C-CORE, 2016) deal with discriminators trained for simulated data from the RADARSAT Constellation Mission[2], showing the benefits of compact

[2] Simulated RCM data were produced from RADARSAT-2 QP data with a program from the Canada Centre for Mapping and Earth Observation.

polarimetry for target discrimination. In 2017, iceberg/ship classifiers' performances were reported (Jun, Atharva, & Dhruv, 2017) based on the Kaggle competition[3] data. In generating abound training data to train machine learning based classifiers, synthetic image data of targets were generated by simple image rotation and scaling. While this might be reasonable to do for the targets with static background whose signature would not vary as the look direction changes, this might not be reasonable as the dynamics of iceberg/ship and water interaction changes a lot with look direction and sea states, producing different SAR signatures.

1.2.2 EM Backscatter Modelling of Icebergs

Although EM tools are used quite frequently to model the backscatter of various objects, their use to model EM backscatter from marine targets is not quite frequently reported in literature. Gerard et al. (2006), reported a simulation tool called 'GRECOSAR' to model EM backscatter from vessel targets. The tool has the capability of producing simulated SAR images of complex targets from varying satellite parameters, target orientations and imaging scenes with a full polarimetric capability. The tool uses an EM solver called Graphical Electromagnetic Computing (GRECO) developed at the Universitat Politecnica de Catalunya Apdo in Barcelona. The EM solver calculates backscatter from the target in 3D environment by using physical optics (PO) and ray-tracing (RT) theory and handles multiple scattering, curvature and shadowing effect (Margarit et al., 2006) from complex environments. GRECOSAR allows the simulation of a variety of satellite SAR modes using input parameters of the SAR to produce the required ground resolution and radiometric dynamic range. The functionality of the software has been rigorously tested and verified by comparing radar backscatter generated from standard canonical objects (sphere, dihedral and trihedral) with reported theoretical values (Margarit et al., 2006). GRECOSAR accounts for single layer propagation and backscatter from any object and has been extensively used for the high dielectric objects like marine targets (ships) (Margarit, G., Mallorqui, & Fabregas, 2007; Margarit, G. & Mallorqui, 2008; Margarit et al., 2006;

[3] https://www.kaggle.com/c/statoil-iceberg-classifier-challenge

Margarit, Gerard, Mallorqui, & Fabregas, 2007; Margarit, Gerard & Mallorquí, 2008; Margarit, Gerard, Mallorqui, Fortuny-Guasch, & Lopez-Martinez, 2009; Margarit, Gerard & Tabasco, 2011) and for urban scattering (Margarit, Gerard, Mallorqui, & Lopez-Martinez, 2007). GRECOSAR has not been used to address backscatter coming from low permittivity dielectrics, such as the glacial ice within an iceberg. Furthermore, the single layer limitation of GRECOSAR implies that the simulation of complicated multilayer propagation and backscatter is not possible. Depending on the frequency, microwaves are known to penetrate to a significant depth into cold glacial ice, resulting in both surface and volume backscatter (Haykin, Lewis, Raney, & Rossiter, 1994). A mismatch in the dielectric values of air and glacial ice results in almost 10% incident energy back to the sensor, contributing to the surface scattering. The rest of the microwave energy penetrates through the berg and dissipates in the form of absorption and scattering loss. Gray et al. in (1991) showed in a field experiment that the absorption loss at X-band is 10 times higher than that of L-band. For the scattering loss, X-band loss is almost 4000 times higher than that of L-band. Penetration depth of a heterogeneous medium constitutes from the absorption (medium loss factor, ε'') and scattering loss (impurities in the medium). Currie et al. (1987) mentioned that the penetration depth of C-band wave in iceberg medium varies between 3 to 14 m depending on the properties of the bergs. This variation arises from the fact that, the absorption loss in the firn of iceberg is a function of ice temperature and a variation of 53 dB/100 m length was found over 18˚ temperature change (Dierking & Wesche, 2014). Dierking et al. (2014) also observed a 1-6 dB/100 m variation for scattering loss (volume scattering) in the Antarctic iceberg and the absorption loss is almost 5 times higher than scattering loss.

This research documented in this thesis attempts to develop an EM model of an iceberg with the help of GRECOSAR which would be pivotal in understanding and quantifying iceberg backscatter for a variety of sensor parameters, environmental conditions and imaging modes and help in producing ground truth iceberg image data in designing more robust iceberg/vessel classifier, thus filling this gap in the literature. The research has been conducted while accounting for the limitations of GRECOSAR and its ability to model only single layer propagation and backscatter.

1.3 Research Objective

The main objective of the research documented herein is to develop an EM backscatter model of low dielectric targets such as icebergs while accounting for the limitations of the GRECOSAR simulation tool. In addressing these objectives, the following steps are followed:

1. Ocean model parameters are explored in GRECOSAR to produce the realistic ocean backscatter.
2. The dielectric permittivity of 3D iceberg profiles embedded within an ocean patch is adjusted within GRECOSAR to match with real iceberg backscattering properties, including total radar cross section (TRCS), radar morphological signature and polarimetry properties. Efforts were made to match the geometrical orientation and surrounding sea states of the in-field iceberg observations, as these are shown to alter the backscattering properties of iceberg targets.
3. Modelling is performed in GRECOSAR to assess backscattering properties of both low and high incidence angles.
4. To support the validity of the GRECOSAR model, a multi-layer mathematical model of glacial iceberg is explored. This model accounts for the various layers of glacial ice, including a surface melt layer that was observed during an iceberg field campaign. The impact that this melt layer has on the total radar backscatter is explored and elaborated. The modelling shows that actively melting icebergs may be realistically modelled in GRECOSAR given the single layer limitations within this modelling software.
5. Once the basic EM properties of icebergs in GRECOSAR are validated, GRECOSAR is then used to produce a set of simulated SAR iceberg and ship targets of various sizes, geometrical and environmental surroundings for use within machine learning classifiers. The compatibility of these simulated SAR image chips with real SAR targets is confirmed for use within a ship and iceberg target classifier application. A ‘chip’ refers to a square patch or sub-image of the SAR imaging area.

1.4 Chapters Overview

The thesis has been divided into five chapters, including this introduction. A chapter summery is given below:

- Chapter 2 is titled EM Backscatter Modelling of Icebergs at Large Incidence Angles using Dual Polarization Radar Modes. This chapter constitutes the paper published in 2018 in the Canadian Journal of Remote Sensing as: Ferdous, M. S., McGuire, P., Power, D., Johnson, T., & Collins, M. (2018). A comparison of numerically modelled iceberg backscatter signatures with sentinel-1 C-band synthetic aperture radar acquisitions. *Canadian Journal of Remote Sensing*, *44*(3), 232-242.
- Chapter 3 is titled EM Backscatter Modelling of Iceberg at Small Incidence Angles using Quad Polarization Radar Modes. This chapter constitutes the paper, published in the Journal of Selected Topics in Applied Earth Observations and Remote Sensing as: M. S. Ferdous, U. H. Himi, P. McGuire, D. T. Power, T. Johnson and M. J. Collins, "C-Band Simulations of Melting Icebergs Using GRECOSAR and an EM Model: Varying Wind Conditions at Lower Beam Mode," in *IEEE Journal of Selected Topics in Applied Earth Observations and Remote Sensing*, vol. 12, no. 12, pp. 5134-5146, Dec. 2019.
- Chapter 4 is titled Assessing the Utility of Modelled SAR Images of Iceberg and Ship Targets using a Machine Learning Classifiers. It constitutes the paper published in 2019 in the IEEE Geoscience and Remote Sensing Letters as: Ferdous, M. S., Himi, U. H., McGuire, P., Power, D., Johnson, T., & Collins, M. (2019). Assessing the usefulness of iceberg electromagnetic backscatter modeling using a C-band SAR classifier. *IEEE Geoscience and Remote Sensing Letters, Early access*, 1-5. doi:10.1109/LGRS.2019.2944432.

Basic summaries of the chapters are outlined below.

1.4.1 Chapter 2

The research started by looking at the aspects of EM backscatter modelling of icebergs using GRECOSAR. The available dataset was from DP Sentinel-1 collected at large incidence angles that included complementary 3D profiles of icebergs. Limitations in generating the iceberg backscatter model in GRECOSAR were identified and necessary assumptions were made to account for the limitations. GRECOSAR can only simulate single layer propagation from a surface whereas multilayer propagation and backscatter is possible from the large volume of an iceberg. Icebergs are of freshwater origin and have many discontinuities such as trapped air pockets, giving rise to the potential for significant backscatter through its volume. The permittivity of the iceberg surface was adjusted from low to high to mimic, respectively, cold and freshly calved icebergs seen in the high Arctic and the wet, actively melting surface of icebergs seen further south. The latter condition was assumed for the icebergs that were ground truthed during a complementary field program conducted by C-CORE in 2015 and 2017, given that field personnel witnessed significant melt conditions on all the icebergs that were profiled. EM simulation parameters were chosen to mimic the field program conditions. Simulation results were measured and compared in terms of SAR target morphological signature and radiometric properties, including TRCS.

Backscatter models for icebergs are developed for this paper using GRECOSAR and compared with ground truth data. The imaging scene consists of iceberg targets surrounded by the ocean surface. The 3D profiles of the icebergs were obtained using LiDAR and multi-beam sonar data mounted on a vessel by a team of C-CORE. These data were collected during a field program off the coast of Salvage, Newfoundland and Labrador, Canada. While profiling the iceberg targets, a SAR image from Sentinel-1 was captured and used as the basis for comparison to the simulated SAR images. Comparisons made in terms of TRCS and the SAR signature of the targets generally indicate realistic simulations. Simulated SAR images were generated at low and high dielectric conditions to mimic cold and melting icebergs. Variability of the TRCS and morphology as a function of target orientation highlights the usefulness of EM modelling in developing a large database of targets that mimic real world situations.

1.4.2 Chapter 3

In the next phase of the research, fully polarimetric (QP) RADARSAT-2 image data were collected at a low incidence angle beam mode during a second iceberg field campaign. Using these data, the polarimetric characteristics of the GRECOSAR simulated iceberg SAR data are explored. In addition to the polarimetric response, the SAR morphological signatures and radiometric properties are also evaluated.

The SAR response investigation is supplemented in this chapter with an analysis of SAR signature variability over various ocean parameters such as wind speeds and directions. As in the previous chapter, 3D profiles of three icebergs were captured in a field study to facilitate the EM modelling; these profiles were captured off the coast of Bonavista, Newfoundland and Labrador, Canada in June, 2017 at the same time of the RADARSAT-2 satellite overpass. The SAR image and 3D profiles were captured within hours of one another. Simulated SAR images of the icebergs were generated in GRECOSAR with the satellite, target orientation and ocean parameters that closely mimic the real SAR scene. A comparison between real and simulated SAR images of the icebergs shows good agreement in terms of SAR morphological signature, TCRS and polarimetric decomposition. Wind direction was varied over 90˚ to observe the level of backscatter variability of the icebergs in the simulated images. Furthermore, simulated SAR images were generated for low and high wind conditions. This study finds that the macro structure of the iceberg dominates its polarimetric behavior. The study also shows a large variability of iceberg SAR signature over varying ocean parameters. This aspect is very important when considering the design of iceberg classification algorithms. Specifically, it points to a need to collect a large quantity of iceberg images over a large variety of meteorological conditions and a large number of incidence angles and orientations in order to completely characterise an iceberg. This is a very important conclusion when considering the collection of a dataset for use in iceberg classification, computer vision and machine learning.

In support of the melt water surface assumption presented in chapter 2, a 2D mathematical model is presented to estimate to what extent the melt water layer will contribute to the backscatter. That

mathematical model considers backscatter contributions at various interfaces of the iceberg, including the air to meltwater interface, meltwater to ice interface and ice to ocean interface (at the iceberg bottom). The analysis shows that the melting condition of iceberg presents a significant backscattering interface that reflects a predominant proportion of the incidence microwave radiation from the SAR. The analysis also shows that the melt water layer can be as little as 0.1 mm to produce a dominant radar response relative to other scattering surfaces on a berg. Thus, the mathematical model independently supports the validity of the GRECOSAR EM simulations.

1.4.3 Chapter 4

In the previous two chapters, EM backscatter models of icebergs were presented and compared in terms of handpicked radiometric and polarimetric properties. These models are developed through a very limited range of satellite parameters, presenting only a small and large incidence angle condition. It is clear that there are more intrinsic properties of the SAR that need analysis. However, the availability of SAR ground truthing limits that analysis. Nonetheless, the EM simulation allows for the development of a large variety of iceberg targets in many different conditions. One way to perform a more detailed comparison for the larger range of SAR parameters is to perform an indirect comparison of simulated SAR images to actual SAR targets comprising that larger range of parameters. In this case, the indirect comparison is made by combining simulated SAR images with a large collection of real SAR targets in a machine learning application. The application chosen here is a SAR-based ship and iceberg classifier.

To perform this indirect comparison, simulated SAR image data were obtained from GRECOSAR in combinations of imaging beam modes and scene parameters to produce a total of 216 simulated SAR images. A very large dataset of ship and iceberg targets from the Sentinel-1 C-Band satellite was made available thanks to a deep learning competition sponsored by C-CORE and Equinor on the Kaggle platform. In this dataset, over 5000 target chips were collected at the Interferometric Wide Swath (IW) mode, with HH and HV polarizations. Parameters of the GRECOSAR simulations consisted of Sentinel-1 IW1 (33.1°)

and IW3 (43.1°) beam mode, wind speeds of 5 and 10 m/s, wind directions of 0°, 45° and 90° (measured clock wise (CW) with respect to range direction) and target orientations of 0°, 45° and 90° (measured CW with respect to azimuth direction). Simulations were performed in GRECOSAR using 3D profiles of icebergs and computer aided design (CAD) models of ships. The idea was to mimic the real SAR scenes as closely as possible. The iceberg profiles used here were the same ones used in chapter 3 that were collected off the coast of Bonavista in June 2017. Three ship CAD models were sourced from an online inventory and scaled to the sizes of iceberg targets. Classifiers, including state vector machines (SVM), random forest, k-nearest neighbour (kNN) and neural net (NN), were trained with simulated SAR data and then gradual mixed with real SAR data. Similar performances of the mixed and real-data only classifiers are observed. The similarity of the different classifiers indicates the compatibility of the GRECOSAR simulated data for this application. Thus, it indicates that the simulated SAR data captures the necessary physical parameters of the iceberg/ship targets for SAR target classification.

1.4.4 Chapter 5

Chapter 5 is the concluding part of the thesis. It has been segmented into two parts. The first part compares research objectives with accomplishments as described in chapter 1. In the second part, future research directions have been suggested based on the accomplishments of this research.

Co-authorship Statement

The principal author of the published papers containing the techniques and results reported in this thesis contributed primarily in the design and identification of the research proposal and the resulting research. The supervisory team helped in reviewing the research proposal and the output research. Practical aspects of the research identified by the principal author were discussed with supervisors. Data analysis and interpretation was primarily conducted by the principal author and reviewed by the supervisory team. In preparing this manuscript and the papers that comprise the various chapters, the principal author organised and composed the drafts that were reviewed and approved by the supervisors.

Chapter 2 EM Backscatter Modelling of Icebergs at Large Incidence Angles using Dual Polarization Radar Modes

2.1 Introduction

Safe offshore operations and navigation in ice-prone waters require reliable surveillance of icebergs. Iceberg monitoring is of interest in the scientific context as well. Increase in iceberg calving relates to global warming and helps predict long-term climate change (Bigg, Wadley, Stevens, & Johnson, 1997). In the context of the Arctic and Antarctic, harsh weather, dark polar nights and excessive cloud cover in summer implies that radar and more specifically SAR – is generally the preferred choice for ice monitoring(Power, Youden, Lane, Randell, & Flett, 2001) . SAR is widely used by governments and industry to monitor iceberg locations in ice-frequented waters (Randell, Freeman, Power, & Stuckey, 2009). SAR is also used extensively for vessel surveillance, as the applications are very similar, involving the detection of bright backscatter on a clutter background. Some representative publications of SAR-based ship detection include C-band RADARSAT-1 (Meyer & Hinz, 2009), ENVISAT ASAR (Tello, López-Martínez, Mallorquí, & Greidanus, 2005), RADARSAT-2 (Marino, Walker, & Woodhouse, 2010), X-band TerraSAR-X (Marino & Walker, 2011; Marino & Hajnsek, 2012) and X-Band COSMO-SkyMed (Pastina, Fico, & Lombardo, 2011). To date, iceberg detection has been performed mostly with C-band SAR because of the data availability and government and industry practise; nonetheless, there are some notable examples of X-band iceberg surveillance. Representative examples of iceberg detection research include (Akbari & Brekke, 2017; Akbari & Brekke, 2018; Dierking & Wesche, 2014; Kim, Kim, Kim, & Hwang, 2011). RADARSAT-2 data performed better for iceberg detection than RADARSAT-1 and ENVISAT (Wesche & Dierking, 2012), primarily because of the availability of a cross pol channel (HV or VH) with a suitably low NESZ. In general, HH channel is better than VV, due to the slightly elevated sea clutter levels relative to HH (Vachon, PW, Campbell, Bjerkelund, Dobson, & Rey, 1997). On the other hand, HV has better signal to clutter ratio than HH in low incidence angles (Touzi, Charbonneau, Hawkins, & Vachon, 2004). Higher incidence angles are suggested for better detection as less clutter is generated than the low incidence angles (Vachon, Paris W. & Wolfe, 2011).

In the context of ocean surveillance in ice frequented waters, one of the primary challenges in using SAR data is the discrimination of vessel targets from icebergs (Power et al., 2001). In the context of iceberg surveillance, vessel targets are considered false alarms and the same is true for icebergs in vessel monitoring applications. The present state of the art in SAR-based vessel and iceberg discrimination is the use of machine learning to train algorithms to distinguish between vessel and iceberg backscatter (see, for example (Bentes, Frost, Velotto, & Tings, 2016; C-CORE, 2012; C-CORE, 2016; Howell et al., 2004; Howell et al., 2006; Howell, 2008; Howell, Bobby, Power, Randell, & Parsons, 2012)). Several of the authors have been involved in efforts to develop ship and iceberg classifiers in different types of SAR imagery, starting initially with RADARSAT-1 (unpublished) and then expanding to ENVISAT ASAR (Howell et al., 2004; Howell et al., 2006), RADARSAT-2 (C-CORE, 2016; Howell, 2008) and TerraSAR-X (Howell et al., 2012). The most recent efforts (C-CORE, 2016) deal with discriminators trained for simulated data from the RADARSAT Constellation Mission, showing the benefits of compact polarimetry for target discrimination.

Machine learning requires the use of large validated datasets for iceberg and vessel targets, which can be costly and time consuming to collect. For example, an internet-based computer vision competition, sponsored by C-CORE and Statoil, used over 5000 validated targets as training and testing datasets. One solution to the problem is the use of a physically based EM backscatter modelling of iceberg and ship targets in SAR data. The availability of such models could prove to be a crucial and important step in developing a robust iceberg/ship classification algorithm.

GRECOSAR was used for the EM modelling work (Margarit, Gerard, Mallorqui, Rius, & Sanz-Marcos, 2006). The functionality of the software has been rigorously tested and verified by comparing radar backscatter generated from standard canonical objects (sphere, dihedral and trihedral) with reported theoretical values (Margarit et al., 2006); these results have been reproduced by the authors. Use of GRECOSAR for the detection and classification of marine targets (ships) (Margarit, G., Mallorqui, &

Fabregas, 2007; Margarit, G. & Mallorqui, 2008; Margarit, Gerard, Mallorqui, & Fabregas, 2006; Margarit et al., 2006; Margarit, Gerard, Mallorqui, & Fabregas, 2007; Margarit, Gerard & Mallorquí, 2008; Margarit, Gerard & Mallorqui, 2008; Margarit, Gerard, Mallorqui, Fortuny-Guasch, & Lopez-Martinez, 2009; Margarit, Gerard & Tabasco, 2011) and for urban scattering (Margarit, Gerard, Mallorqui, & Lopez-Martinez, 2007) have been reported extensively. GRECOSAR uses a multi-harmonic (MH) sea model to modulate sea waves and the sea model has been validated in other published work (Yam, Mallorqui, & Rius, 2012).

The main objective of this work is to present an EM backscatter model of icebergs using GRECOSAR at a satellite's higher incidence angle beam mode and to compare with DP SAR data. The rest of the chapter includes the following sections: "Materials and Methods", "Results and Discussions" and finally "Conclusion". "Material and Methods" describes first, how SAR images containing three target icebergs were captured and how corresponding 3D profiling of the icebergs were measured in a field program off the coast of Salvage, NL. This is followed by the description of wide ranges simulation parameters and a selection and a thresholding based de-clutter technique to mask iceberg target pixels from ocean clutter in a SAR image. In the "Results and Discussions" section simulated and real SAR images of the iceberg targets were compared in terms of morphology of the target signatures and TRCS. A further simulation result is presented to show the variability of the TRCS of the icebergs over orientations to the satellite. The "Conclusions" sums up the article in terms of objectives and the result found and provides future directions of this work.

2.2 Materials and Methods

2.2.1 Field Data

2.2.1.1 SAR Image Acquisition and 3D Model Profiling

A SAR image containing icebergs off the coast of Salvage, NL, Canada was captured on 7 July 2015 at 1423 UTC with Sentinel-1 sensor. The SAR image mode was IW mode in DP single look complex (SLC)

format with 3 sub-swaths. The image is then de-burst and calibrated with European Space Agency (ESA)-made SNAP software (ESA's open source software to process Sentinel images) to ground range intensity (σ_0) format to comply with the GRECOSAR-generated SAR image format as shown in Figure 2.1. It is the amount of backscatter return per unit area of an object to the antenna. Satellite parameters representing the IW3 mode of the Sentinel-1 satellite are presented in Table 2.1.

Table 2.1 Sentinel-1 satellite parameters.

Parameter	Value	Parameter	Value
Incidence angle, φ ($^{\circ}$)	43	Pulse width, τ (μs)	53.4
Centre frequency, Fc (GHz)	5.405	Pulse repetition frequency, PRF (Hz)	1717.129
Bandwidth, δf (MHz)	56.5	Sampling rate, F_s (MHz)	64.34
Resolution	Range x Azimuth =3.5×21.6 m	Pixel spacing in slant range	Range x Azimuth =2.31×13.904 m

Three icebergs were identified and are also shown in Figure 2.1. These three icebergs are denoted by the symbols IB1, IB2 and IB3. A field program was conducted by a team at C-CORE to capture the 3D profiles of the icebergs using LiDAR and a multi-beam sonar. IB1 was profiled on 3 July 2015 and the IB2 and IB3 were profiled on 6 July 2015. A Dynascan m-250 Single Head LiDAR was used to generate point clouds for the above water part of the icebergs. A R2 Sonic 2024 Single head Multibeam Sonar beam was used to collect point clouds for the submerged portion of the icebergs. Three loops were made for a single iceberg profiling with 4 knots average speed of the survey vessel. Although the LiDAR's footprint will vary by range it has a standard resolution of 1 cm. On average, LiDAR has points density for IB1, IB2 and IB3 as 120.80, 172.05, 100.79 points/m^2 and for Sonar 23.60, 84.18, 22.1 points/m^2. The raw point clouds were then filtered to generate a clean, quantified and corrected version of the iceberg 3D profiles. These were used to generate simulated SAR images and to compare with the real SAR image.

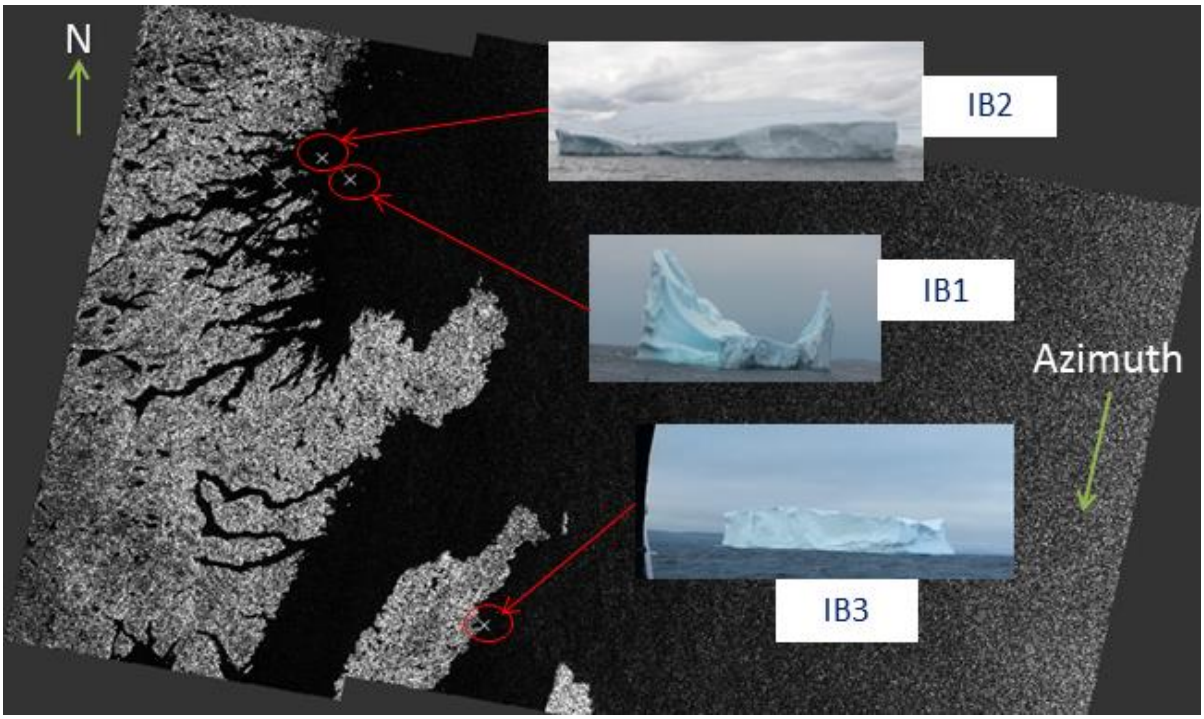

Figure 2.1 Sentinel-1 SAR image in σ_0 (m^2/m^2) showing the locations of three icebergs of interest.

2.2.1.2 Iceberg 3D Profile Orientation

Prior to simulation, it is important to know the correct orientation of the icebergs with respect to the radar look direction to get an accurate image footprint to compare with the real SAR image. Iceberg orientations in the SAR image might differ from the orientation at the time the 3D profile was captured due to significant delay between 3D profiling and SAR image acquisition time. The approximate orientations of the icebergs were obtained by overlaying the outline of icebergs (that were encoded with global positioning system (GPS) information) and the captured SAR image footprint as shown in Figure 2.2. Note that the simulated SAR image footprint is small because of the extensive simulation time required for the numerical computations by GRECOSAR. Better visualizations of the icebergs and their relative waterlines are shown in Figure 2.3.

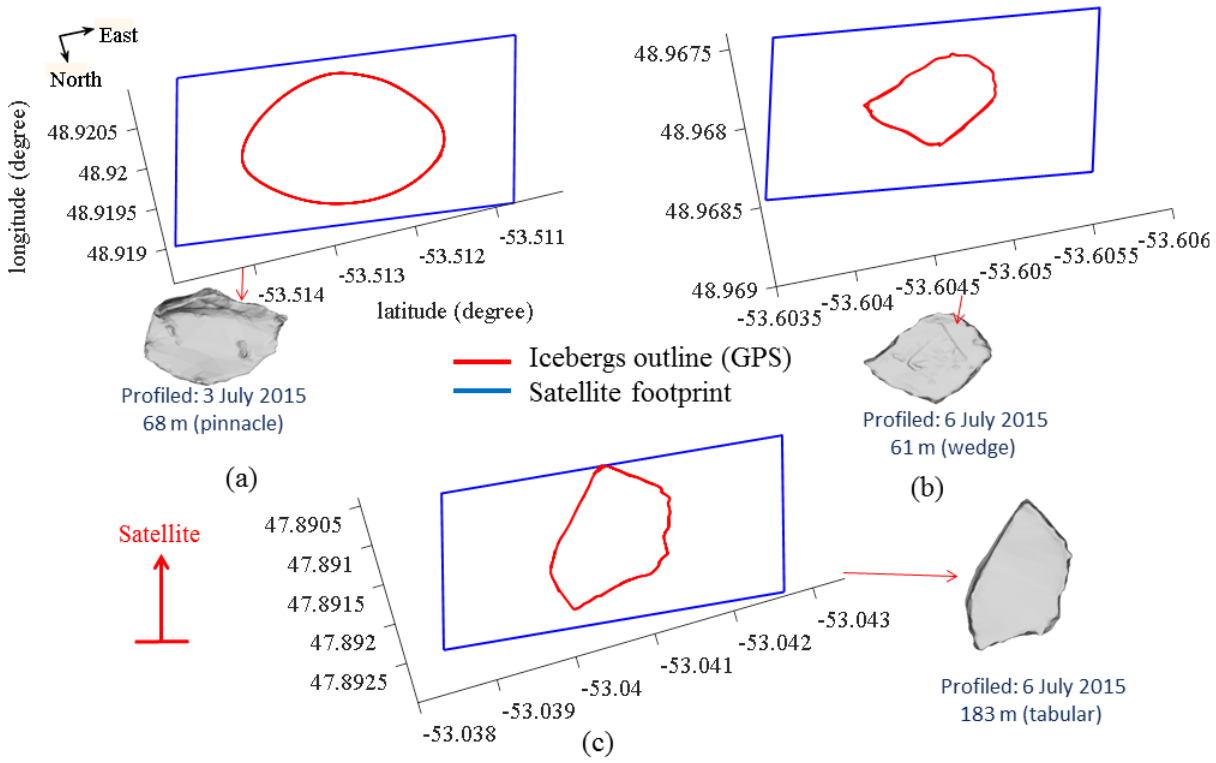

Figure 2.2 Simulated SAR image footprint (blue) and icebergs outline from GPS data (red) overlaid; icebergs (a) IB1 (b) IB2 (c) IB3.

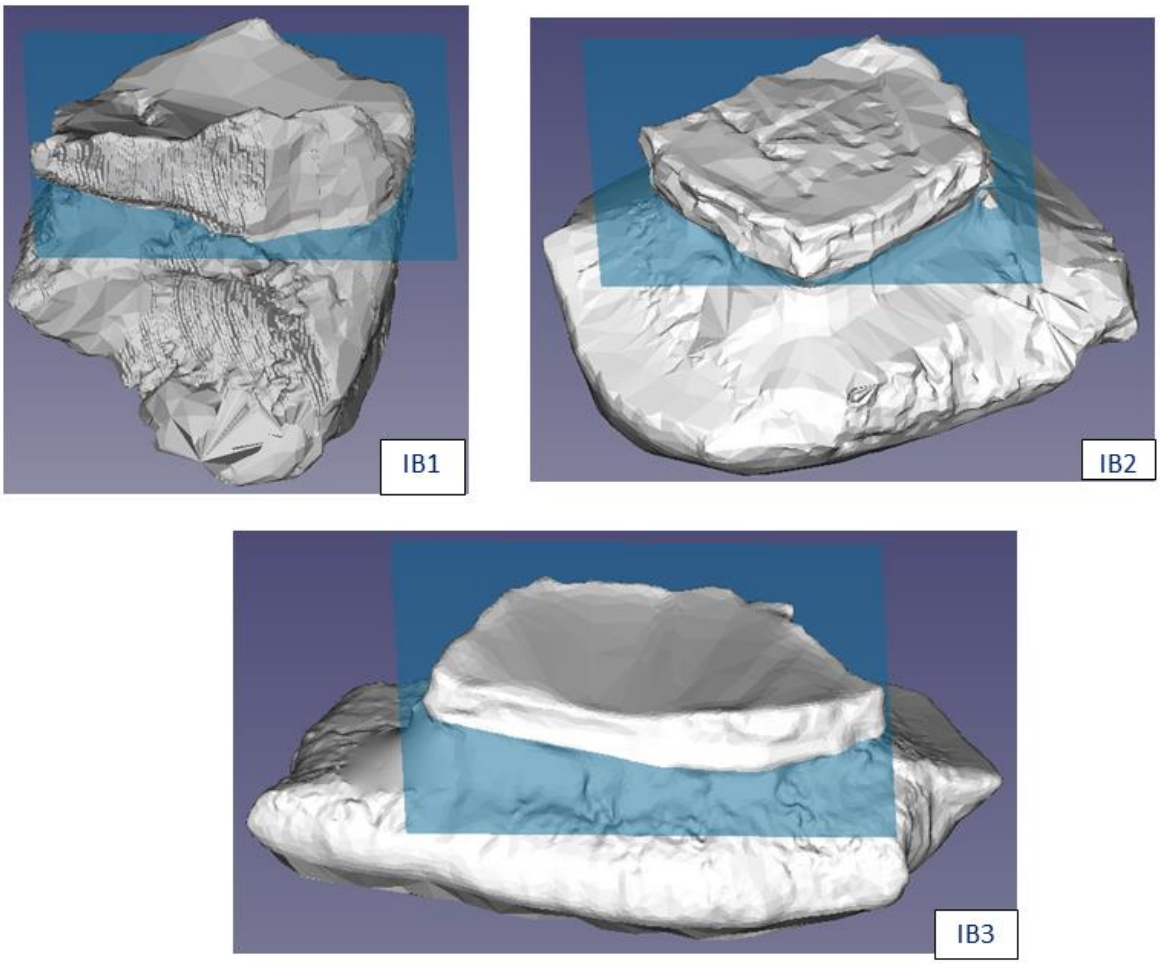

Figure 2.3 Full 3D profiles of the icebergs and relative waterlines shown by the blue surfaces.

2.2.2 EM Backscatter Simulation Parameters

2.2.2.1 Simulation Scene

The simulation scene consisted of an iceberg 3D profile surrounded by an ocean surface. GRECOSAR considers the target (iceberg) and the ocean in Figure 2.4 as a single target. It computes backscatter in every antenna position along the azimuth direction considering curvature, edges, shadows and multiple reflections. The height profile of the ocean updates as the sensor position moves along the azimuth and is defined by the Pierson-Moskowitz spectrum (described in the next section) (Pierson & Moskowitz, 1964). The geometrical parameters necessary to define the simulation scene are illustrated in Figure 2.4 and described in the following sub-sections. Looking into Figure 2.4, the SAR beam is directed in the range

direction. The berg is referenced CW with respect to the azimuth direction. The wind direction is referenced CW with resect to the range direction. The azimuth direction is along the flight direction of the satellite. The range direction is perpendicular to the right of the azimuth direction.

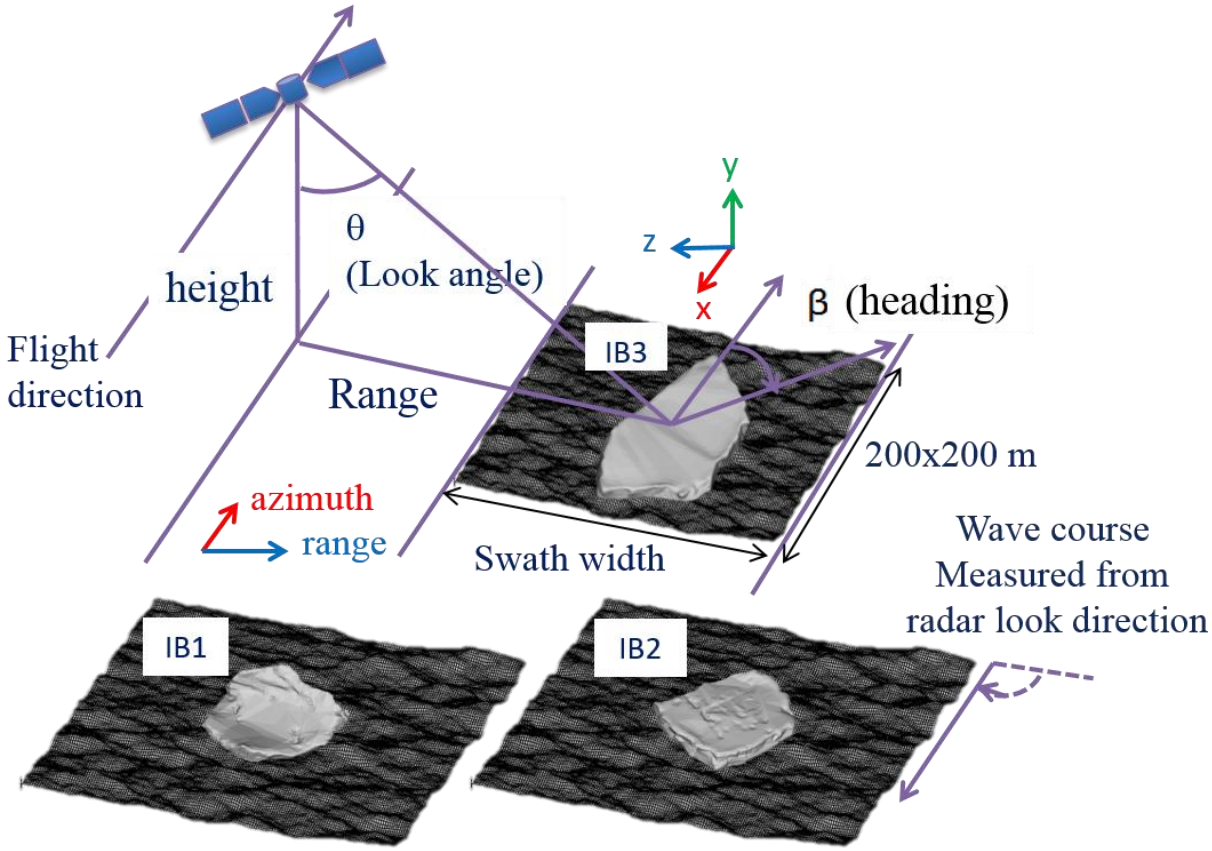

Figure 2.4 GRECOSAR simulation scene.

2.2.2.2 Ocean Surface

The surrounding ocean surface is a flat meshed surface of a CAD model as shown in Figure 2.5 (a). The surface height is modulated by an embedded MH sea model. The parameters of the MH sea model are configured by selecting pre-defined sea states in the software according to the Pierson-Moskowitz spectrum (Pierson & Moskowitz, 1964). Sea states are defined by their significant wave height h_s and average wave period T, which scales the wave spectrum's height and defines the centre frequency respectively (see Figure 2.5 (b)). GRECOSAR takes significant frequency and phase components surrounding the centre of the

Pierson-Moskowitz spectrum (Figure 2.5 (b)) and maps back to the spatial domain to modulate the height at every point in the xz plane by (2.1) and as shown in Figure 2.5 (c),

$$y(x,z,t) = \sum_{n=1}^{N}\sum_{m=1}^{M}\overline{y}_{n,m}\ \sin\{\omega t + \epsilon_{n,m} - k_n(x\cos\chi_m^* + z\sin\chi_m^*)\} \tag{2.1}$$

Where, M and N are phase and frequency components.

ω = wave components in the wave spectral density (rad/s)

k_n= wave number (rad/m)

χ_m= propagation directions in the wave spectral density (˚)

x, z and t are spatial and time coordinates (m , m, second)

$\overline{y}_{n,m}$= height of each wave component (m), defined as

$$\overline{y}_{n,m} = \sqrt{2S_z(\omega^*,\chi^*)\Delta\omega\Delta\chi} \tag{2.2}$$

Where, $\Delta\omega$ and $\Delta\chi$ are differential steps in frequency and phase axis (Fig. 2.5 (c)).

$S_z(\omega,\chi)$= wave spectral density (m^2/Hz) shown in vertical axis of Fig. 2.5 (a)

$$S_z(\omega,\chi) = \mathrm{S}(\omega)\mathrm{M}(\chi) \tag{2.3}$$

Where, $S(\omega)$ is related to significant wave height, h_s and average wave period, T by:

$$\mathrm{S}(\omega) = \frac{173h_s^2}{T^4\omega^5}\exp\{-\frac{691}{T^4\omega^4}\} \tag{2.4}$$

M(χ) is the spread function along X-axis in Fig. 2.5 (c). Parameters are described in detail in (Pierson & Moskowitz, 1964).

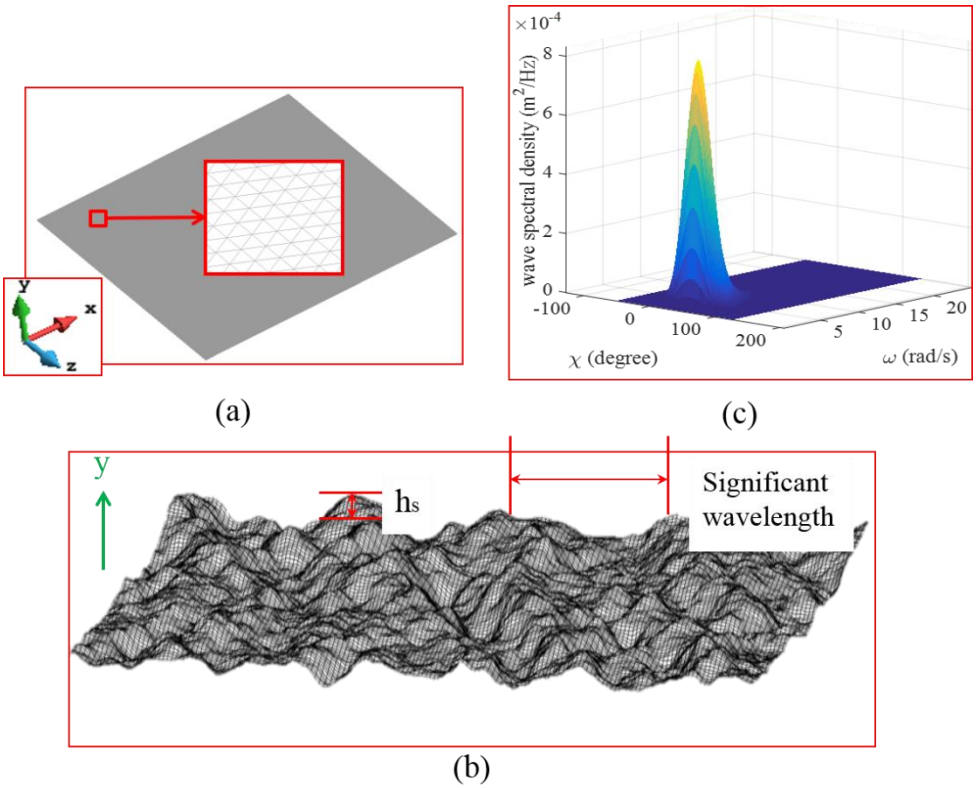

Figure 2.5 Ocean target modelling in GRECOSAR (a) 2D CAD model of a flat surface that is discretized by triangular meshes (b) the wave heights in the y direction are modulated by the frequency and direction components defined by Pierson-Moskowitz sea spectrum inside GRECOSAR (c) visualization of a Pierson-Moskowitz sea spectrum for a sea-state defined by significant wave height h_s and average wave period T. GRECOSAR takes dominant frequency and phase components centred around the peak of Pierson-Moskowitz spectrum to modulate wave heights and directions in (b). An ocean chip size of 200x200 m^2 was modelled with an iceberg model embedded at the middle of the chip.

Note that sea spray is significant along the shoreline and near the ocean/iceberg interface; this could affect ocean wave patterns. Looking from the iceberg images, the ocean looks very calm and no sea spray is visible. There are also other factors to consider, but these additional considerations are left as future work.

2.2.2.3 Meshing

The ocean waves composed of ranges of frequencies. Among them there is a certain wavelength at which EM wave from the sensor interacts strongly and reflects significant energy to the sensor. This wavelength

is called ‘creeping wavelength’ and be denoted as λ_{creep}. λ_{creep} is a function of sensor frequency and the incidence angle and related by:

$$\lambda_{creep} = \frac{\lambda_{sensor}}{2 \sin \theta} \tag{2.5}$$

The ocean model in GRECOSAR is a flat surface CAD model. To ensure that the meshed CAD surface can represent the variation of a ‘creeping wave’, the meshing size needs to be at least half of the ‘creeping wavelength’ according to the Nyquist criteria. For the case of Sentinel-1 IW3 imaging mode (43˚ incidence angle) λ_{creep} would be 4.06 cm which suggests the mesh size needs to be 2.03 cm to comply with Nyquist rate in the spatial sense. However, minimizing mesh size requires huge computational time and resources. An experiment was done to determine optimum mesh size. An ocean chip size of 100x100 m^2 was meshed by 2, 4, 5, 6 and 8 cm. Mean clutter was calculated for Sentinel-1 IW3 beam mode and relative error was calculated. To calculate error, mean clutter for a 2 cm mesh was assumed as reference. As seen in Figure 2.6, error is negligible until it starts to pick up at 6 cm and in substantial at 8 cm. Therefore, in the CAD software, the ocean chip was meshed by a 5 cm triangular mesh as a compromise between computational load and accuracy. For example, with a 5 cm mesh size and a 200x200 m^2 ocean area, the work station needed 6-7 hours to generate simulated SAR image.

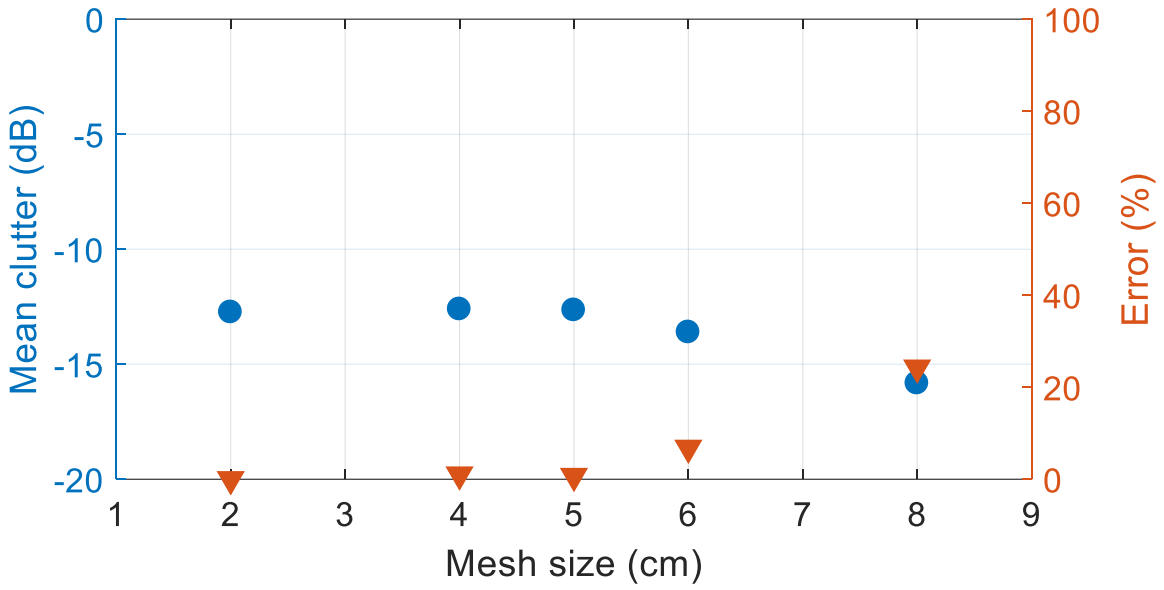

Figure 2.6 Variation of mean ocean clutter at HH channel over mesh size for Sentinel-1 IW3 mode.

2.2.2.4 Key Parameters

This sub-section will describe parameters necessary for the simulation scene to replicate a real SAR image as closely as possible. A real SAR image containing icebergs in Figure 2.1 was captured by the Sentinel-1 satellite in IW3 mode. Satellite parameters used for GRECOSAR simulation were taken from Table 2.1.

Field observation suggests the ocean was calm and the weather remained stable while the SAR image was captured. Based on this, a sea state-0 (2.57 m/s wind speed) was chosen that has significant wave height of 0.1524 m and average wave period of 1.5 second. In the simulation, to make sure the iceberg targets get equal amounts of surrounding clutter as in the real SAR image, the wave course was varied until the simulated mean backscatter equalled the real SAR image ocean clutter in HH channel. The wave course was calculated clockwise with respect to the radar look direction as shown in Figure 2.5. SAR image captured on 7 July, 2015 containing the icebergs has a mean HH channel backscatter of -24.57 dB that sets the wave course to 30˚. The role of sea state is very important in iceberg detection. With an increase in sea state, the average clutter increases, lowering the signal to clutter ratio and degrading target detection

(Vachon et al., 1997). Reduced detectability in high clutter for ship targets has been studied (Li, He, & Wang, 2009); a similar study for icebergs is intended as a future work.

Setting the right dielectric permittivity for the iceberg target is very critical for the GRECOSAR simulation. This parameter could range between from very low for cold bergs just after calving to much higher if the berg surface is under a high melting condition. GRECOSAR can only simulate surface backscatter, although it is known that for icebergs that backscatter can come from both the surface and from inside the volume (due to air bubble inclusions) and even from the bottom surface (ice to water interface at the bottom of the berg). Nonetheless, GRECOSAR provides an opportunity to determine the significance of the surface backscattering contribution at various dielectric permittivities by comparing the GRECOSAR simulations (with only surface scattering) to the real SAR images (with multiple types of scattering). Two extremes for dielectric permittivities were examined. The dielectric permittivity of a cold berg surface is well established in the literature and was extensively measured value of 3.15 with a loss factor/loss tangent of 2×10^{-3} (Haykin, Lewis, Raney, & Rossiter, 1994). To mimic the perfect melting berg condition, the permittivity of fresh water at 0° C was assumed and calculated according to (Meissner & Wentz, 2004) to be 65.8-36.4i. Modelling the iceberg surface as melt ice is expected to provide high surface backscattering that should dominate other scattering types, including the volume scattering that arises from an iceberg's multi-layer surface. This high backscatter may compensate for GRECOSAR's inherent limitation to simulate volume scattering. Nonetheless, it is recognized that an iceberg may contain localized regions of glacial ice with high and low melting surfaces and therefore the total backscatter may be a superposition of scattering from the two dielectric permittivity extremes.

In setting the permittivity of the surrounding ocean surface, a water temperature of 0° C and a salinity of 35 parts per thousand (PPT) were considered. Although the permittivity of ocean water is a function of temperature, salinity and frequency, because of its high reflectance, the relative variation should be

insignificant. The dielectric permittivity of the seawater was set to 60.8-40.6i at a frequency of 5.4 GHz and was calculated according to (Meissner & Wentz, 2004).

2.2.2.5 Target Pixels Separation from Clutter

To facilitate the analysis and quantification of the icebergs targets, the target pixels in the SAR image were separated (masked) from the surrounding ocean clutter. Ocean clutter surrounding the target pixels was isolated from the target using an intensity threshold of $m + 8\sigma$ of the ocean clutter pixels statistics for both SAR image and simulated intensity images. m is the mean and σ is the standard deviation of the ocean clutter. This simple thresholding technique is widely used and been taken from (Howell, 2008).

2.3 Results and Discussions

2.3.1 SAR Image at Varying Permittivity

Two sets of simulated SAR images were generated, one with iceberg material permittivity set to fresh cold ice and the other with actively melting surface. The simulated SAR signatures of the icebergs at these two permittivities are shown in Figure 2.7 along with real SAR signatures for comparison. All chips represent a 200x200 m^2 area and the images are for HH channel in σ_0 linear scale. Although the patterns of the high intensity regions of the image do not exactly match, the extent of the target pixels is comparable. It is very important to note that with increase in permittivity, i.e., from fresh ice to the melt condition, significant backscatter contributions come from the surface as seen in the middle and right column image clips of Figure 2.7. The high intensity region variation in the iceberg signatures might be due of the time lag between 3D profiling and SAR image capture time. The time lags between 3D profiling and SAR image capture time for IB1, IB2 and IB3 are approximately 4 days and 1 day respectively. Some environment factors e.g., high melting condition, washing and eroding of iceberg sides might have influenced the physical appearance of the icebergs.

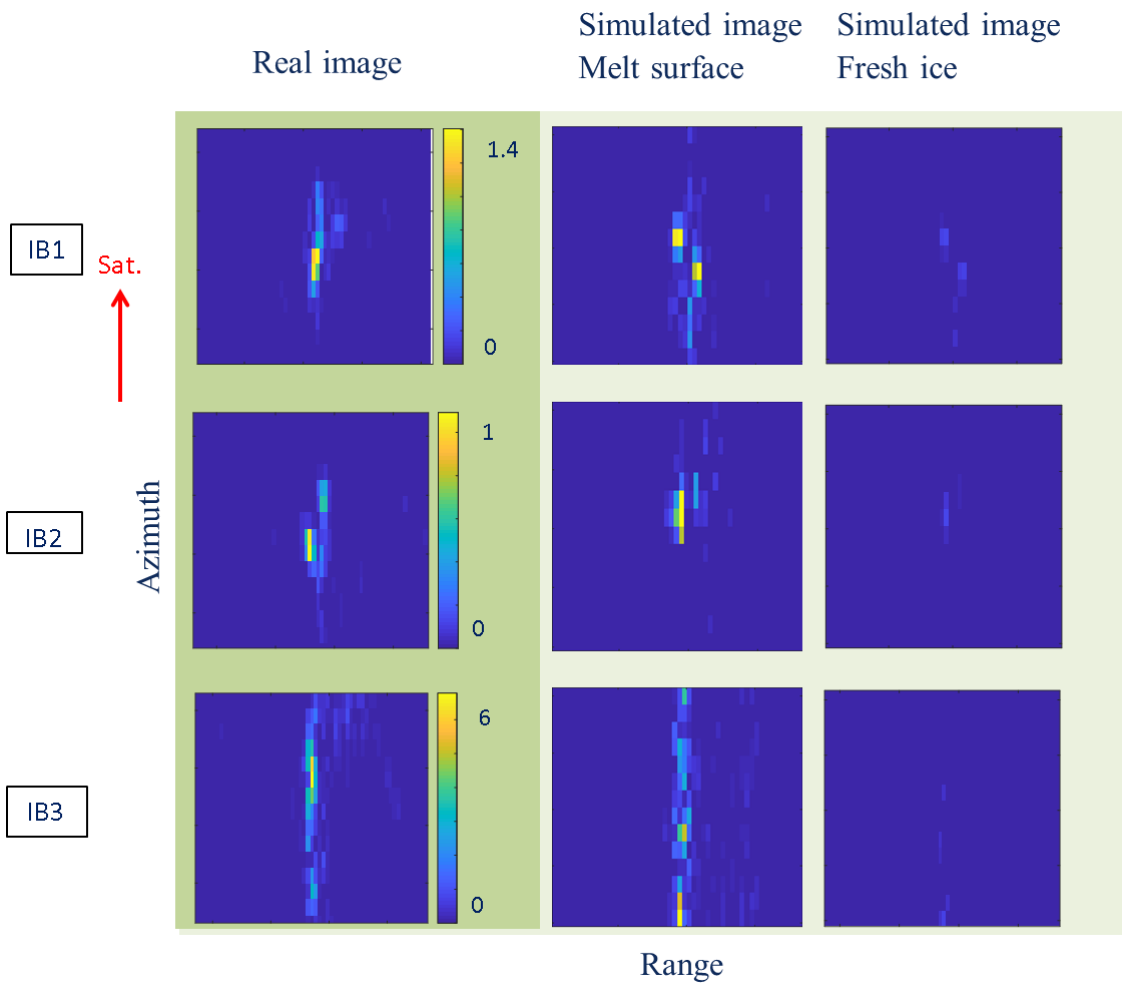

Figure 2.7 Real (left) and simulated (middle, right column) SAR images of IB1 (top row), IB2 (middle row) and IB3 (bottom row) over a 200x200 m^2 chip area. Middle column is with water permittivity at 0°, right column is with ice permittivity Images are taken in HH channel and in σ_0 (m^2/m^2) format.

It is evident from the above figure that determining iceberg permittivity is challenging and might fall at any value between fresh ice and melt water. This is a logical assumption, since a melting berg may contain both wet and dry locations, depending on the shape of the berg. As the SAR image was captured in July off the coast of Newfoundland in a summer day at around noon, it is highly probable the surface will be in a state of melt flux. The field program team also noted the actively melting iceberg surface condition. They verified this by using a paintball gun to mark the icebergs; the paintball marks were almost immediately washed out by the melting water. This is very important in simulating iceberg objects in GRECOSAR as it can only

simulate single layer contribution and the melting iceberg surface provides the dominant backscattering contribution.

2.3.2 TRCS over Orientations

The TRCS of the iceberg targets have been determined after varying the orientations of the iceberg with respect to the SAR look direction are plotted in Figure 2.8. The iceberg targets were rotated between 180˚ to 360˚ in 45˚ intervals. The TRCS of an iceberg was calculated by summing the RCS over every pixel in the target. Individual RCS of a pixel was determined by the intensity of the cell multiplied by pixel area.

$$TRCS = \Delta A \sum_{all\ pixels\ over\ the\ image\ clip} \sigma_0 \qquad (2.6)$$

The TRCS of the iceberg targets at the orientations corresponding to the real and simulated SAR image are shown in the Table 2.2. It shows the TRCS from real and simulated SAR images are in very good agreement, when considering the melt surface condition, rather than the cold fresh ice condition. Low TRCS at the fresh ice condition could also result from GRECOSAR's limitation that it only considers surface backscatter. However, it is evident that multilayer propagation in iceberg can be compensated if the surface dielectric is set for fresh water at 0˚ that represents melting water all over the surface in the iceberg target.

Table 2.2 TRCS of icebergs on real and simulated SAR images.

TRCS in dBsm	Real image	Simulated-melt surface	Simulated-fresh ice	Error (%) = |(Real-Sim. melt)/Real|x100%
IB1	27.79	28.18	17.48	1.40
IB2	26.98	26.76	16.08	0.81
IB3	37.07	36.54	21.31	1.43

Variations of the TRCS of the iceberg targets as a function of orientation (β), measured with respect to the azimuth direction CW, are shown in Figure 2.8. Of note are the maximum and minimum TRCS positions and their corresponding orientations with respect to the radar look direction. At maximum RCS positions,

the reflecting edges and the sides of the icebergs face maximum exposure to the radar look direction. The opposite happens at minimum RCS positions; in other words, the reflecting edges and the sides of the icebergs are turned away from the radar look direction.

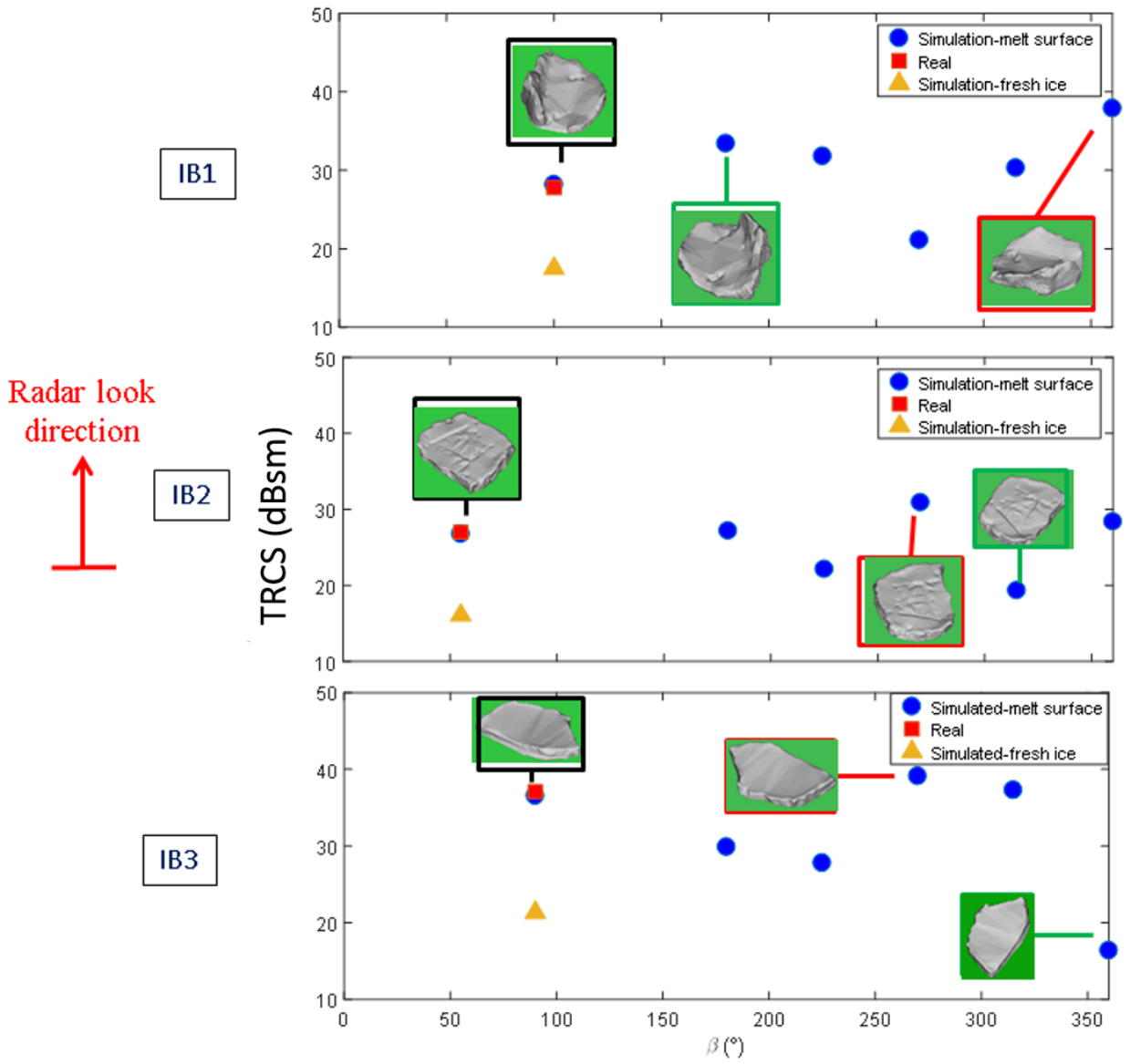

Figure 2.8 TRCS of the iceberg targets of orientations (shown in *X*-axis by *β*) between 180˚ and 360˚ with 45˚ intervals including the point where the orientation of 3D profile is like that of SAR image. Black boxes are for the SAR image orientation. Green boxes are for minimum TRCS locations and red boxes are for maximum TRCS locations.

2.4 Conclusions

An EM backscatter model of several icebergs at a satellite's higher incidence angle beam mode has been presented and compared with ground-validated DP SAR data. Measurements from SAR imagery of icebergs were captured by the Sentinel-1 satellite over Salvage, Newfoundland, Canada and then compared with simulated images generated by GRECOSAR. Simulated images were generated for low and high dielectric conditions to demonstrate seasonal surface permittivity variation of the iceberg in cold and melting conditions. The similarity of the TRCS of the simulated and SAR images and the SAR signature pattern provide a strong indication of the validity of the EM backscatter models of the icebergs. The large backscatter generated from realistic multilayer propagation in an iceberg can be compensated by a higher dielectric surface permittivity condition to emulate the backscatter generated by the single layer model in GRECOSAR. Variation of the TRCS of icebergs over orientations suggests the use of the EM backscatter model of iceberg could be very useful in designing a robust iceberg/ship classifier. Limitations of this study include the fact that GRECOSAR is only capable of single layer backscatter simulations. As shown here, this appears to be highly applicable to the mid-latitude icebergs in Newfoundland waters. It is speculated by the authors that icebergs in colder regions (e.g., Greenland) that are freshly calved or exist in sub-zero temperatures may produce a more dominant multi-layers backscatter, including both surface and volume scatter. Practically, electric permittivity is a distributed parameter across any volumetric object, whereas in GRECOSAR it is constant for an object that limits its ability more practical representation of any target. Several factors could be sources of errors in the results. Environment factors that might contribute to the difference between real and simulated SAR image results are the slow and natural drifting and rotation of the icebergs over time and melting that might smoothen the surface of the iceberg between the time of the profile acquisition and the SAR image acquisition. In GRECOSAR, the iceberg-ocean intersection representation is simplistic, whereas in the real world, this representation is more complex.

Avenues to explore in the future includes assessing the volume scattering contribution in an iceberg target by comparing GRECOSAR generated SAR images with real SAR images, taking the advantage of

GRECOSAR's inability to simulate diffuse scattering inside an iceberg's volume. This can be done, for example, by analysing polarimetric decompositions of the real and simulated iceberg backscattering. Extensive simulations will be performed to suggest optimum satellite parameters and imaging modes for iceberg and vessel discrimination and to quantify the effect of higher sea states and wind directions in iceberg detection. The results of the iceberg simulations produced in GRECOSAR are applicable for the case of icebergs in seawater of any temperature and salinity. The effect of sea-ice surrounding the iceberg can also be produced given the CAD model profile of ranges of sea-ice in hand.

2.5 References

Akbari, V., & Brekke, C. (2017). Iceberg detection in open water and sea ice using C-band radar polarimetry. Paper presented at the *Geoscience and Remote Sensing Symposium (IGARSS), 2017 IEEE International*, 2298-2301.

Akbari, V., & Brekke, C. (2018). Iceberg detection in open and ice-infested waters using C-band polarimetric synthetic aperture radar. *IEEE Transactions on Geoscience and Remote Sensing, 56*(1), 407-421.

Bentes, C., Frost, A., Velotto, D., & Tings, B. (2016). Ship-iceberg discrimination with convolutional neural networks in high resolution SAR images. Paper presented at the *EUSAR 2016: 11th European Conference on Synthetic Aperture Radar, Proceedings Of*, 1-4.

Bigg, G. R., Wadley, M. R., Stevens, D. P., & Johnson, J. A. (1997). Modelling the dynamics and thermodynamics of icebergs. *Cold Regions Science and Technology, 26*(2), 113-135.

C-CORE. (2012). *Analysis of single, dual and polarimetric synthetic aperture radar data for iceberg/ship detection and discrimination.* (No. R-08-090-673).C-CORE.

C-CORE. (2016). *DIR – ship and iceberg detection and discrimination with RCM in support of polar epsilon 2.* (No. R-15-113-1178).C-CORE.

Dierking, W., & Wesche, C. (2014). C-band radar polarimetry—useful for detection of icebergs in sea ice? *IEEE Transactions on Geoscience and Remote Sensing, 52*(1), 25-37.

Haykin, S., Lewis, E. O., Raney, R. K., & Rossiter, J. R. (1994). *Remote sensing of sea ice and icebergs* John Wiley & Sons.

Howell, C. (2008). *Iceberg and ship detection and classification in single, dual and quad polarized synthetic aperture radar* (PhD).

Howell, C., Bobby, P., Power, D., Randell, C., & Parsons, L. (2012). Detecting icebergs in sea ice using dual polarized satellite radar imagery. Paper presented at the *10th Int'L Conference and Exhibition on Performance of Ships and Structures in Ice (ICETECH),*

Howell, C., Mills, J., Power, D., Youden, J., Dodge, K., Randell, C., . . . Flett, D. (2006). A multivariate approach to iceberg and ship classification in HH/HV ASAR data. Paper presented at the *Geoscience and Remote Sensing Symposium, 2006. IGARSS 2006. IEEE International Conference On,* 3583-3586.

Howell, C., Youden, J., Lane, K., Power, D., Randell, C., & Flett, D. (2004). Iceberg and ship discrimination with ENVISAT multipolarization ASAR. Paper presented at the *Geoscience and Remote Sensing Symposium, 2004. IGARSS'04. Proceedings. 2004 IEEE International, , 1*

Kim, J., Kim, D., Kim, S., & Hwang, B. (2011). Iceberg detection using full-polarimetric RADARSAT-2 SAR data in west antarctica. Paper presented at the *Synthetic Aperture Radar (APSAR), 2011 3rd International Asia-Pacific Conference On,* 1-4.

Li, H., He, Y., & Wang, W. (2009). Improving ship detection with polarimetric SAR based on convolution between co-polarization channels. *Sensors, 9*(2), 1221-1236.

Margarit, G., & Mallorqui, J. (2008). Discretization effects in sea surface simulation applied to ship classification studies. Paper presented at the *Proc. ESA of SEASAR Workshop, , 2*

Margarit, G., Mallorqui, J., & Fabregas, X. (2007). Ship classification performance in single-pass polarimetric SAR interferometry: Evaluation of the sea interaction. Paper presented at the *Proc. ESA of POLINSAR Workshop,*

Margarit, G., Mallorqui, J., & Fabregas, X. (2006). Study of the influence of vessel motions and sea-ship interaction on classification algorithms based on single-pass polarimetric sar interferometry. Paper presented at the *Geoscience and Remote Sensing Symposium, 2006. IGARSS 2006. IEEE International Conference On*, 75-78.

Margarit, G., & Mallorqui, J. J. (2008). Assessment of polarimetric SAR interferometry for improving ship classification based on simulated data. *Sensors, 8*(12), 7715-7735.

Margarit, G., & Mallorquí, J. J. (2008). Study of sea clutter influence in ship classification algorithms based on polarimetric SAR inteferometry. Paper presented at the *Synthetic Aperture Radar (EUSAR), 2008 7th European Conference On*, 1-4.

Margarit, G., Mallorqui, J. J., & Fabregas, X. (2007). Single-pass polarimetric SAR interferometry for vessel classification. *IEEE Transactions on Geoscience and Remote Sensing, 45*(11), 3494-3502.

Margarit, G., Mallorqui, J. J., Fortuny-Guasch, J., & Lopez-Martinez, C. (2009). Exploitation of ship scattering in polarimetric SAR for an improved classification under high clutter conditions. *IEEE Transactions on Geoscience and Remote Sensing, 47*(4), 1224-1235.

Margarit, G., Mallorqui, J. J., & Lopez-Martinez, C. (2007). Grecosar, a SAR simulator for complex targets: Application to urban environments. Paper presented at the *Geoscience and Remote Sensing Symposium, 2007. IGARSS 2007. IEEE International,* 4160-4163.

Margarit, G., Mallorqui, J. J., Rius, J. M., & Sanz-Marcos, J. (2006). On the usage of GRECOSAR, an orbital polarimetric SAR simulator of complex targets, to vessel classification studies. *IEEE Transactions on Geoscience and Remote Sensing, 44*(12), 3517-3526.

Margarit, G., & Tabasco, A. (2011). Ship classification in single-pol SAR images based on fuzzy logic. *IEEE Transactions on Geoscience and Remote Sensing, 49*(8), 3129-3138.

Marino, A., & Hajnsek, I. (2012). Icebergs detection with TerraSAR-X data using a polarimetric notch filter. Paper presented at the *Geoscience and Remote Sensing Symposium (IGARSS), 2012 IEEE International,* 3273-3276.

Marino, A., & Walker, N. (2011). Ship detection with quad polarimetric TerraSAR-X data: An adaptive notch filter. Paper presented at the *Geoscience and Remote Sensing Symposium (IGARSS), 2011 IEEE International,* 245-248.

Marino, A., Walker, N., & Woodhouse, I. (2010). Ship detection with RADARSAT-2 quad-pol SAR data using a notch filter based on perturbation analysis. Paper presented at the *Geoscience and Remote Sensing Symposium (IGARSS), 2010 IEEE International,* 3704-3707.

Meissner, T., & Wentz, F. J. (2004). The complex dielectric constant of pure and sea water from microwave satellite observations. *IEEE Transactions on Geoscience and Remote Sensing, 42*(9), 1836-1849.

Meyer, F., & Hinz, S. (2009). Automatic ship detection in space-borne SAR imagery. *Int.Arch.Photogram.Remote Sens.Spatial Inform.Sci, 38*(1), 1682-1750.

Pastina, D., Fico, F., & Lombardo, P. (2011). Detection of ship targets in COSMO-SkyMed SAR images. Paper presented at the *Radar Conference (RADAR), 2011 IEEE,* 928-933.

Pierson, W. J., & Moskowitz, L. (1964). A proposed spectral form for fully developed wind seas based on the similarity theory of SA kitaigorodskii. *Journal of Geophysical Research, 69*(24), 5181-5190.

Power, D., Youden, J., Lane, K., Randell, C., & Flett, D. (2001). Iceberg detection capabilities of RADARSAT synthetic aperture radar. *Canadian Journal of Remote Sensing, 27*(5), 476-486.

Randell, C., Freeman, R., Power, D., & Stuckey, P. (2009). SS: Canadian: Atlantic development; technological advances to assess, manage and reduce ice risk in northern developments. Paper presented at the *Offshore Technology Conference,*

Tello, M., López-Martínez, C., Mallorquí, J. J., & Greidanus, H. (2005). A novel algorithm for ship detection in envisat SAR imagery based on the wavelet transform. Paper presented at the *Envisat & ERS Symposium, , 572*

Touzi, R., Charbonneau, F., Hawkins, R., & Vachon, P. (2004). Ship detection and characterization using polarimetric SAR. *Canadian Journal of Remote Sensing, 30*(3), 552-559.

Vachon, P. W., & Wolfe, J. (2011). C-band cross-polarization wind speed retrieval. *IEEE Geoscience and Remote Sensing Letters, 8*(3), 456-459.

Vachon, P., Campbell, J., Bjerkelund, C., Dobson, F., & Rey, M. (1997). Ship detection by the RADARSAT SAR: Validation of detection model predictions. *Canadian Journal of Remote Sensing, 23*(1), 48-59.

Wesche, C., & Dierking, W. (2012). Iceberg signatures and detection in SAR images in two test regions of the weddell sea, antarctica. *Journal of Glaciology, 58*(208), 325-339.

Yam, L. E., Mallorqui, J. J., & Rius, J. M. (2012). Validation of a sea surface model for simulations of dynamic maritime SAR images. Paper presented at the *Geoscience and Remote Sensing Symposium (IGARSS), 2012 IEEE International*, 2813-2816.

Chapter 3 EM Backscatter Modelling of Iceberg at Small Incidence Angles using Quad Polarization Radar Modes

3.1 Introduction

The good agreement seen in the previous chapter between the simulated and real SAR data provides a strong basis to complement and extend the EM work into further combinations of sensor and environmental parameters. The EM interaction at the iceberg and ocean is a complex phenomenon and varies as the incidence angle and sea state changes. In this chapter, EM backscatter modelling will be done at satellite's lower incidence angle beam mode and compared with QP RADARSAT-2 data in terms of radiometric properties. Surrounding ocean states driven by varying wind speed and direction will be explored to determine if the modelling work produces trends observed in real life. The availability of QP RADARSAT-2 data provided an opportunity to check on the integrity of polarimetric properties in the iceberg EM backscatter model that was completed in this chapter. Similar to previous chapter, another field program was operational off the coast of Bonavista, Newfoundland and Labrador to collect 3D profiles of the icebergs to use within the simulation. The field program was conducted in June when the weather was relatively warm (between 10° and 20° Celsius) and the team observed active melting of the bergs. This was confirmed by firing paint-balls at the icebergs and observing that the paint quickly washed away from the bergs in seconds. In the previous chapter, then a melt water dielectric was used in the model to simulate the melting berg conditions showed promising results in that iceberg brightness compared favourable to real SAR data. A mathematical backscatter model for icebergs would be an important tool to predict to what extent a melting layer would contribute to backscatter. Modelling work exists for sea-ice (Partington & Hanna, 1994), snow covered sea-ice (Komarov, Isleifson, Barber, & Shafai, 2015; Komarov, Landy, Komarov, & Barber, 2017) and snowpack layer (Longepe, Allain, Ferro-Famil, Pottier, & Durand, 2009; Matzler, Aebischer, & Schanda, 1984; Phan et al., 2012), however no such model exists for icebergs. A mathematical backscatter model of the iceberg, including of a melt-water layer, is presented below that assesses the influence of melt layer thickness on the overall backscatter return from the target.

This chapter includes the following sections: “Field Data and 3D Profile Acquisition,” “GRECOSAR Simulation Parameters,” “GRECOSAR Simulations,” “Polarimetric Decomposition Comparison,” “2D Iceberg Backscatter Model,” and finally “Discussion.” “Field Program and 3D Profile Acquisition” describes the real SAR images that were captured during the field program off the coast of Bonavista, NL. The “GRECOSAR Simulation Parameters” section describes wide ranges of simulation parameters required for a confident simulation in GRECOSAR. The “GRECOSAR Simulations” section presents all the SAR simulations based on the parameters. The “Polarimetric Decomposition Comparison” section compares Pauli decompositions of the SAR images with the actual SAR acquisitions of the same icebergs. The “2D Iceberg Backscatter Model” section contains a simple mathematical model of an iceberg for analysis of the iceberg melting effect. The “Discussion” section sums up the article and its findings and as well provides future directions of this work.

3.2 Field Data and 3D Profile Acquisition

3.2.1 SAR Image Acquisition

Two RADARSAT-2 images were captured containing icebergs off the coast of Bonavista, NL, Canada on 13 June and 16 June 2017 respectively (Figure 3.1 the SAR images were in FQ1W and FQ2W mode and in SLC format). The image was radiometrically scaled with PCI Geomatica software to ground range intensity (σ_0) format to match the GRECOSAR generated SAR image format. Quick looks of the two SAR images and their imaging geometry are shown in Figure 3.2 and Figure 3.3. More detail on the RADARSAT-2 imaging mode is shown in Table 3.1.

The local incidence angles for icebergs termed as IB4, IB5 have been calculated to be 18.76˚ and 18.55˚ respectively. The third iceberg, IB6 has incidence angle of 21.85˚. Incidence angles of FQ1W and FQ2W mode have been used in this modelling to adhere to the standard incidence angles of the RADARSAT-2 Fine Quad (FQ) beam mode.

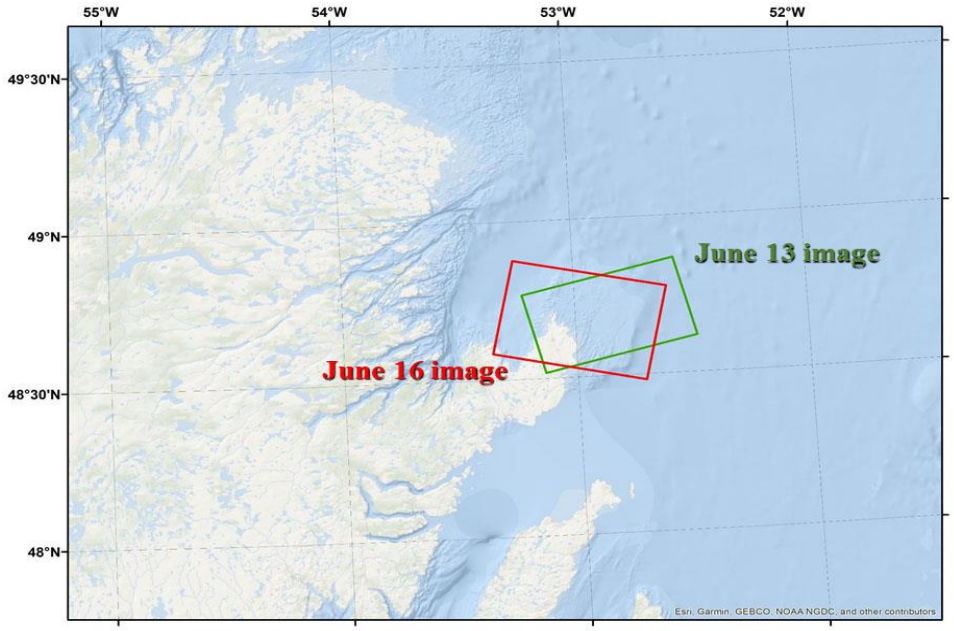

Figure 3.1 Field study location and RADARSAT-2 SAR image footprints.

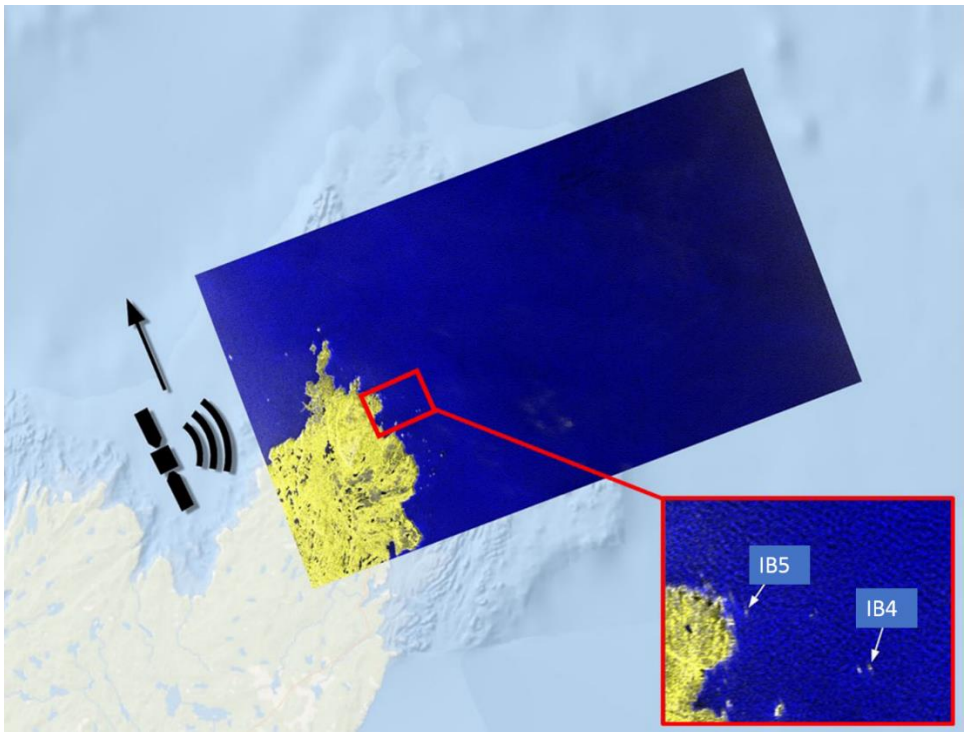

Figure 3.2 RADARSAT-2 SAR image from June 13 (false coloured with RGB = HV, HH, HH channels) showing the locations of two icebergs of interest. The satellite icon indicates the azimuth and range look directions. RADARSAT-2 data and data products © 2017 MDA Geospatial Services, all rights reserved. RADARSAT is an official mark of the Canadian Space Agency.

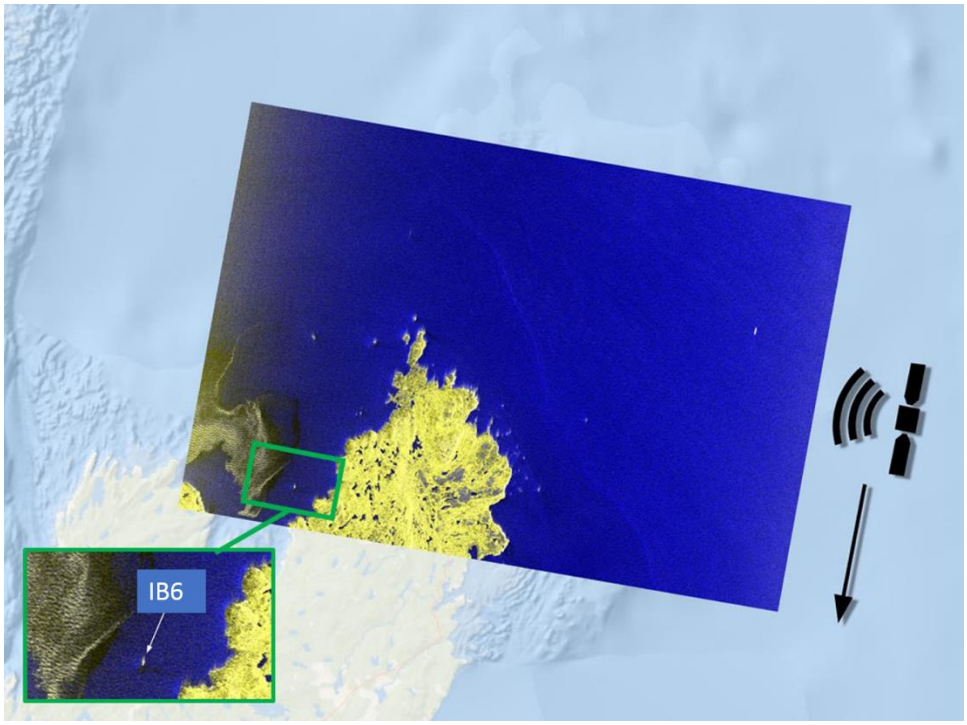

Figure 3.3 RADARSAT-2 SAR image from June 16 (false coloured with RGB = HV, HH, HH channels) showing the locations of one iceberg of interest. RADARSAT-2 data and data products © 2017 MDA Geospatial Services, all rights reserved. RADARSAT is an official mark of the Canadian Space Agency.

Table 3.1 RADARSAT-2 satellite parameters.

Beam mode / Parameters	FQ1W	FQ2W
Acquisition Date	June 13, 2017	June 16, 2017
Acquisition Time	2106 hrs UTC	0954 hrs UTC
Incidence angle, φ (˚)	19.35	20.85
Orbit inclination, (˚)	98.6	
Pass direction	Ascending	Descending
Antenna pointing	Right	Right
Resolution, Range × Azimuth (m)	4.52 x 4.83	4.733 x 5.28
Pixel spacing in ground range, Range × Azimuth (m)	14.6 x 4.83	13.22 x 5.3
Centre frequency, Fc (GHz)	5.405	
Pulse repetition frequency (Hz)	1389	
Bandwidth, δf (MHz)	31.02	
Sampling rate, F_s (MHz)	31.9	
Pulse width, τ (μs)	21	

3.2.2 3D Profiling of Icebergs

A field program was conducted by a team of C-CORE to capture these 3D profiles of the icebergs using LiDAR and a multi-beam sonar. IB4, IB5 were profiled on 13 June 2017, respectively 1 hour 35 minutes and 3 hours 15 minutes, respectively, later than the SAR image capture. IB6 was profiled on 16 June 2017, 4 hours 38 minutes after the SAR image was taken. A Dynascan m-250 Single Head LiDAR was used to generate point clouds for the above water part of the icebergs. A R2 Sonic 2024 Single head multibeam sonar was used to collect point clouds for the submerged portion of the icebergs. A single iceberg profiling required three loops to encircle the bergs to allow the removal of iceberg drift from the profile measurement. The average speed of the survey vessel during data acquisition was 4 knots. Although the LiDAR's footprint will vary by range it has a standard resolution of 1 cm. The raw point clouds were filtered to generate clean, quantified and corrected versions of the iceberg 3D profiles. The final version of the 3D profiles is shown in Figure 3.4.

The physical properties and conditions of the icebergs, also noted during the field program, are summarized in Table 3.2.

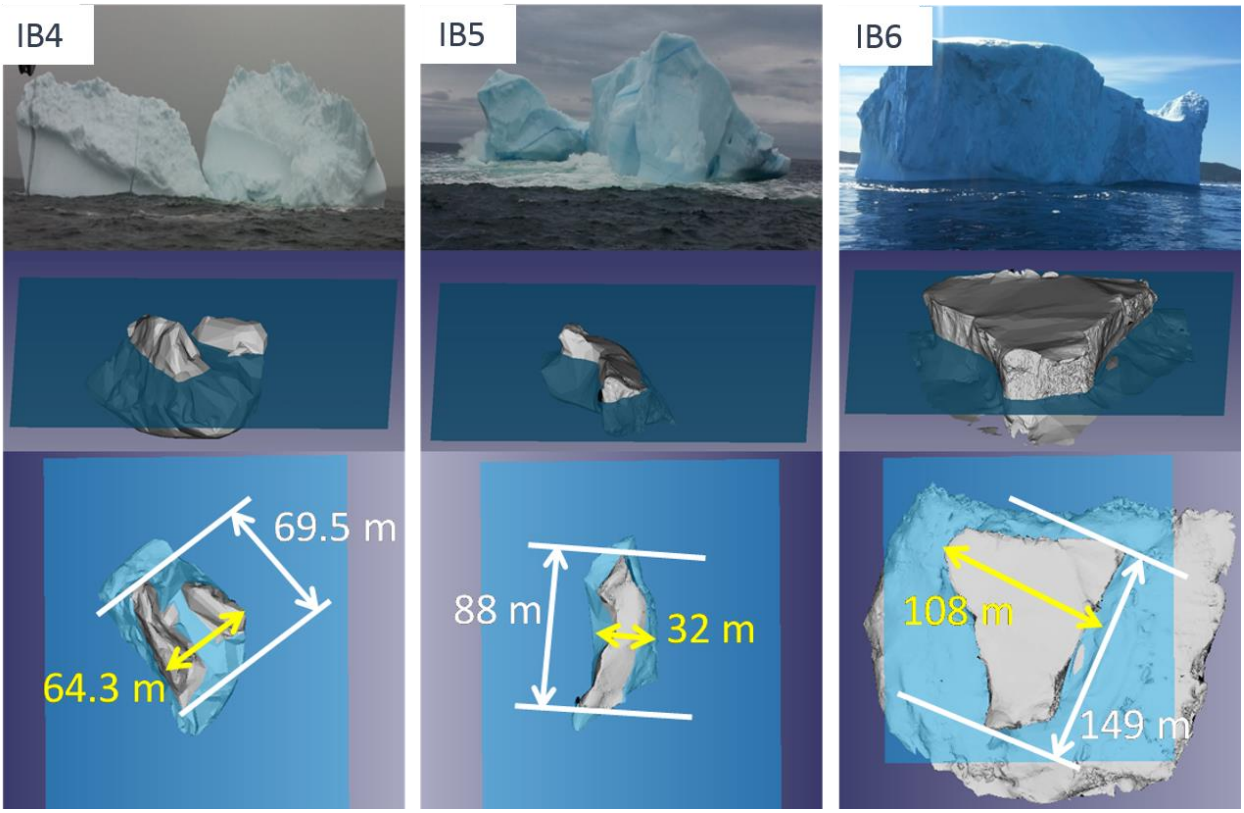

Figure 3.4 Real icebergs photos (top row) and full 3D profiles of the icebergs and relative waterline (WL) shown by the blue surfaces (middle row: perspective view and down row: top view).

Table 3.2 Iceberg physical parameters.

Parameter	Iceberg		
	IB4	IB5	IB6
Maximum WL length (m)	69.5	88	149
Transverse WL length (m)	64.3	32	108
Keel depth (m)	45	32	75
Sail height (m)	21	12	27
Water Depth	45	32	75
Shape	pinnacle	wedge	tabular
Status	grounded	grounded	grounded

3.2.3 Iceberg 3D Profile Orientation

Prior to simulation, it is important that the orientation of the icebergs with respect to the radar look direction remains the same as in the real SAR image. This was ensured by encoding every point cloud in the 3D profile with the measured GPS positions of the vessel. As suggested above, there was a time delay between

the 3D profiling and SAR image acquisition. Some of the icebergs were grounded and they are expected to move very little in the time gap.

3.3 GRECOSAR Simulation Parameters

3.3.1 Simulation Scene

The simulation scene consisted of a 3D profile containing an iceberg surrounded by an ocean surface. The geometrical parameters necessary to define the simulation scene are illustrated in Figure 3.5 and described in the following sub-sections.

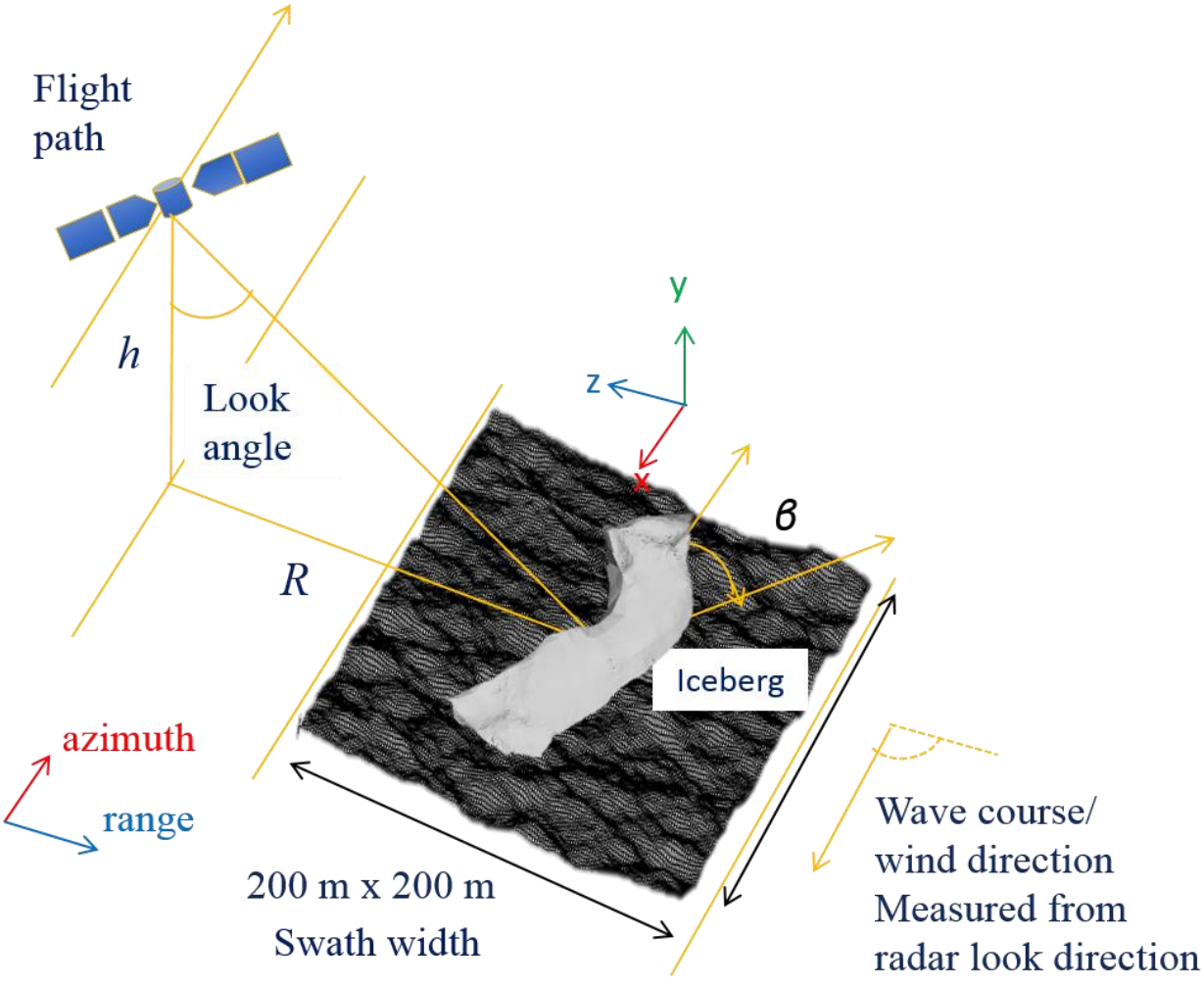

Figure 3.5 Simulation scene and parameters in GRECOSAR.

3.3.1.1 Ocean Surface

The surrounding ocean is a CAD model of a square-shaped flat meshed surface. The surface height is modulated by an embedded MH sea model. The harmonic components and directional information of the MH sea model comes from the Pierson-Moskowitz spectrum (Pierson & Moskowitz, 1964), which is defined by significant wave height h_s and average wave period T. GRECOSAR translates this information to spatial height variation as shown in Figure 3.5. Details of the procedure can be found in Chapter 2 (Ferdous et al., 2018). Validation of sea surface model in GRECOSAR has been published in (Yam, Mallorqui, & Rius, 2012). An ocean chip size of 200x200 m^2 was used to simulate IB4, IB5 and 250x250 m^2 was used for IB6. Note that the Pierson-Moskowitz spectrum assumes a deep-water condition (depth>=$\lambda_w/2$), where λ_w is the largest ocean wavelength. In our examples, the shallowest water depth is 32 m (for IB5), and this satisfies the deep-water criteria for the wind speeds and sea states being considered here.

3.3.1.2 Meshing of the Ocean Surface

Similar experiment has been done to determine the optimum mesh size as in chapter 2. For the case of RADARSAT-2 FQ1W imaging mode (19˚ incidence angle) λ_{creep} would be 8.31 cm which suggests the mesh size needs to be 4.15 cm to comply with the Nyquist rate. An ocean chip size of 100x100 m^2 was meshed by 2, 4, 5, 6 and 8 cm. Mean clutter was calculated for the RADATSAT-2 FQ1W beam mode and the relative error was calculated. To calculate error, mean clutter for the 2 cm mesh was assumed as a reference. As seen in Figure 3.6 the error is negligible for all cases. A 4 cm triangular mesh size seemed a reasonable choice to be consistent with previous workflow and again a compromise between computational load and accuracy.

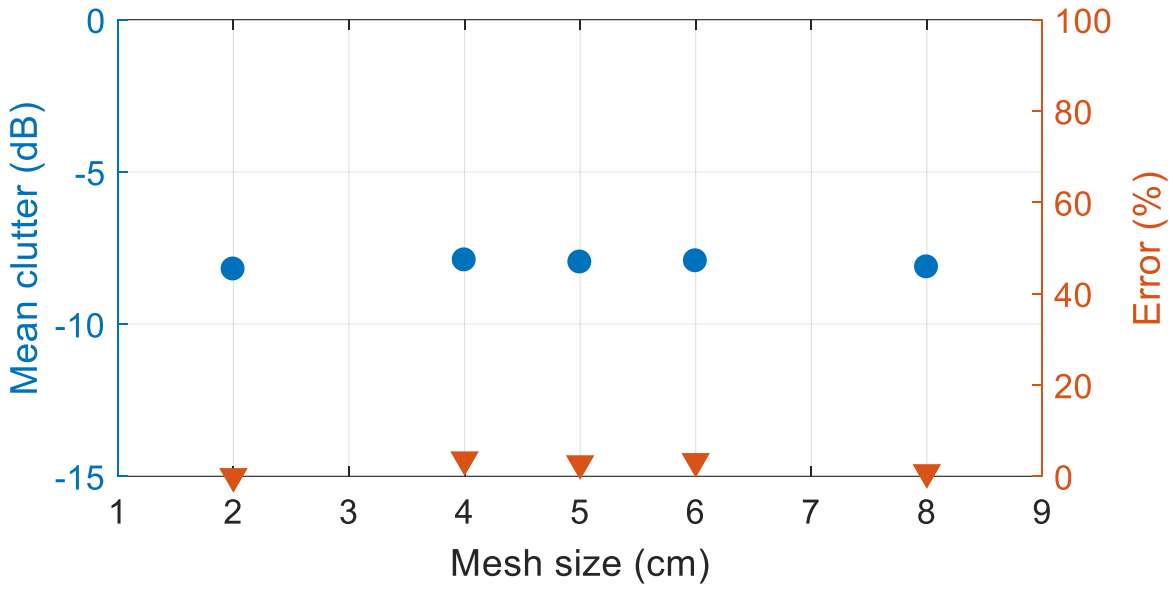

Figure 3.6 Variation of mean ocean clutter at HH channel over mesh size for RADARSAT-2 FQ1W mode.

3.3.2 Wind Speed and Direction

As noted earlier, the role of sea state is very important in iceberg detection. With an increase in sea state, the average clutter increases, lowering the signal to clutter ratio and degrading target detection (Vachon, PW, Campbell, Bjerkelund, Dobson, & Rey, 1997). Reduced detectability in high clutter for ship targets has been seen in (Li, He, & Wang, 2009).

Wind speed and direction drive ocean roughness and determine the amount of ocean clutter seen in a SAR image. CMOD4 (Vachon, Paris W. & Wolfe, 2011) is a geophysical model that can retrieve wind speed from full polarimetric RADARSAT-2 image data and predict clutter variation over wind directions. Stoffelen et al. in (1997) reported error margin of 0.5 m/s of the CMOD4 model. Retrieved wind speed by CMOD4 for image-1 is 7.2 m/s and for image-2 is 7.17 m/s. The variation of ocean clutter over wind direction for image-1 and -2 has been shown as blue and red lines in Figure 3.7. In order for the simulated ocean clutter to be a close representative of the real clutter behavior in image-1 and -2, parameters of the MH sea model have been adjusted to h_s=0.04 m, T=0.155 sec. This produces ocean clutter variation that is

a good match with the image-1 and -2 scene (green line in Figure 3.7). This combination is used to generate simulated ocean clutter at 7.2 m/s. Part of this chapter will investigate the influence of wind speed on iceberg targets.

Wind direction for the image-1 and -2 scenes was measured from the local weather station data in reasonable proximity to the SAR image capture time. The closest weather station was Bonavista, NL. Predicted wind direction for image-1 is 78˚ CW from the radar look direction at 2100 hrs UTC, which is 6 minutes before the SAR image capture. For image-2, it is 352˚ CW from the radar look direction at 1000 hrs UTC which is 6 minutes after the SAR image capture.

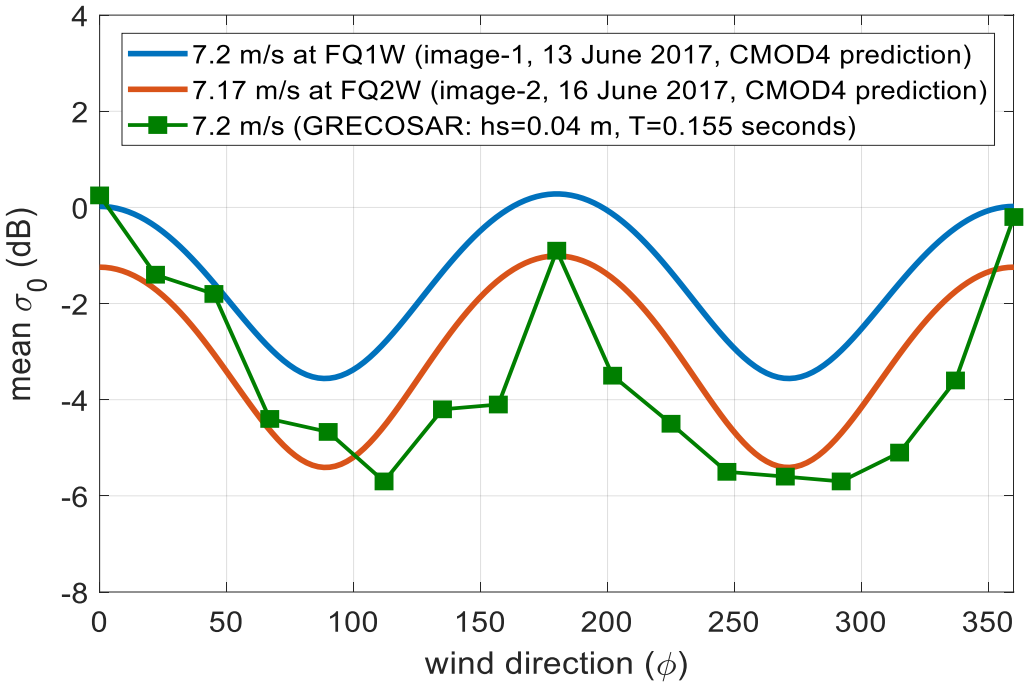

Figure 3.7 Ocean backscatter variation over wind direction in VV channel.

3.3.3 Dielectric Permittivity

Setting the correct dielectric permittivity for the iceberg target is very critical for the GRECOSAR simulation. This parameter could range between from very low for cold bergs just after calving and could be much higher if the berg surface is under a high melting condition. GRECOSAR can only simulate surface

backscatter, although it is known that for icebergs that backscatter can come from both the surface and from inside the volume (due to air bubble inclusions) and even from the bottom surface (ice to water interface at the bottom of the berg). Nonetheless, GRECOSAR provides an opportunity to determine the significance of the surface backscattering contribution at various dielectric permittivities by comparing the GRECOSAR simulations (with only surface scattering) to the real SAR images (potentially with multiple types of scattering). Two extreme dielectric permittivities were examined. The dielectric permittivity of a cold berg surface is well established in the literature and was set to 3.15 with a loss factor of 2×10^{-3} (Haykin et al., 1994). To mimic the perfect melting berg condition, the permittivity of fresh water at 0° C was assumed and calculated according to (Meissner & Wentz, 2004) to be 65.8-36.4i. Modelling the iceberg surface as melt ice is expected to provide high surface backscattering that should dominate other scattering types, including the volume scattering that arises from an iceberg's multi-layer surface. This high backscatter may compensate for GRECOSAR's inherent limitation to simulate volume scattering. Nonetheless, it is recognized that an iceberg may contain localized regions of glacial ice with high and low melting surfaces and therefore the total backscatter may be a superposition of scattering from the two dielectric permittivity extremes.

In setting the permittivity of the surrounding ocean surface, a water temperature of 0° C and a salinity of 35 PPT or, equivalently, practical salinity unit (PSU) were considered. Although the permittivity of ocean water is a function of temperature, salinity and frequency, because of its high reflectance, the relative variation should be insignificant. The dielectric permittivity of the seawater was set to 60.8-40.6i at a frequency of 5.4 GHz and was calculated according to (Meissner & Wentz, 2004).

3.4 GRECOSAR Simulations

Ranges of simulations were produced, based on the parameters mentioned in the previous section. These simulations are described below. Note that the SAR simulation parameters have been taken from Table 3.1.

3.4.1 Varying Wind Directions

Simulated SAR images were generated for the 0-90˚ wind direction range for all three icebergs and compared with the real SAR images. Comparisons are made in terms of SAR signature, TRCS and polarimetric decomposition.

3.4.1.1 Simulated SAR Signature

For the simulations, QP SAR images were generated for all four channels (HH, HV, VH, VV). The images are displayed in ground range intensity format (σ_0). The HV channel has been chosen for display, thanks to its higher signal to clutter ratio for low incidence angle compared with the two co-pol channels (Touzi, Charbonneau, Hawkins, & Vachon, 2004). Target pixels were separated and segmented from clutter pixels by a threshold of $m + 8\sigma$, where, m is the mean and σ is the standard deviation of the ocean clutter. This mask has been applied to the rest of the four channels to extract target pixel components in HH, VH and VV channels.

Figure 3.8 shows a comparison of SAR signatures for IB4 for various wind directions. For each of the images in this figure, the Y-axis is the azimuth (along orbit) direction of the satellite and the X-axis is the range (transverse to orbit) direction. The measured wind direction at the time of IB4 SAR image capture was 78˚. We can see that the simulated SAR image of IB4 at 78˚ qualitatively matches closely with the real SAR image. It is noteworthy that there is significant variation of the SAR signature with wind direction. Specifically, the pattern of the high intensity pixels change, but to a lesser extent than the lower intensity pixels in the vicinity of the primary backscatter. This is because change in wind direction is expected to modify the interaction of the backscatter near the iceberg-ocean interface.

Figure 3.9 shows a comparison of SAR signatures for IB5 using the same axes conventions as Figure 3.8. The measured wind direction at the time of IB5 SAR image capture was 78˚. It may be observed that the simulated SAR image of IB5 at 22˚ is a better qualitative match to the actual SAR image than the 78˚

simulation. Similar to IB4, low intensity pixels surrounding the IB5 are seen to be re-oriented as the wind direction changes.

Figure 3.10 Shows a comparison of SAR signatures for IB6. We can see that real SAR signature at 352˚ looks most similar to the simulated SAR signatures of 337˚ and 360˚. Similar to IB4 and IB5, the low intensity pixels surrounding IB6 are seen to be re-oriented as the wind direction changes.

All three icebergs were grounded at the time of profiling and image acquisition. A slight rotational movement may have taken place before the image acquisition, but this would not be expected to drastically alter the results.

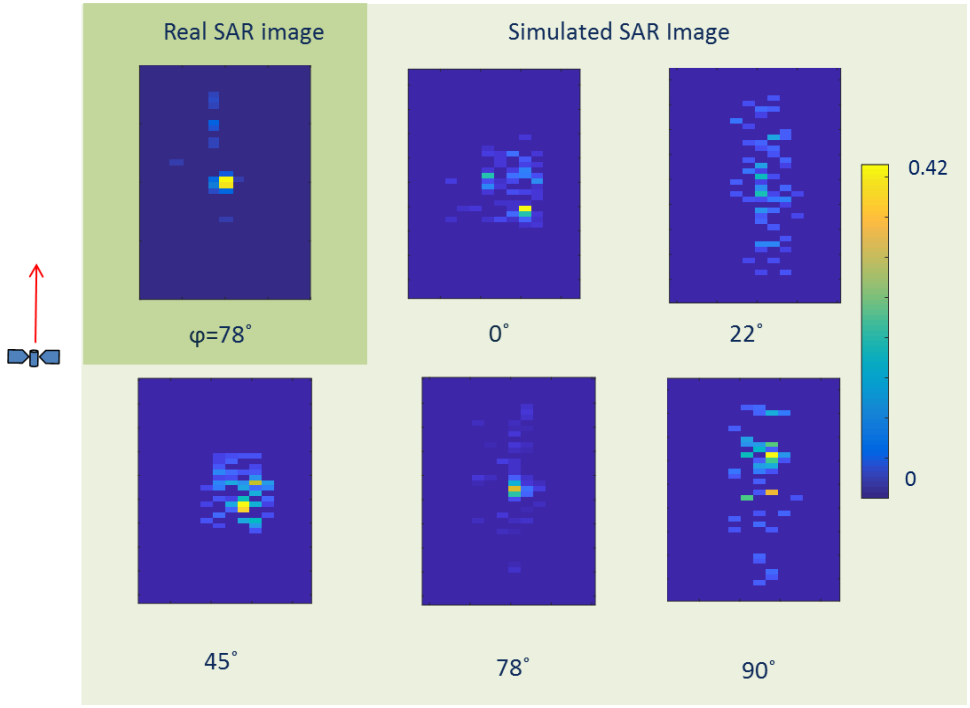

Figure 3.8 Real and simulated SAR signatures of IB4 in HV channel and in σ_0 (m^2/m^2) format.

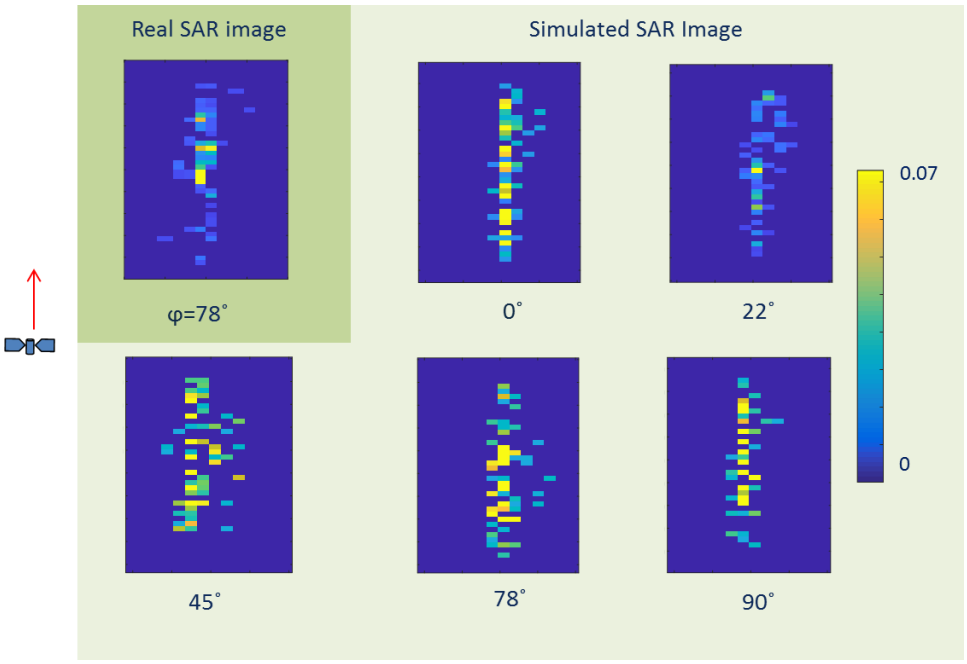

Figure 3.9 Real and simulated SAR signatures of IB5 in HV channel and in σ_0 (m^2/m^2) format.

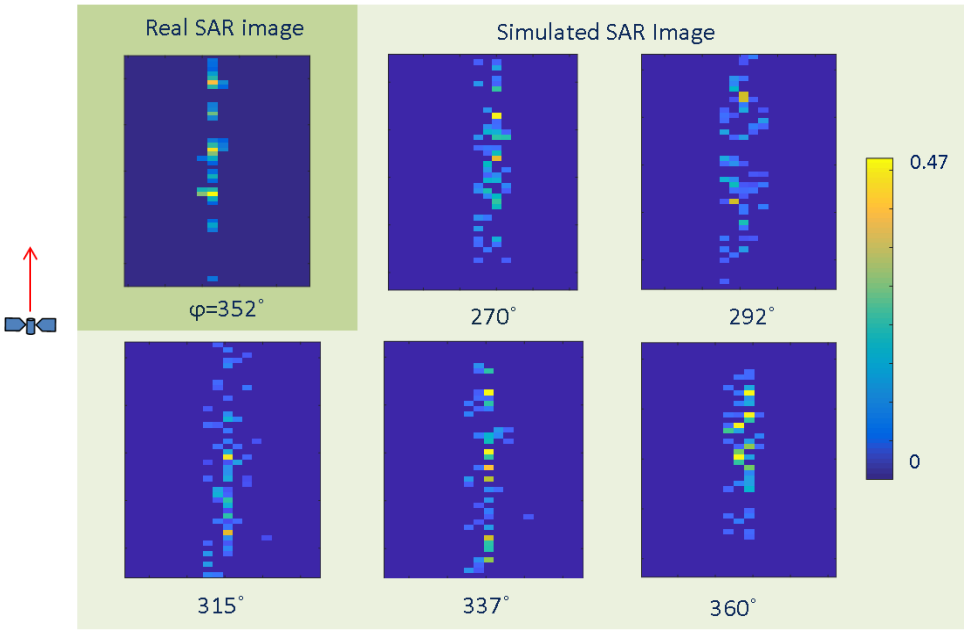

Figure 3.10 Real and simulated SAR signatures of IB6 in HV channel and in σ_0 (m^2/m^2) format.

3.4.1.2 Image Similarity Quantification

The similarity between the real and simulated SAR signatures have been measured by the structural similarity index measure (SSIM) described in (Wang, Bovik, Sheikh, & Simoncelli, 2004). The MATLAB function named 'ssim' has been used to determine SSIM index in (%). The real SAR image was set as a reference for the measurements. Figure 3.11 summarizes the results for the three icebergs. SSIM index has been found maximum for IB4 at 22˚ (86.5%) and IB5 at 78˚ (94%), whereas for IB6 maximum SSIM index (75.1%) has been found at 337˚.

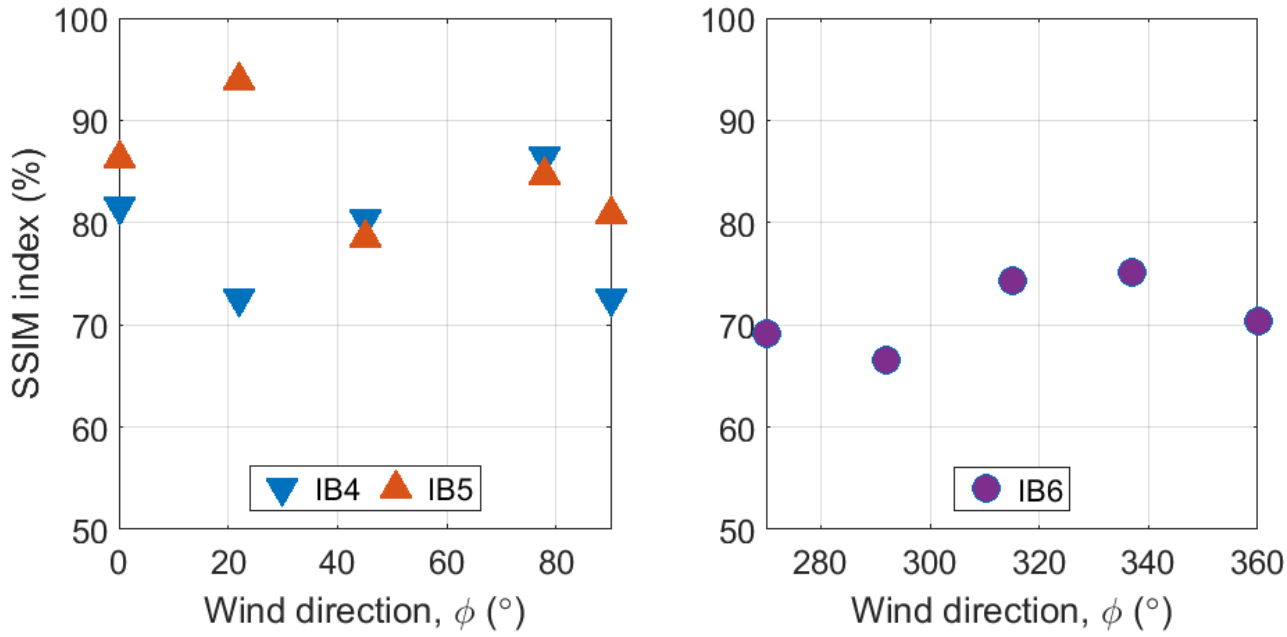

Figure 3.11 Image similarity of IB4, IB5 and IB6 over wind direction.

3.4.1.3 TRCS

The TRCS of a target is a strong measure that the target has been detected by the SAR sensor. Targets of higher RCS are obviously easier to detect, given the larger contrast between the target pixels and the background clutter. In this case, the TRCS was calculated by summing the RCS over every pixel in the segmented target. The individual RCS of a pixel was determined by the intensity of the cell multiplied by pixel area.

Figure 3.12 shows TRCS of IB4 versus wind direction, based on the simulated SAR images. The TRCS calculated from real SAR image is very close to the simulation at 78˚, which is the measured wind direction at the time of SAR image acquisition. The maximum SSIM was also found at this wind direction (Figure 3.11). This RCS plot shows how the wind direction can influence the TRCS; in the case of IB4, it is in the range of 21-26 dBsm.

Figure 3.13 shows TRCS of IB5 versus wind direction based on the simulated SAR images. TRCS calculated from real SAR image is very close to the simulation at 22˚, whereas the measured wind direction at the time of the real SAR image was 78˚. This is consistent with Figure 3.9 and maximum SSIM seen in Figure 3.11. whereby, the SAR backscatter pattern most closely resembled the simulation at 22˚. The simulated RCS of IB5 varies in the range of 17-23 dBsm.

Figure 3.14 shows the TRCS of IB6 versus wind direction based on the simulated SAR images. The TRCS calculated from the real SAR image and the measured wind direction of 352˚ is very close to the simulation and the maximum SSIM index has been found at 337˚ in Figure 3.11. What is noticeable about this plot relative to the previous two is the low variation in the TRCS. The simulated RCS of IB6 only varies by about 2 dBsm, which is much lower than either IB4 or IB5.

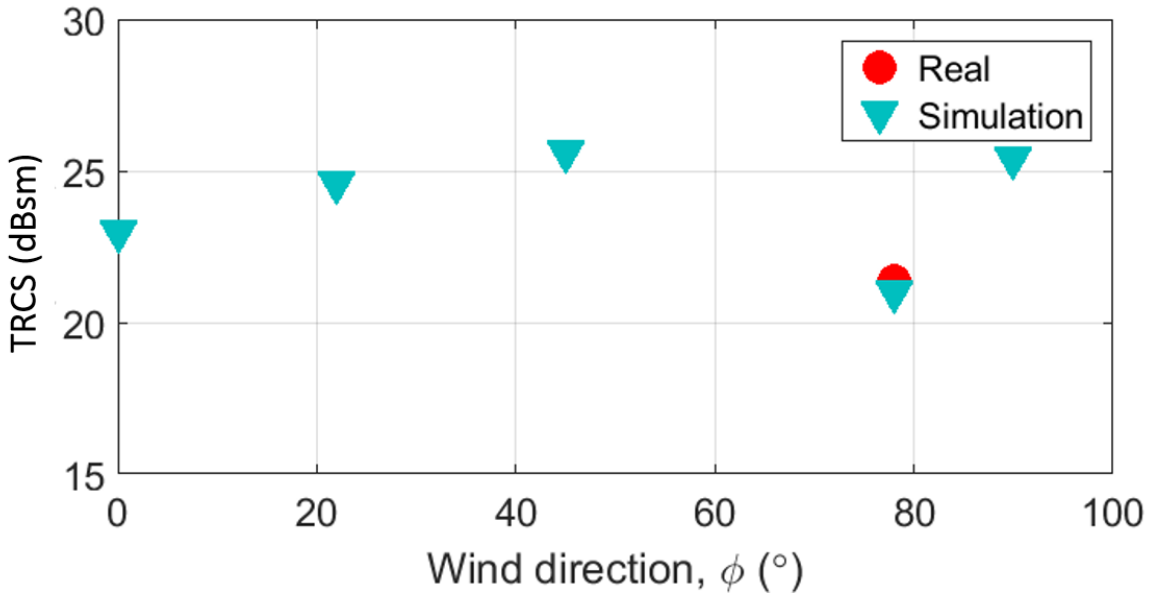

Figure 3.12 TRCS of IB4 over wind direction variation.

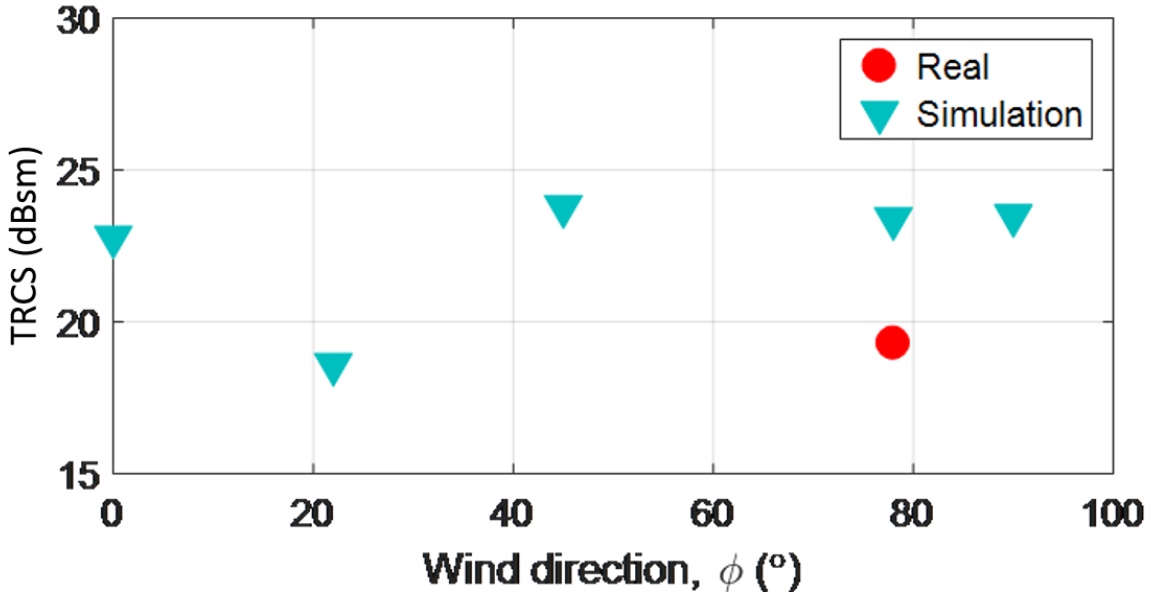

Figure 3.13 TRCS of IB5 over wind direction variation.

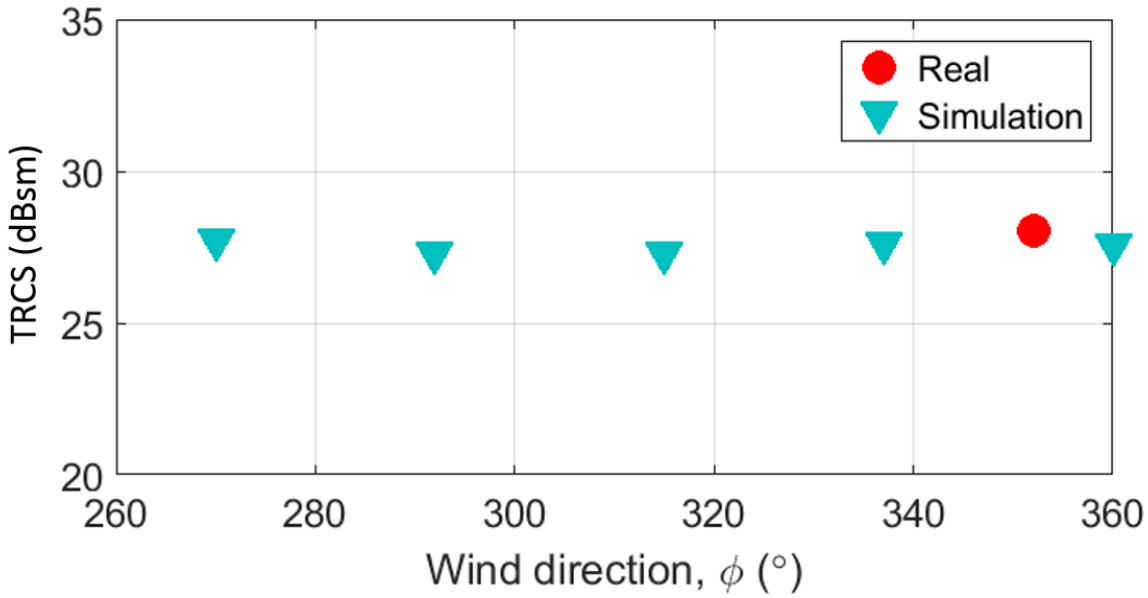

Figure 3.14 TRCS of IB6 over wind direction variation.

3.4.1.4 RMS Deviation

Given that IB6 is much larger than the two other icebergs, the above results suggest that larger icebergs may have a TRCS that varies less with wind direction. To test this hypothesis, two larger versions of IB5 were created by scaling the size of the 3D profiles by a factor of 1.4 and 1.8 respectively in all directions. The TRCS of the scaled versions of IB5 (IB5-SC1 and IB5-SC2) are plotted in Figure 3.15. The TRCS varied by 0.81 dBsm for IB5-SC1 and 1.4 dBsm for IB5-SC2. Note that the two larger versions of IB5 have much lower RCS variation relative to the smaller IB5.

The TRCS variation is further summarized in Figure 3.16, showing the root mean square (RMS) deviation of the three icebergs with wind direction. The deviation has been calculated taking the differences between simulated and real values. This deviation was then normalized with respect to the real value and the RMS deviation calculated as a percentage. It is noticeable that the smallest iceberg (IB5) has the largest variation (19%), whereas the variation is smallest for the largest berg, IB6 (2%). To further confirm this trend, normalized deviation is also plotted for the up-scaled versions of IB5. Both bergs also show lower relative variation with IB5-SC1 at 1.22% and IB5-SC2 at 2.14%.

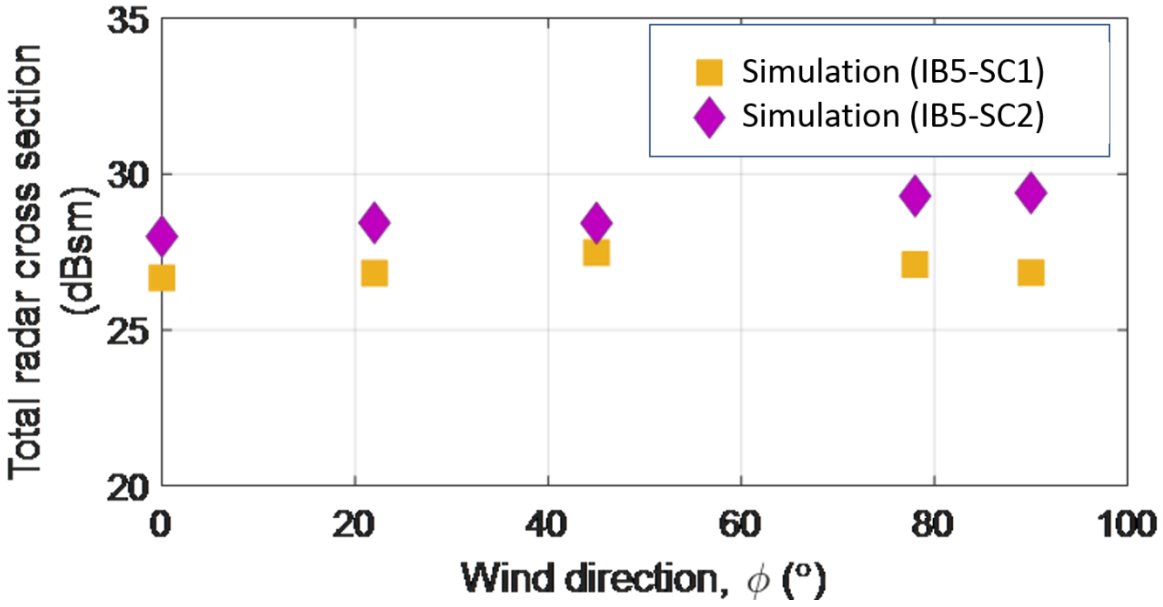

Figure 3.15 TRCS of scaled versions of IB5, showing variation over wind direction.

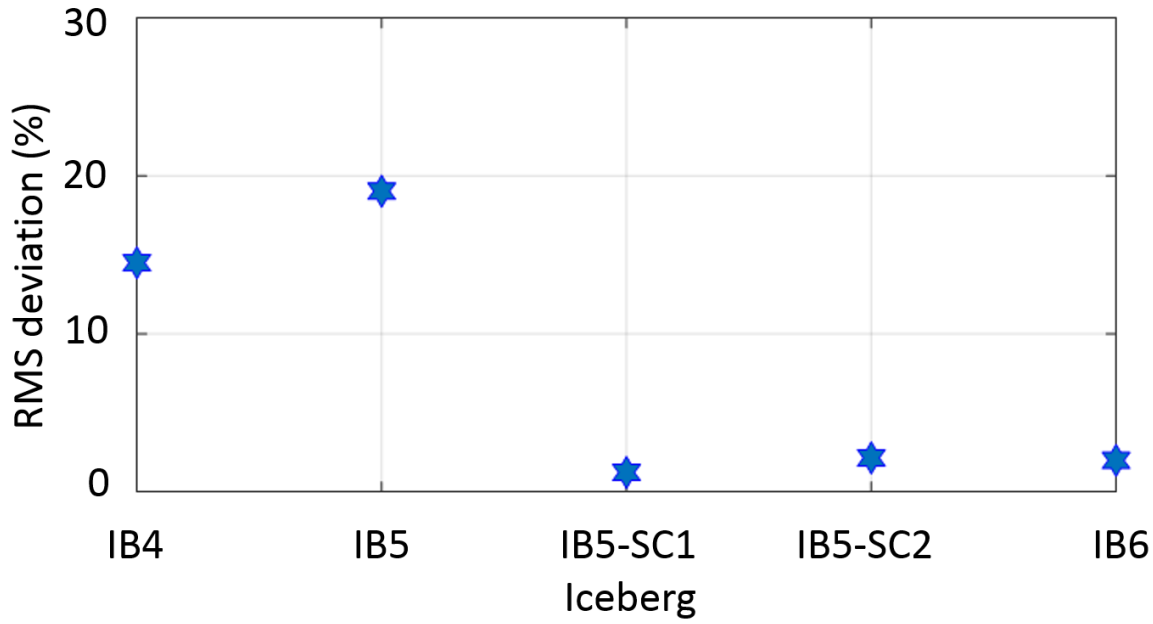

Figure 3.16 RMS deviation of TRCS measure of the icebergs.

3.4.2 Varying Wind Speeds

The objective of this section is to demonstrate EM model's response as wind speed changes. Increasing wind speeds translate into increasing ocean clutter. GRECOSAR simulations were generated to see the

effect of wind speeds on SAR iceberg targets. Ocean parameters were configured to produce mean ocean clutter levels defined by CMOD4 wind speeds. Significant wave height, h_s was kept constant at 0.04 m and wave period T was varied. Figure 3.17 (bottom) shows the wave period variation with wind speed. The wind speeds were translated by the CMOD4 model based on the mean ocean clutter generated at FQ1W mode and 0° wind direction with respect to RADAR look direction CW. The icebergs' EM model response for 7.2 m/s wind speed has already been discussed in previous sections.

Figure 3.17 (top) shows the TRCS of the icebergs at varying wind speeds. These simulations show that, for the most part, increasing wind speed (and clutter) provides a decreasing TRCS trend. This is a satisfying result since a higher level of diffuse ocean/iceberg backscatter around the perimeter of the berg may end up reducing the total berg RCS by destructive interference. Taking the example of IB6, this iceberg has a consistently decreasing trend in RCS with wind speed, with TRCS varying by 2.5 dBsm. This iceberg has steep sides so it will have a dominant double bounce scatter on the side of the berg that faces the radar. This double bounce scatter could conceivably decrease with diffused destructive interference as the ocean roughness increases. In the case of IB4 and IB5, the trend is generally decreasing with wind speeds, except in the case of 5 m/s for IB5 and 10 m/s for IB4 (1.32 dBsm). A possible explanation for this discrepancy in the trends is the shape of these two icebergs. IB6 is the largest icebergs and has smooth/steep sides, whereas the two smaller icebergs (IB4, IB5) have irregular sides. The irregularity of these bergs' sides might, at times, form constructive interference at the leading edge of the icebergs for certain wind speeds. The TRCS variation is 1.32 dBsm for IB3 and 3 dBsm for IB5.

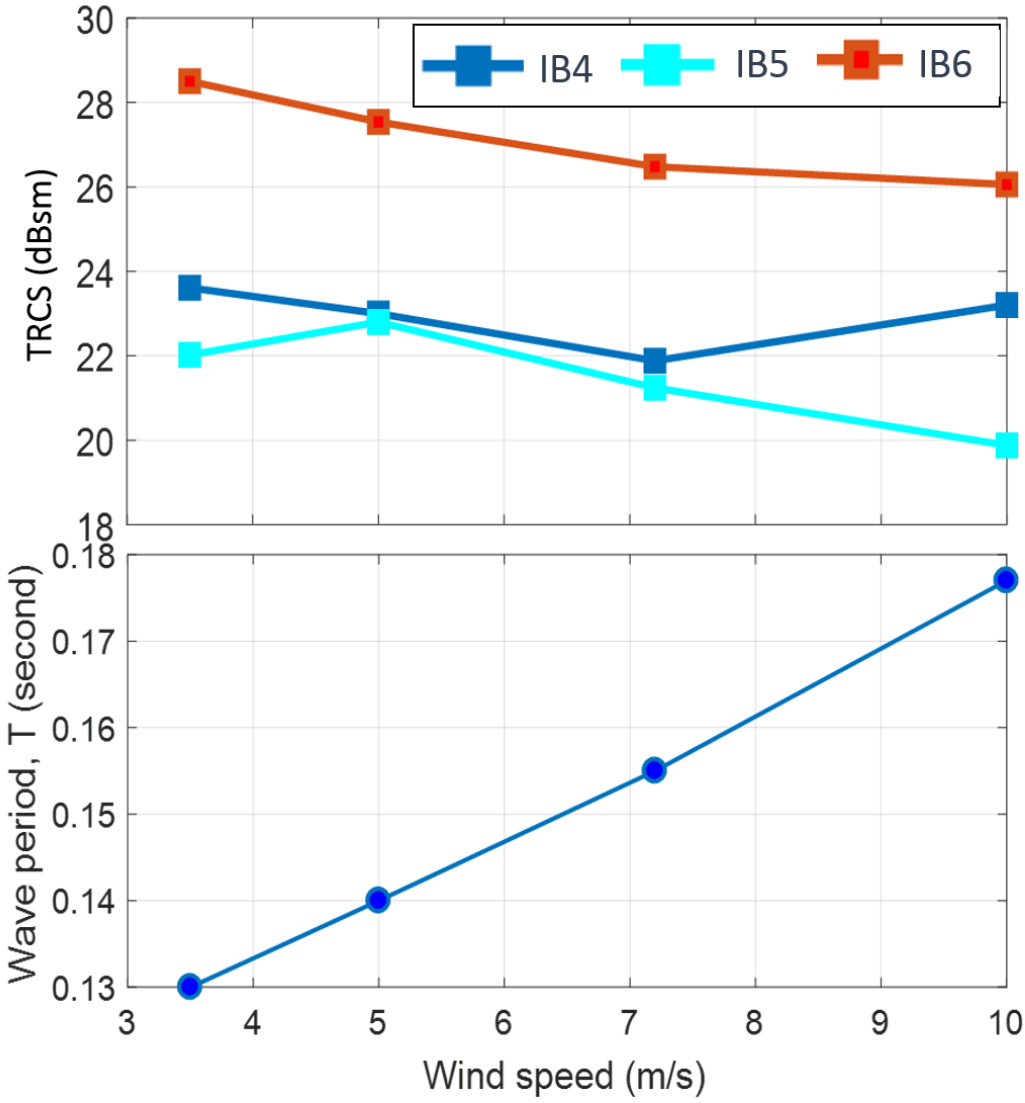

Figure 3.17 TRCS of icebergs and wave period variation at different wind speeds.

3.5 Polarimetric Decomposition Comparison

Given that the three icebergs being examined here were under significant deterioration (melt) during the field program, it was speculated that the surface water melt contributes to dominant surface backscatter rather than the dominant volume backscatter that might be seen in glaciers. In order to test this hypothesis, the polarimetric properties of the simulated SAR images have been examined more closely. Specifically, polarimetric decompositions, based on the full polarimetric image data, have been generated to examine

the different SAR scattering mechanisms. In this study, the real and simulated SAR images of the icebergs have been processed in the form of Pauli decompositions according to (Lee, Grunes, & Kwok, 1994) .

In Figure 3.18, the Pauli decompositions of the three icebergs have been shown in terms of surface, double bounce and volume scattering components. The simulated images are shown at the wide coloured bars, while the real images are shown at the narrow white bars. Simulated SAR images were generated for the wind direction that was measured by local weather station. Power components in the bar chart are expressed as a percentage of total power from surface, double-bounce and volume scattering. For all the GRECOSAR iceberg simulations, the percentages assigned to each scattering type closely follow that of the real SAR image data, as seen in Figure 3.18. Double bounce scattering (in cyan) is maximum for IB6, which is the biggest iceberg and has largest dihedral corner among the three icebergs shown here. Although GRECOSAR cannot simulate multi-layer volume backscatter, considerable volume scattering (in yellow) is seen from the simulations. This is likely due to diffuse scattering produced from the superposition of multiple out-of-phase surface scatterers. In addition, mathematically, volume scattering is proportionate to the HV component and any diplane oriented at 45˚ line of sight (LOS) direction can produce HV by definition (Haykin et al., 1994). Physically, icebergs have a complex geometry with many scattering features, and thus HV backscatter may be produced as a result.

Given the significant surface and double bounce scattering in both the real SAR and GRECOSAR simulated scenes, it is speculated that the surface melt layer is largely responsible, and that for these icebergs, the lack of a GRECOSAR volume scattering component is less of a concern for actively melting icebergs. This adds significant credibility to the use of the GRECOSAR simulations for practical applications.

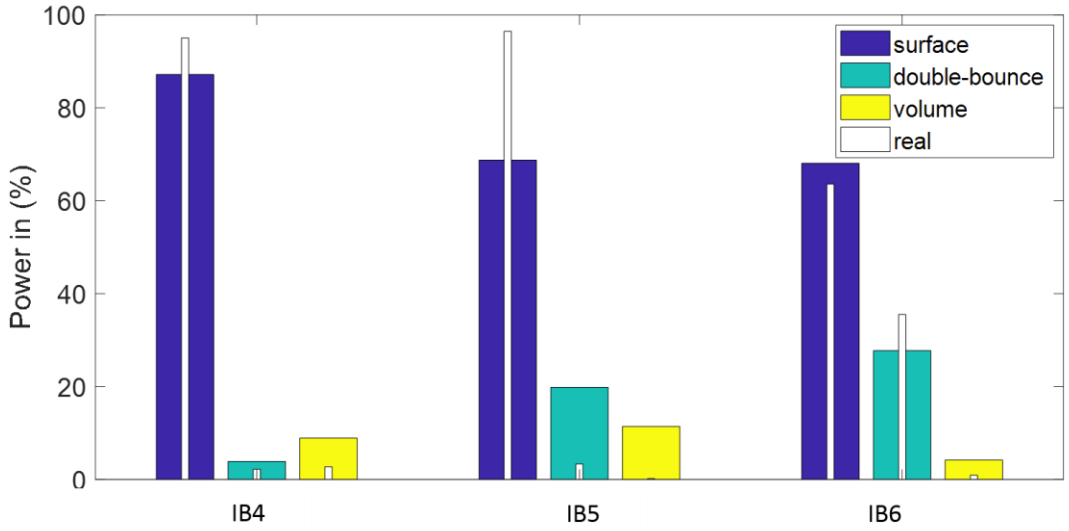

Figure 3.18 Comparison of Pauli decomposition of simulated and real SAR images of the three icebergs IB4-IB6.

3.6 2D Iceberg Backscatter Model

Given the results in the previous section, further analysis was conducted on the expected percentages of surface and volume scatter in an actively melting iceberg. The analysis was performed by deriving a simple two-dimensional multilayer backscatter model, as a supplement to the 3D GREECOSAR simulations. In this 2D model, analysis is simply given to the amount of radar backscatter rather than deriving detailed SAR image simulations.

As mentioned in the Introduction section, 2D backscatter modelling has been reported for sea ice (Partington & Hanna, 1994), snow covered sea ice (Komarov et al., 2015; Komarov et al., 2017) and snow pack layer (Longepe et al., 2009; Matzler et al., 1984; Phan et al., 2012) . The sea ice layer is primarily modelled with cylindrical shaped brine, and spherical air bubble inclusions embedded in a fresh ice medium (Partington & Hanna, 1994) . The snow medium is modelled by an air medium hosting densely packed water and ice inclusions (Longepe et al., 2009; Matzler et al., 1984; Phan et al., 2012).

Icebergs are composed of densely packed snow (Ulaby et al., 2014) and can be modeled simply as fresh ice stuffed with air bubbles as shown in Figure 3.19. The iceberg melting layer will be modeled as a thin layer on top of the iceberg made of fresh water shown in Figure 3.19.

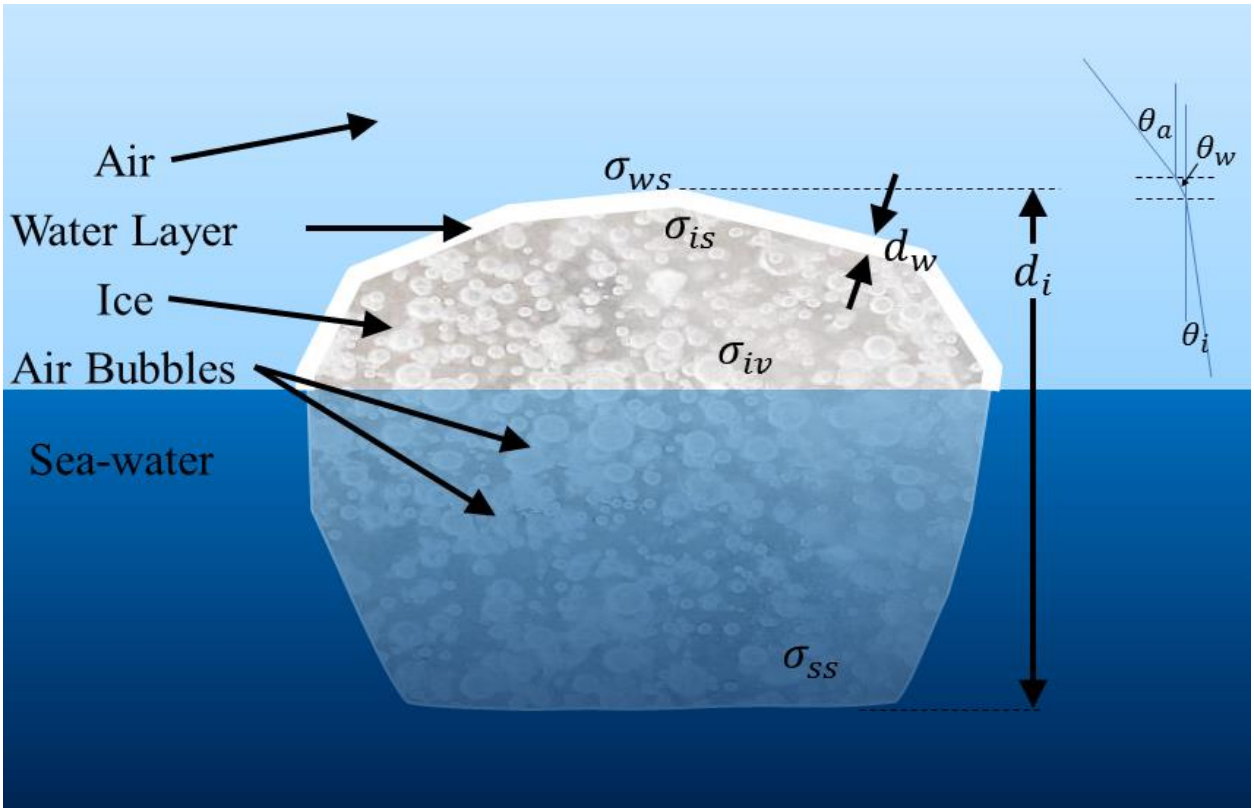

Figure 3.19 Iceberg model consisting of melt layer on top.

3.6.1 Mathematical Model

Total backscattering components coming from the various layers can be written as following, similar to (Partington & Hanna, 1994).

$$\sigma^0 = \sigma^0_{ws} + \sigma^0_{is} + \sigma^0_{iv} + \sigma^0_{ss} \tag{3.1}$$

where,

σ^0_{ws}= surface scattering from air-water interface

σ_{is}^0= surface scattering from water-ice interface

σ_{iv}^0= volume scattering from ice volume

σ_{ss}^0= surface scattering from ice-sea water interface

Surface scattering contributions between the air-water interface are computed by the integral equation method (IEM) for small surface roughness approximation, as given in (Fung, Li, & Chen, 1992). The VV and HH normalized radar cross sections are expressed as:

$$\sigma_{VV}^0 = 8k^4\sigma^2 \left| \frac{R_V \cos^2\theta + \sin^2\theta(1+R_V)^2}{2} * \left(1 - \frac{1}{\varepsilon_r}\right) \right|^2 W(-2k_x, 0) \tag{3.2}$$

$$\sigma_{HH}^0 = 8k^4\sigma^2 |R_H \cos^2\theta|^2 W(-2k_x, 0) \tag{3.3}$$

where,

k = wave number in the incident medium;

θ = incidence angle

σ = rms height (m) of the surface;

ε_r = permittivity ratio between medium 2 to 1;

k_x = wave number projected into medium 1 in horizontal direction;

R_V = Fresnel reflection coefficient for vertical polarization (Ulaby et al., 2014); and

R_H= Fresnel reflection coefficient for horizontal polarization (Ulaby et al., 2014).

$W(-2k_x, 0)$ is the spectrum of height correlation function taken from (Komarov et al., 2017);

$$W(q, 0) = \frac{2\pi L^2}{(1+q^2L^2)^{1.5}} \tag{3.4}$$

Where,

L = correlation length of surface roughness (m).

Surface scattering from water-ice interface is computed by Radiative Transfer Model (RTM) as given in (Partington & Hanna, 1994):

$$\sigma_{is}^{0} = \sigma_{is1}^{0} T_{a_{w1}} T_{a_{w2}} exp(-\frac{2\beta_w d_w}{cos\,\theta_w}) \tag{3.5}$$

where,

σ_{is1}^{0} is scattering at the interface of two media computed by (3.2) and (3.3);

T_{xyz} is the transmission coefficient between medium x and y and z=1 for x to y medium 2 means y to x medium; and

$\beta_{xe} = \beta_a + \beta_s$ is the extinction coefficient composed of absorption and scattering coefficient. $x = w$, i, s subscript for the medium.

Similarly for the ice-sea water interface (Partington & Hanna, 1994),

$$\sigma_{ss}^{0} = \sigma_{ss1}^{0} T_{aw1} T_{aw2} T_{wi1} T_{wi2} \exp\left(-\frac{2\beta_i d_i}{\cos\theta_{\mathrm{i}}}\right) \exp(-\frac{2\beta_w d_w}{\cos\theta_{\mathrm{w}}}) \tag{3.6}$$

The volume scattering component coming from the iceberg surface is given by (Partington & Hanna, 1994)

$$\sigma_{iv}^{0} = \sigma_{v}^{0} T_{aw1} T_{aw2} T_{wi1} T_{wi2} \left(\frac{1 - exp\left(-\frac{2\beta_i d_i}{\cos\theta_{\mathrm{i}}}\right)}{\frac{2\beta_i d_i}{cos\theta_i}} \right) \exp(-\frac{2\beta_w d_w}{\cos\theta_{\mathrm{w}}}) \tag{3.7}$$

σ_{v}^{0} is the scattering from all the air bubbles in the iceberg (Gray & Arsenault, 1991) :

$$\sigma_{v}^{0} = \sigma_v n \rho_{am} \sin\theta \tag{3.8}$$

where,

n = air bubble density per cubic meter; and

ρ_{am}= approximate range-ambiguous distance, the extent by which the volume scattering spreads (it will be assumed 10 m according to (Gray & Arsenault, 1991)).

Scattering from individual air bubbles in an iceberg volume is considered as Rayleigh scattering (Gray & Arsenault, 1991):

$$\sigma_v = 4\pi r^6 k^4 \left|\frac{\varepsilon_{air} - \varepsilon_{ice}}{\varepsilon_{air} - \varepsilon_{ice}}\right|^2 \tag{3.9}$$

where,

r = radius of air bubble (m); and

k = wavenumber in iceberg media whose effective permittivity can be computed by a dielectric mixture model of ice and air (Ulaby et al., 2014):

$$\varepsilon_{ib} = \varepsilon_i + 3v\varepsilon^* \frac{\varepsilon_{air} - \varepsilon_{ice}}{\varepsilon_{air} - \varepsilon^*} \tag{3.10}$$

where, $\varepsilon^* = \varepsilon_{ice}$ according to(Partington & Hanna, 1994)

The extinction coefficients will be computed as:

$$\beta_a = 3vk \frac{\varepsilon''}{|\varepsilon + 2|^2} \tag{3.11}$$

$$\beta_s = 2vk^4 r^3 |K|^2 \tag{3.12}$$

$$K = \frac{\varepsilon - 1}{\varepsilon + 2} \tag{3.13}$$

$$\varepsilon = \frac{\varepsilon_{air}}{\varepsilon_{ice}} \tag{3.14}$$

3.6.2 Model Parameters

All the necessary parameters used in the 2D mathematical iceberg backscatter modeling, as described above, have been tabulated in Table 3.3. The model is designed for C-band frequency (F_C). A 30 m thick iceberg (d_w) has been assumed. The melt water thickness (d_w) and incidence angle (θ_{air}) are model variables as it is the objective to see the sensitivity of backscatter as the melt water changes. Other parameters in Table 3.3 have been set according to the references.

Table 3.3 Iceberg backscatter model parameters.

Parameter	Value	Parameter	Value
F_C (GHz)	5.4	d_w (mm)	0.1~1
θ_{air}(˚)	10~60	d_w (m)	30
ε_i	1	ε_{ib}	1.75 - 0.0018i
ε_{ice}	3.15 with loss tangent 2x10^{-3} (Haykin et al., 1994)	ε_w	65.8-36.5i calculated at 0˚, F_C (Meissner & Wentz, 2004)
n (m^3)	1.18×10^8 (Gray & Arsenault, 1991)	σ_w (mm)	Assumed same as σ_i
r (mm)	1 (Gray & Arsenault, 1991)	L_w (cm)	Assumed same as L_i
σ_i (mm)	1.5 (Partington & Hanna, 1994)	σ_s (mm)	Assumed same as σ_i
L_i (cm)	8 (Partington & Hanna, 1994)	L_s (cm)	Assumed same as L_i

3.6.3 Model Results

The iceberg model and parameters described above have been used to predict the effect of the water melt layer on the SAR backscatter. Figure 3.20 shows the backscattering components from the interfaces within the iceberg for a very thin melt layer (0.1 mm) versus incidence angle. The major backscatter contribution comes from the top melt water surface. Although the melt layer is very thin, its high dielectric constant reflects most of the energy. The next significant backscatter contribution increase is from the water-ice interface, and then from the ice-sea water interface at the bottom of the iceberg. Air bubbles inside the iceberg also contribute to the backscatter, but for this bubble density, the backscatter is low. With increasing

incidence angle, the surface scattering components drop rapidly, whereas the volume scattering component only drops a little. This is due to the relative symmetry of the air bubbles with respect to varying incidence angle.

The effect of melt water layer thickness is also explored. In Figure 3.21, the melt water layer thickness is increased to 0.5 mm, and thence to 1 mm in Figure 3.22. In each of these cases, the increase in backscatter produces a slightly increased backscatter from the top two layers, and slightly lesser from the other volumetric sources.

Given the results of these figures, it seems clear that the surface backscattering will dominate for actively melting icebergs, and therefore, GRECOSAR seems to be well suited to deriving realistic SAR simulations for these types of bergs.

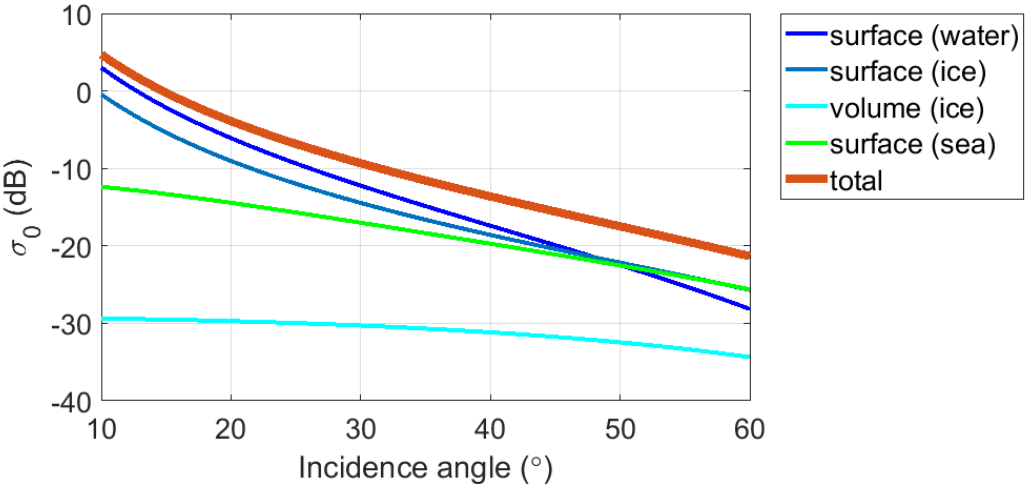

Figure 3.20 Scattering components from iceberg layers for 0.1 mm melt water layer in HH polarization channel.

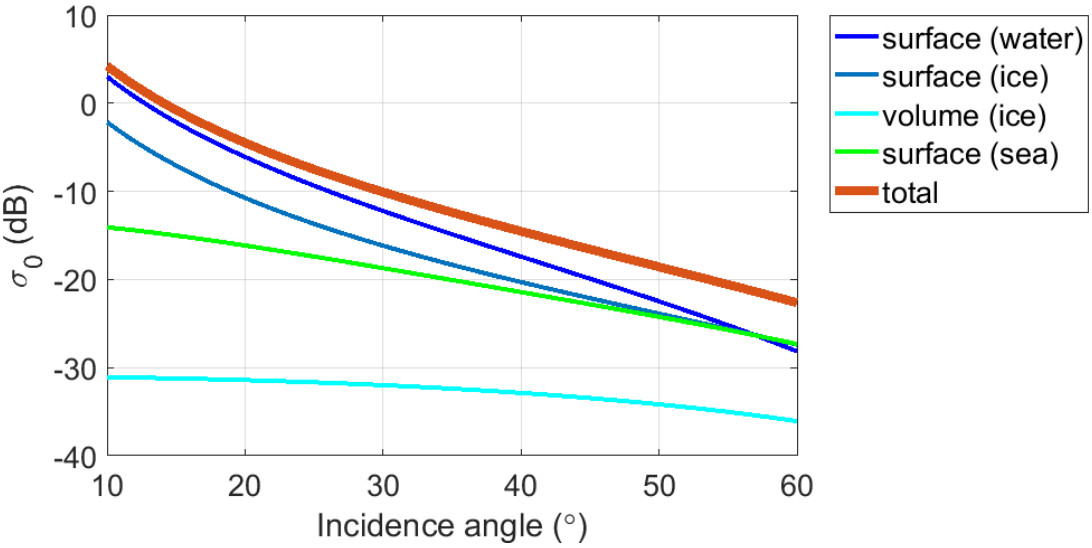

Figure 3.21 Scattering components from iceberg layers for 0.5 mm melt water layer in HH polarization channel.

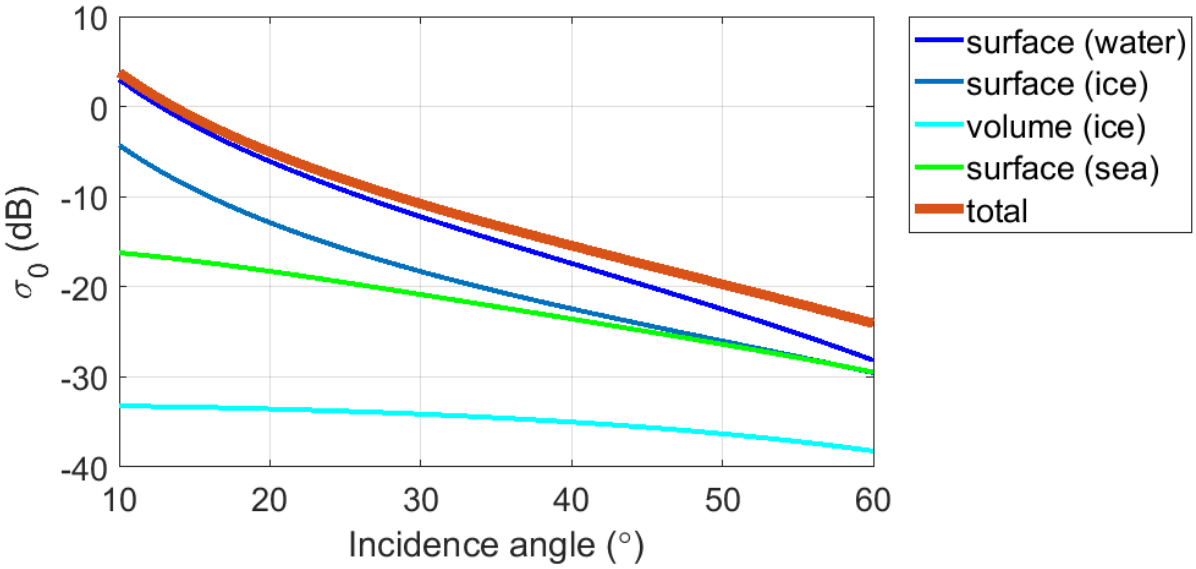

Figure 3.22 Scattering components from iceberg layers for 1 mm melt water layer in HH polarization channel.

3.7 Discussion

An EM backscatter model, based on the simulation software GRECOSAR, has been presented and compared with ground-validated data for QP RADARSAT-2 imagery for several iceberg case studies. SAR

imagery of icebergs was captured over Bonavista, NL, Canada and then compared with simulated images generated by GRECOSAR. Simulated images were generated for varying wind speeds and directions.

Simulated SAR signatures of the same iceberg were shown to vary with wind direction. Wind direction was also shown to change the backscattering pattern at the iceberg-ocean interface and resulted in a pattern change in low intensity pixels surrounding the iceberg perimeter. The change in the pixel pattern has been quantified with respect to the real SAR imagery using the SSIM index. Maximum SSIM index locations suggest closest simulation to the real SAR scenario. The TRCS of an iceberg was also shown to vary with wind direction. It was also observed that, with an increase in iceberg size, the TRCS variation decreases.

The effect of wind speed on iceberg backscatter was also explored. Low wind speed (3.5 m/s) generates less clutter and results in brighter target backscatter relative to the same iceberg simulated in a higher wind speed of 7.2 m/s.

Given that the SAR signature and TRCS of icebergs vary with wind speed and direction, this suggests that the development of a statistical iceberg classifier would benefit greatly from a large dataset with a variety of meteorological conditions. This type of a dataset, with a large volume of targets and a large variation in wind speeds and direction, may be challenging and costly to collect manually. This suggests that the generation of training data sets from an EM backscatter model of icebergs could be very useful in designing a robust iceberg/ship classifier. Using the same 3D profile of an iceberg, a large variety of iceberg targets could be generated by simply varying the wind speed and direction in the EM model. With a large number of 3D iceberg profiles, a very large dataset of SAR training data could be generated for a statistical classifier.

The GRECOSAR backscatter model was also tested by examining the polarimetric backscatter properties of various iceberg targets. Pauli decomposition results for the simulated SAR iceberg targets were compared with decomposition results from real SAR data; the comparison was considered very favourable. Given that the GRECOSAR simulations are comparable to the real SAR data when considering backscatter

mechanisms, this suggests that the macro structure of the iceberg surface is the dominant backscatter, relative to the internal the microstructures (air bubbles) of the iceberg when the surface undergoes melting.

GRECOSAR only simulates backscatter from top single layer surface; the discrepancies between simulated and real data are rather significant when it comes to the spatial distribution of backscattering. However, the TRCS exhibits lower discrepancies and we believe the simulator can still be used to depict general trends for melting icebergs. The iceberg surface was seen to be in a high melt state by the field study team and high backscattering is expected to come from the high dielectric melt water surface assumed in this study. To confirm this, a 2D mathematical backscatter model of an iceberg, considering the melt water layer, was derived. This model shows that, even for a very thin melt water layer (0.1 mm), dominant surface scattering from the melt water layer is present. This indicates that the single layer backscatter model in GRECOSAR should be enough for producing SAR images simulations of icebergs in a high state of melt.

Limitations of this study include the fact that GRECOSAR simulations assume a constant electric permittivity for a particular object. Practically, electric permittivity is a distributed parameter across any volumetric object that limits GRECOSAR's ability for practical representation of any target. Environment factors that might contribute to the difference between real and simulated SAR image results are the slow and natural drifting and rotation of the icebergs over time. In GRECOSAR, the iceberg-ocean intersection representation is simplistic, whereas in the real world, this representation is more complex.

Future recommendations for research include the extension of this work to a larger dataset of icebergs in a more extensive range of incidence angles. In particular, only three 3D profiles were used for a narrow incidence angle range. It is recommended that 3D profiles be collected using satellite incidence angles that are more varied. It is also recommended that the GRECOSAR simulations be tested in a machine learning context to see the value of these simulations for SAR ship and iceberg discrimination.

3.8 Acknowledgment

The authors would like to thank Carl Howell, Mark Howell, Pamela Burke of C-CORE for their help in the data processing and interpretation. Mark Howell also helped in graphics preparation. The authors would also like to thank Defence R&D Canada for access to RADARSAT-2 images. These images were made available via a Multi-User Request Form (MURF) agreement with the Government of Canada.

3.9 References

Fung, A. K., Li, Z., & Chen, K. (1992). Backscattering from a randomly rough dielectric surface. *IEEE Transactions on Geoscience and Remote Sensing, 30*(2), 356-369.

Gray, A. L., & Arsenault, L. D. (1991). Time-delayed reflections in L-band synthetic aperture radar imagery of icebergs. *IEEE Transactions on Geoscience and Remote Sensing, 29*(2), 284-291.

Komarov, A. S., Isleifson, D., Barber, D. G., & Shafai, L. (2015). Modeling and measurement of C-band radar backscatter from snow-covered first-year sea ice. *System, 8*, 9.

Komarov, A. S., Landy, J. C., Komarov, S. A., & Barber, D. G. (2017). Evaluating scattering contributions to C-band radar backscatter from snow-covered first-year sea ice at the Winter–Spring transition through measurement and modeling. *IEEE Transactions on Geoscience and Remote Sensing, 55*(10), 5702-5718.

Lee, J., Grunes, M. R., & Kwok, R. (1994). Classification of multi-look polarimetric SAR imagery based on complex wishart distribution. *International Journal of Remote Sensing, 15*(11), 2299-2311.

Li, H., He, Y., & Wang, W. (2009). Improving ship detection with polarimetric SAR based on convolution between co-polarization channels. *Sensors, 9*(2), 1221-1236.

Longepe, N., Allain, S., Ferro-Famil, L., Pottier, E., & Durand, Y. (2009). Snowpack characterization in mountainous regions using C-band SAR data and a meteorological model. *IEEE Transactions on Geoscience and Remote Sensing, 47*(2), 406-418.

Matzler, C., Aebischer, H., & Schanda, E. (1984). Microwave dielectric properties of surface snow. *IEEE Journal of Oceanic Engineering, 9*(5), 366-371.

Meissner, T., & Wentz, F. J. (2004). The complex dielectric constant of pure and sea water from microwave satellite observations. *IEEE Transactions on Geoscience and Remote Sensing, 42*(9), 1836-1849.

Partington, K., & Hanna, M. (1994). Modelling radar sea ice backscatter in support of ERS-1 SAR. *EARSeL Advances in Remote Sensing, 3*(2), 42-53.

Phan, X., Ferro-Famil, L., Gay, M., Durand, Y., Dumont, M., Allain, S., & D'Urso, G. (2012). Analysis of snowpack properties and structure from TerraSAR-X data, based on multilayer backscattering and snow evolution modeling approaches. *arXiv Preprint arXiv:1211.3278,*

Pierson, W. J., & Moskowitz, L. (1964). A proposed spectral form for fully developed wind seas based on the similarity theory of SA kitaigorodskii. *Journal of Geophysical Research, 69*(24), 5181-5190.

Stoffelen, A., & Anderson, D. (1997). Scatterometer data interpretation: Estimation and validation of the transfer function CMOD4. *Journal of Geophysical Research: Oceans, 102*(C3), 5767-5780.

Touzi, R., Charbonneau, F., Hawkins, R., & Vachon, P. (2004). Ship detection and characterization using polarimetric SAR. *Canadian Journal of Remote Sensing, 30*(3), 552-559.

Ulaby, F. T., Long, D. G., Blackwell, W. J., Elachi, C., Fung, A. K., Ruf, C., . . . Van Zyl, J. (2014). *Microwave radar and radiometric remote sensing* University of Michigan Press Ann Arbor.

Vachon, P. W., & Wolfe, J. (2011). C-band cross-polarization wind speed retrieval. *IEEE Geoscience and Remote Sensing Letters, 8*(3), 456-459.

Vachon, P., Campbell, J., Bjerkelund, C., Dobson, F., & Rey, M. (1997). Ship detection by the RADARSAT SAR: Validation of detection model predictions. *Canadian Journal of Remote Sensing, 23*(1), 48-59.

Wang, Z., Bovik, A. C., Sheikh, H. R., & Simoncelli, E. P. (2004). Image quality assessment: From error visibility to structural similarity. *IEEE Transactions on Image Processing : A Publication of the IEEE Signal Processing Society*, *13*(4), 600-612.

Yam, L. E., Mallorqui, J. J., & Rius, J. M. (2012). Validation of a sea surface model for simulations of dynamic maritime SAR images. Paper presented at the *Geoscience and Remote Sensing Symposium (IGARSS), 2012 IEEE International*, 2813-2816.

Chapter 4 Assessing the Utility of Modelled SAR Images of Iceberg and Ship Targets using a Machine Learning Classifiers

4.1 Introduction

The previous chapters presented EM backscatter modelling of icebergs at Sentinel-1 higher incidence angle (43˚) beam mode and RADARSAT-2 lower incidence angle (19˚) beam mode. The chapters showed good agreement in terms of SAR signature, TRCS and polarimetric decomposition between simulated and real SAR image of the icebergs. An assessment was made on how ocean parameters, including wind direction and speed, could alter the polarimetric behavior of iceberg targets that include SAR signature and TRCS. A mathematical backscatter model of the iceberg considering a melting water layer showed that as little as 0.1 mm melt water could produce maximum backscattering from the surface which further solidify melt water dielectric assumption presented (chapter 3).

So far, an iceberg's EM backscattering properties have been compared in terms of visual SAR signatures and hand-picked radiometric parameters such as TRCS and polarimetric decomposition. This is enough for parameter based simple classifiers but might be insufficient for machine learning based classifiers that can deal with hundreds or thousands of intrinsic parameters. This chapter will show a test of the compatibility of simulated SAR images of icebergs in machine learning based classifiers and thus suggest validation of the EM backscatter model of an iceberg.

The rest of the chapter includes the following sections: "SAR Data Set Collection," "Iceberg/Ship Classifiers," "Comparisons of Classifiers Accuracy," and finally "Discussion." "SAR Data Set Collection" describes rationale and procedure of simulated SAR image generation and real SAR image sourcing. The "Iceberg/Ship Classifiers" section describes data pre-processing, rationale for chosen classifiers such as SVM, RanFor, kNN and NN and software, hardware packages used in this experiment. The "Comparisons of Classifiers Accuracy" section presents classifiers performances with the simulated SAR image data set and gradual mix up with the real SAR data set as training data. Similar performances have been achieved

with only real SAR training data and compared with results from a with simulated data set. The "Discussion" section sums up the article and its findings and as well provides future directions of this work.

4.2 SAR Data Set Collection

4.2.1 Real SAR Image Sourcing

C-CORE has ground truth data of icebergs and vessels available in house. 5000 image data were available for the Kaggle competition, the same data set will be used in this experiment. The SAR images are Sentinel-1 SLC intensity format. Each image comes with HH and HV layers of 75x75 pixels. Images were downsized to 60x60 pixels to make them comparable to the size of simulated SAR images. The images also contain incidence angle information. The incidence angle ranged from 30˚ to 44˚.

4.2.2 Simulated SAR Data Generation

4.2.2.1 Simulation Scene and Parameters

In GRECOSAR simulated SAR images of icebergs and ships were generated. The simulation scene consisted of a 3D model containing an iceberg or ship surrounded by an ocean surface as shown in Figure 4.1.

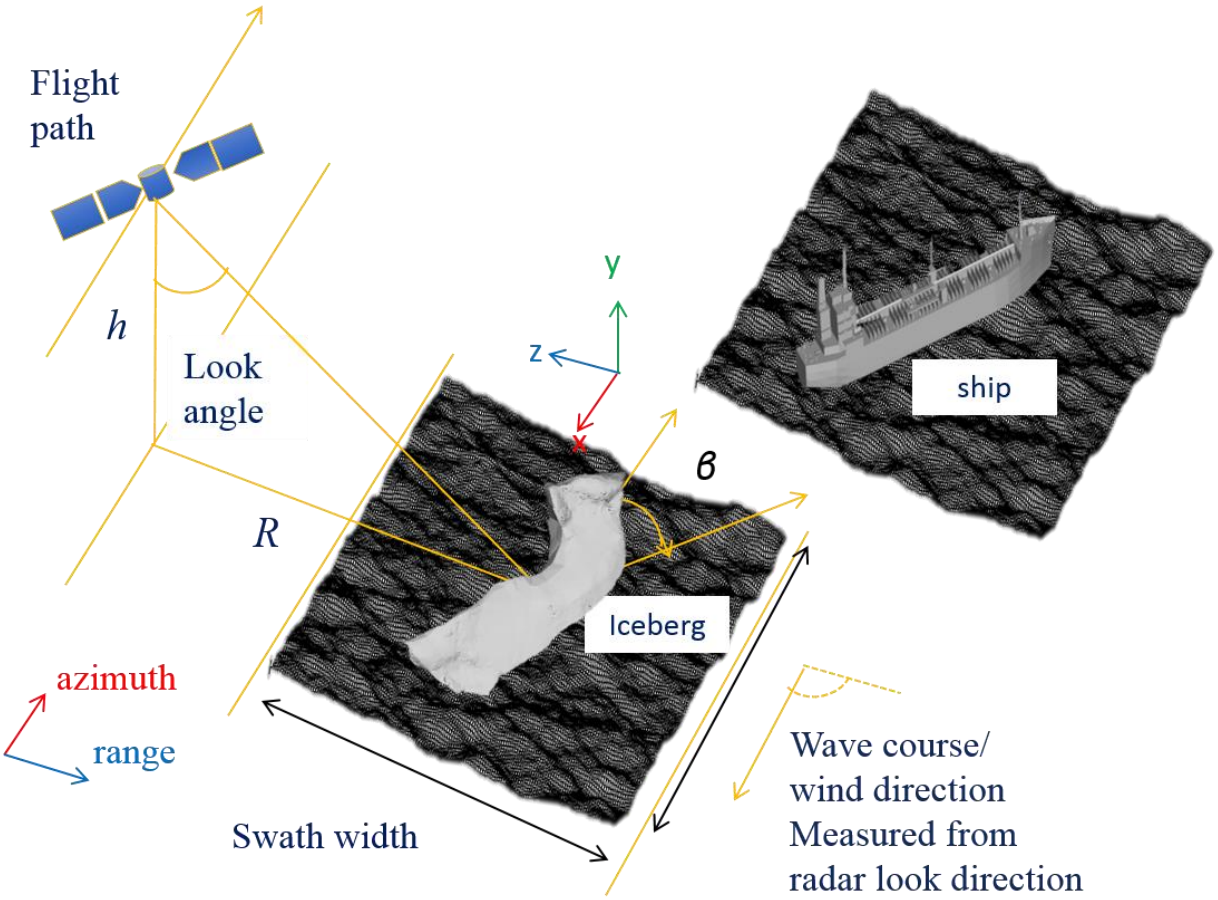

Figure 4.1 Simulation scene and parameters in GRECOSAR.

The objective is to produce simulation scenes that capture all possible phenomena consisting of beam modes, wind speeds, wind directions and target rotations. The satellite parameters were set for Sentinel-1 low incidence angle (IW1) and high incidence angle (IW3) beam modes. Wind parameters that drive the ocean backscattering have been set for high and low wind speeds and for azimuth to range wind directions. Targets have also been varied from 0-90˚ to realistically capture the effect of target rotation in contrast to the image rotation effort to produce augmented data reported in (Jun, Atharva, & Dhruv, 2017). Six icebergs and ships were picked. All these combinations would produce a total of 216 unique simulated SAR images. Other simulations parameters and procedures have been followed as described previously in Chapters 2 and 3. The summary of simulation parameters appears in Table 4.1.

Table 4.1 Summary of simulation parameters.

Parameter	Value
SAR centre frequency	5.405 GHz
Targets	Icebergs= 3, Ships= 3
Scene pixels	60x60
Total image counts	Icebergs=108, Ships=108, Total=216
Incidence angle, (ϕ)	IW1= 33.1˚, IW3= 43.1˚
Wind speed	5 m/s, 10 m/s
Wind direction	0˚, 45˚ and 90˚
Target orientation	0˚, 45˚ and 90˚

4.2.2.2 3D Profiles of Iceberg and Ship targets

3D profiles of the iceberg and ship targets are required to generate simulated SAR images in GRECOSAR. 3D profiles of icebergs were captured using LiDAR and a multi-beam sonar in a field program conducted by a team of C-CORE in June 2017 off the coast of Bonavista, NL, Canada. Three icebergs of small, medium and large sizes were picked for this field program. The measured 3D profiles of the icebergs (designated as IB4, IB5 and IB6) are shown in Figure 4.2. Three vessels were also used, and their CAD models are shown in Figure 4.3. The *Cargo Vessel* model was included in the GRECOSAR package. The *Small Oil Tanker* and *Medium Oil Tanker* models were outsourced from an online CAD model store[4]. The ship models were scaled to the sizes of the icebergs to ensure that target classifiers were not influenced significantly by target size.

[4] http://www.cgtrader.com

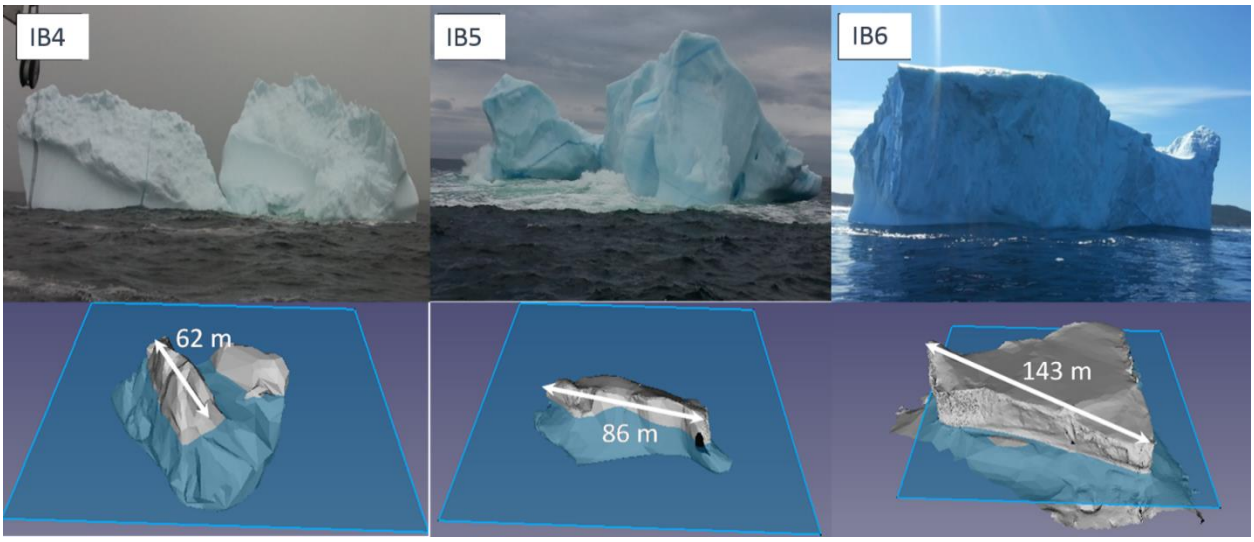

Figure 4.2 Icebergs photos and full 3D profiles showing waterline length.

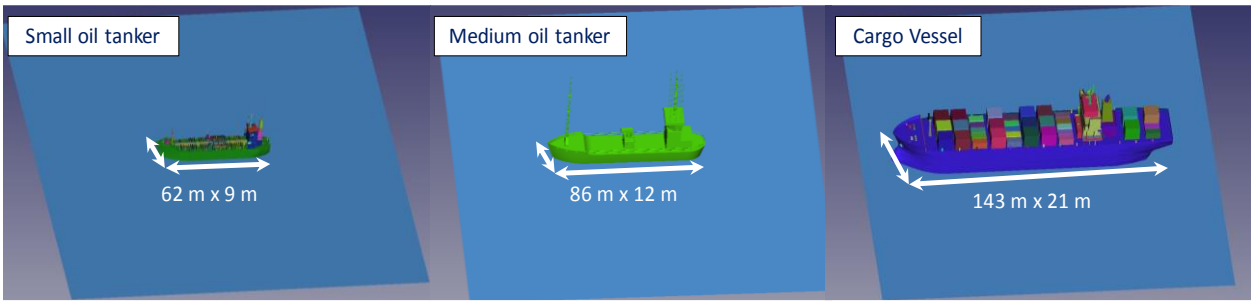

Figure 4.3 CAD models of ships, including waterline length and width.

4.3 Iceberg/Ship Classifiers

Using the dataset of real and simulated SAR targets, a series of image classifiers were developed using the data for training and testing purposes. A brief description of the classifiers and data pre-processing performed for the analysis is discussed in the subsections below.

4.3.1 Software and Hardware

The software package and hardware used in this work have been summarized below:

- MATLAB 2017a academic version
- Work station

- Processor: Core i7 processor with 3.60 GHz speed
- Internal Memory (RAM): 32 GB
- Operating system: 64-bit Windows 7
- GPU: NVIDIA GeForce 337.88

4.3.2 Classifiers

As the central intent of this work is to test the adaptability of a simulated SAR dataset with real data, the focus of the analysis is not on optimizing the classifier design, nor in determining the utility of various classifier techniques for this application. Such an analysis – particularly on this dataset – has been reported in (Power et al., 2018). Rather, classifiers were chosen based on those already used (Jang, Kim, & Lam, 2017) with the same Kaggle target database. All the classifiers were modelled in MATLAB built-in functions. In all the classifiers, 10-fold cross validation has been applied in the training and testing data (Duda, Hart, & Stork, 2012).

4.3.2.1 Support Vector Machine

SVM is very well suited for binary classification as would be good for our case of iceberg/ship classification. SVM finds a hyperplane that separates the two classes with minimum distance margin. SVM sits at the top 10 list according to (Jang et al., 2017). Basic parameters used:

- Classification model: ‘fitcsvm’(The MathWorks, b)
- Kernel Function: radial bias function (rbf)

4.3.2.2 Random Forest

RanFor learns from an ensemble which is divided based on many decision trees and finally votes for classification. RanFor is one of two classifiers in top 10 list that classifies based on decision trees according to (Jang et al., 2017). Basic parameters:

- Classification model: ‘fitctree’ (The MathWorks, c)
- Maximal number of decision splits (or branch nodes) per tree is 7199

4.3.2.3 K-Nearest Neighbour

kNN algorithm looks for k-nearest samples for an object and tags to a class based on maximum voting. According to (Jang et al., 2017) kNN is in the top-10 algorithm list. Basic parameters used for this work:

- Classification model: ‘fitcknn’ (The MathWorks, a)
- Number of weights: 3
- Weights: one weight per observation

4.3.2.4 Neural Network

NN can perform better with high dimensional complex features seen in the image data set. Basic features are:

- Classification app: ‘Neural Net Pattern Recognition’ (The MathWorks, d)
- Number of hidden neurons: 10
- Number of layers: 2

In all the classifiers 10-fold cross validation has been applied in the training and testing data.

4.3.3 Data Pre-processing

As a first step, the matrix elements of each real SAR image, consisting of 75×75×2 (×2 accounts for HH and HV bands) elements, have been clipped to 60×60×2 to make it comparable to the simulated SAR image matrix size. Then, matrix elements were converted to a two layers linear format of 3600×2 and then to a single layer 7200 element vectors. Elements of the HV layer were juxtaposed with HH layer. The linear vectors were then pre-processed in various combinations of band selection, ocean clutter, data

normalization and linearity of the data. Four combinations have been tried based on the parameters shown in Table 4.2. Ocean clutter was masked with a thresholding technique described in chapter 2. Data normalization was performed according to (Jang et al., 2017). Combinations 1-4 were tested using the SVM classifier with 400 randomly drawn real SAR targets, with an equal number of iceberg and ship targets. As can be seen, combination 1 outperforms other combinations, hence this pre-processing combination are used in all subsequent tests.

Table 4.2 Data pre-processing Combinations.

Comb.	Band	Clutter	Normalization	Accuracy
1	HH, HV	yes	Yes	81.5
2	HH, HV	no	Yes	74.7
3	HH, HV	yes	No	81
4	HH (incidence angle >30˚) or HV (otherwise)	yes	Yes	75.7

4.3.4 Accuracy Measure

In the classification process for SVM, RanFor and kNN, the basic steps followed are: classifier model generation, cross-validation on the generated model; and 10-fold loss calculation based on the cross-validation step.

Models parameters were optimized by the 'OptimizeHyperparameters' option in MATLAB aiming to minimize cost function in default 30 epochs for SVM, RanFor and kNN classifiers. Once the 10-fold loss is known (in %), the accuracy can be calculated by deducting the loss from 100. For NN, it measures classifier performance by computing the confusion matrix for training, test and validation data. Accuracy is determined from the MATLAB generated 'all confusion matrix'.

4.4 Comparison of Classifier's Accuracy

Following the steps of data-preprocessing and classifier formation, classifiers were trained based on real and simulated SAR image data and the accuracies were then compared. In the literature, there is no specific mention of the amount of training data that would be required to produce optimal performance for iceberg and ship classifiers. Nonetheless, based on the Kaggle experience, the optimal number of targets should number in the thousands. As the total amount of simulated SAR data is 216, this number will be assumed as a starting point and increased up to 1616 in steps of 200. This number of targets was considered enough to confirm the hypothesis of this paper – that simulated SAR images can be used to augment (or even replace) a real SAR target training dataset.

4.4.1 Accuracy with Real SAR Images as Training Data

Real SAR images of icebergs and ships were randomly drawn from the Kaggle dataset and fed to train the classifiers. The accuracy of the classifiers has been plotted in Figure 4.4 with respect to the increase in the number of training data. As similar pattern for accuracy followed for all the classifiers. The accuracy is maximum when the number of training data are 1016 for SVM and kNN classifiers, 216 for NN and the RanFor classifier peaked at 816 training data.

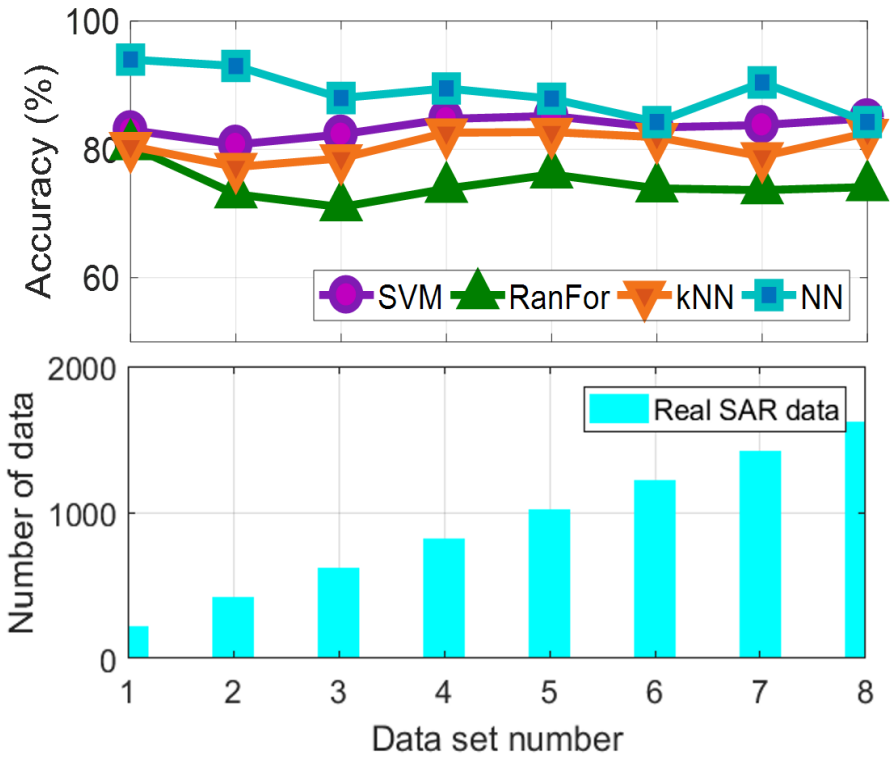

Figure 4.4 Classifiers accuracy with real SAR data as training data.

4.5 Accuracy with Simulated SAR Images as Training Data and Prediction with Real Data

Accuracies were measured first with classifiers trained with the 216 simulated SAR targets. Then, real SAR targets were mixed with the simulated SAR targets into one larger dataset, in increments of 200 targets. In every step, the total number of training targets were made equal to the number for the case of real SAR data. The results have been plotted in Figure 4.5. In the case with only the simulated SAR data (dataset # 1), a high level of accuracy is already observed for all the classifiers in contrast to the result with only the real SAR data. Accuracy numbers of approximately 95%, 93%, 95% and 95% were seen for the SVM, RanFor,kNN and NN classifiers. The explanation for the high accuracy with the simulated SAR images is because the simulated SAR data contains 216 targets generated from only six different 3D profiles whereas the real SAR data contains all distinctly different targets. With the blend of real SAR data with simulated data, the level of accuracy is comparable, and the patterns followed the trend as similarly seen in Figure

4.4. Real iceberg data set containing equal number of training data were passed into the classifiers trained with simulated only (dataset #1) and mixed datasets (#2 to 8) to determine prediction accuracy. This has been shown in Figure 4.5 (middle). High prediction accuracy for icebergs is trending on the right spectrum of the figure (#6 to #8) where trained models were dominated by real data set. Above 85% prediction accuracy is seen for the classifiers trained with purely simulated data (#1) for all the algorithms except kNN. The reason perhaps being that the simulated data contains variability of the 3 icebergs at varying clutter and sensor parameters. It is possible for the real dataset to contain icebergs with more varying sizes and shapes.

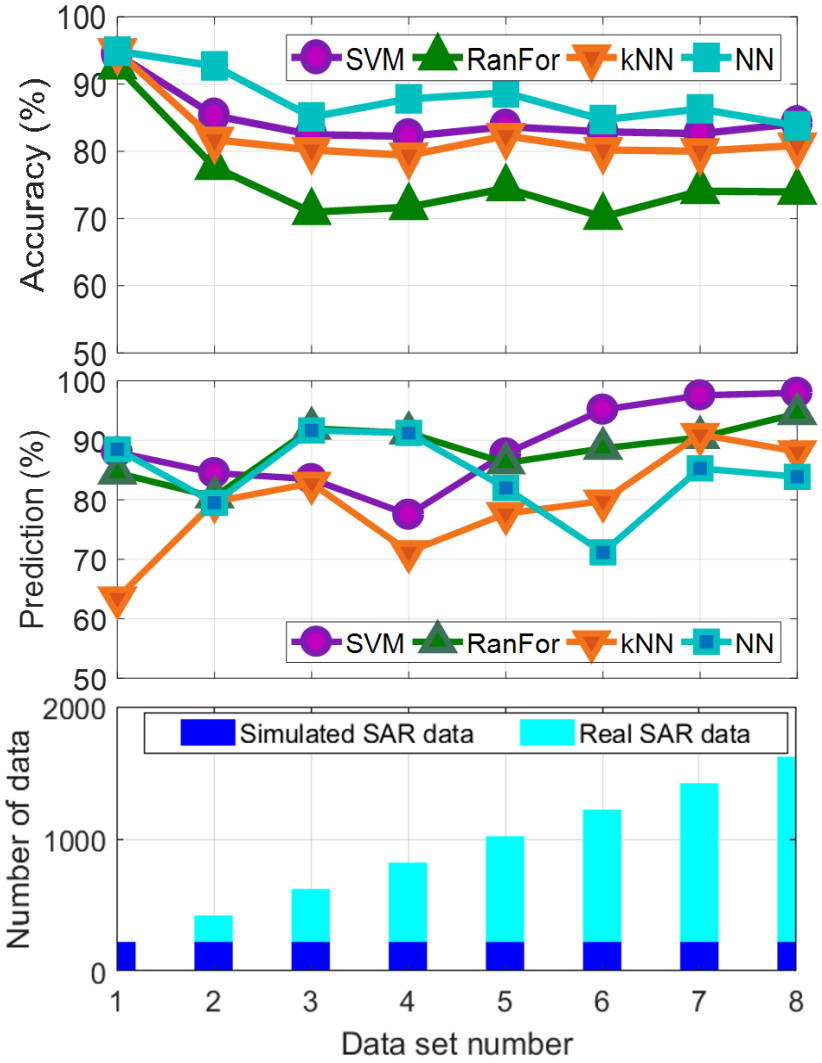

Figure 4.5 Classifiers accuracy (top) and prediction (middle) with simulated and real SAR data mix.

4.6 Accuracy Comparison

As a measure of comparison, 'change in accuracy' was measured for every classifier, keeping the simulated data accuracy result as reference. The results are shown in Figure 4.6. This provides a measure of the accuracy shift from the simulated data alone to results with the mixture of simulated and real data. Another term called 'average absolute accuracy' has also been computed for better insight. This was computed by taking absolute and averaging 'changes' over classifiers at each dataset number. This has been plotted by grey bars in Figure 4.6. In the case with only the simulated dataset (# 1) the margin is the maximum at almost 8%. The reason for this is that the SAR dataset contains full polarimetric information of 6 targets for ranges of scene, geometrical and sensor parameters. That yielded a high accuracy margin with respect to the same number of real SAR data. On the other hand, with real and simulated data mixed, lowest and highest margins were found to be almost 0.6% (# 8) and 2.7% (# 2).

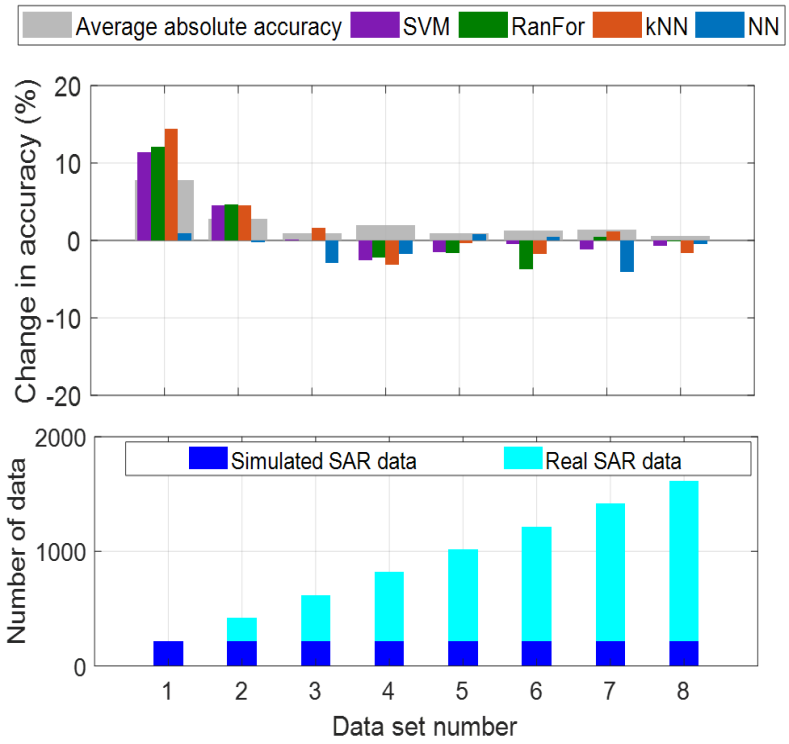

Figure 4.6 Classifiers accuracy comparison.

4.7 ROC Analysis

In addition to the accuracy measure, receiver operating characteristics (ROC) curves have been generated by passing the real data on the classifiers trained by the real and mixed data. ROC curves were generated for the SVM, RanFor and NN based classifiers. It was not possible to generate ROC curves for the kNN classifier because it does not provide the probability of the object that is necessary to generate a false positive rate. Rather it assigns objects directly to a nearest neighbor.

4.7.1 Real Data

Real data containing Iceberg and Ship targets were passed to the classifiers trained by real data and ROC curves were generated. ROC curves have been plotted for SVM, RanFor and NN classifiers in Figure 4.7, Figure 4.8 and Figure 4.9, respectively, and their corresponding area under curve (AUC) measures are shown. A minimum AUC of 99% for SVM, 92% for RanFor and 91% for NN have been calculated.

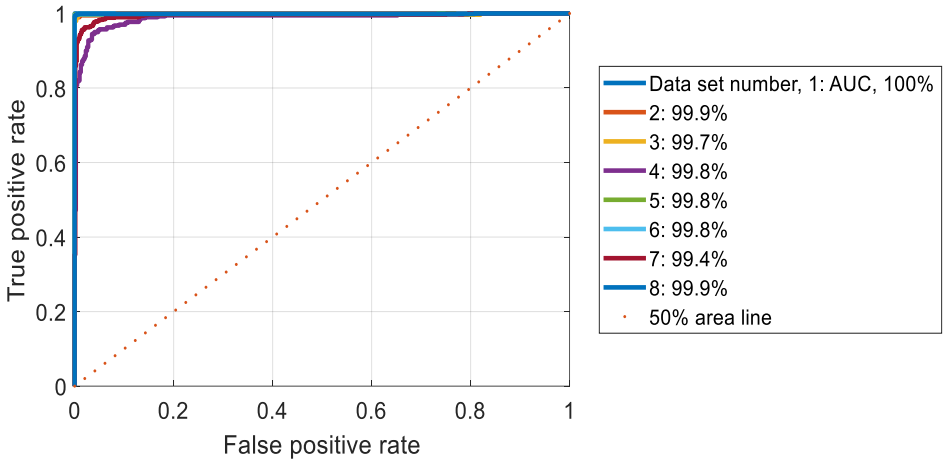

Figure 4.7 ROC and AUC for SVM classifier trained with real data.

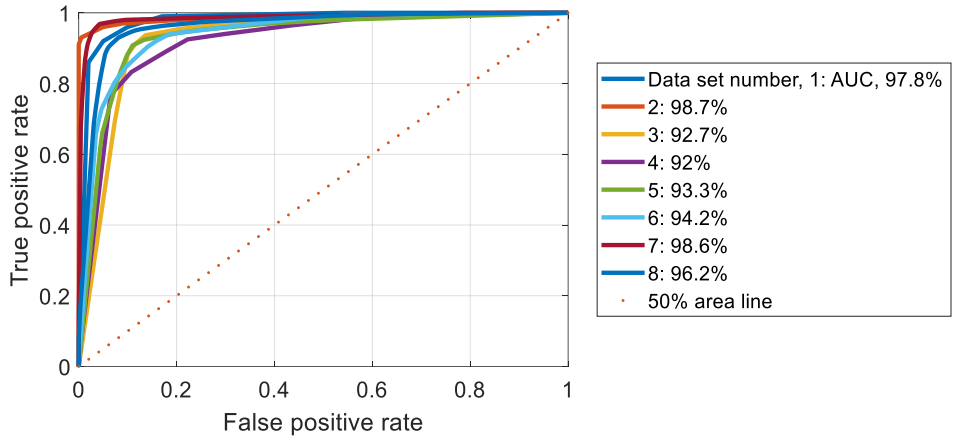

Figure 4.8 ROC and AUC for RanFor classifier trained with real data.

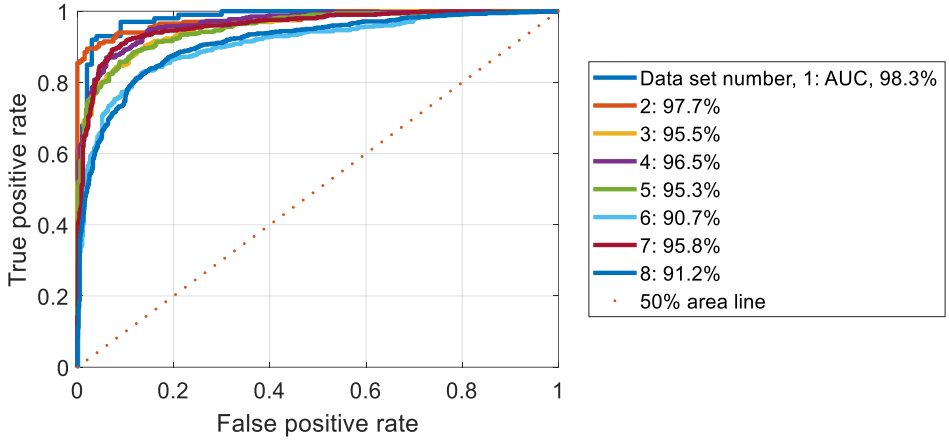

Figure 4.9 ROC and AUC for NN classifier trained with real data.

4.7.2 Mixed Data

Real data containing Iceberg and Ship targets were passed to the classifiers trained by only simulated data (#1) and mixed data (#2-#8) to generate ROC curves. For the SVM classifier (in Figure 4.10), with only a simulated-data-trained classifier, the AUC was calculated to be 48.3% (#1), whereas for the case of mixed data, a minimum of 91.2% is seen (#2). For the case of the RanFor classifier (in Figure 4.11), with only a simulated-data-trained classifier, an AUC was calculated to be 47.5% (#1), whereas for the case of mixed data, a minimum of 71.1% is seen (#2). For the case of the NN classifier (in Figure 4.12), with only the

simulated-data-trained classifier, an AUC of 72.1% was calculated (#1), whereas for the case of mixed data, a minimum of 82.5% is seen (#2).

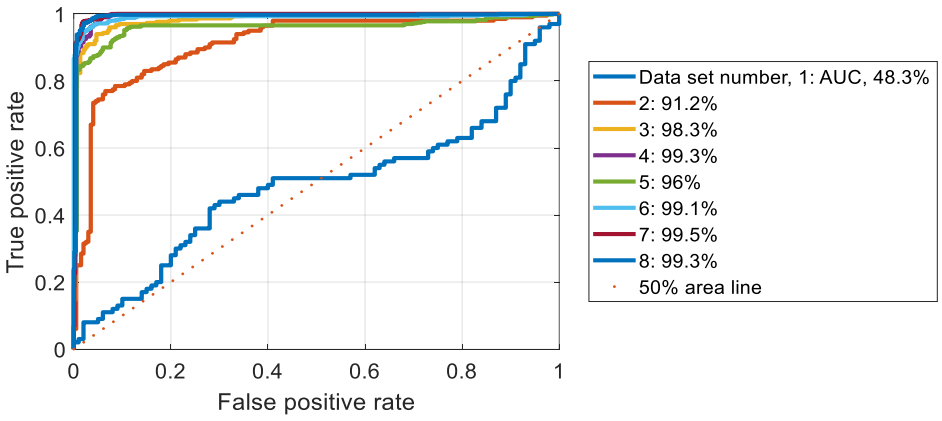

Figure 4.10 ROC and AUC for SVM classifier trained with mixed data.

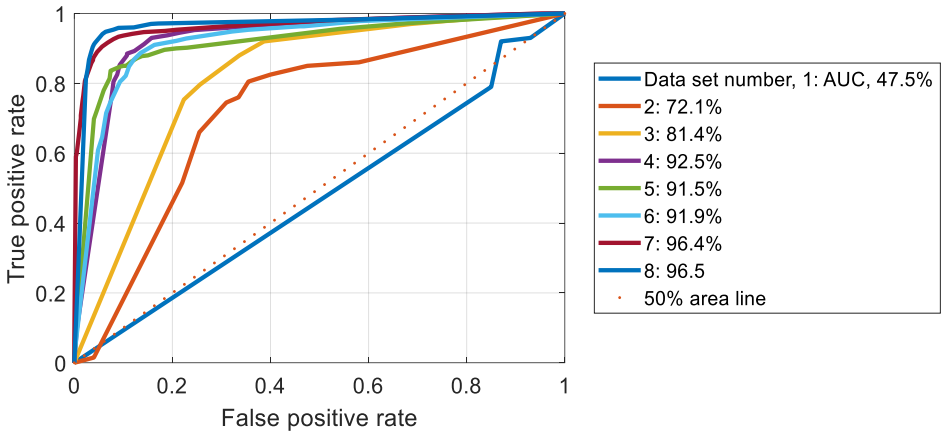

Figure 4.11 ROC and AUC for RanFor classifier trained with mixed data.

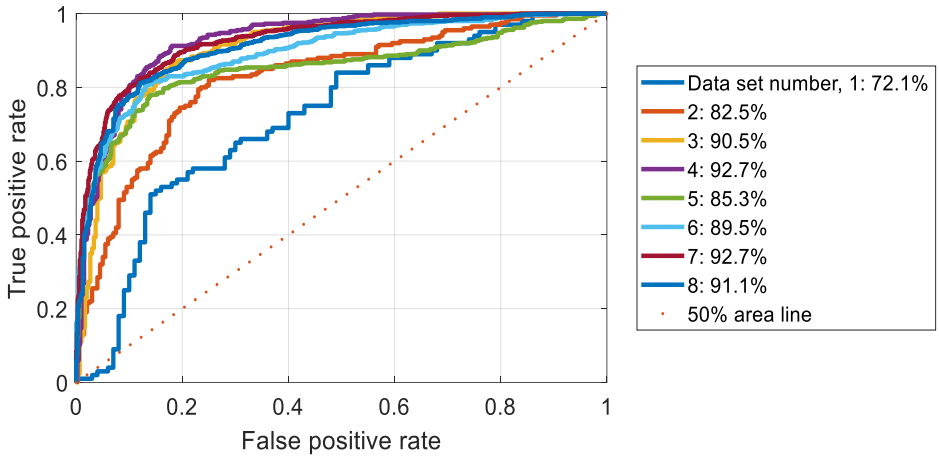

Figure 4.12 ROC and AUC for NN classifier trained with mixed data.

From the above, the following observations can be made:

1. With only simulated data trained classifiers, lower numbers of AUC have been found (close to 50% line) for SVM and RanFor. This is still quite good for the iceberg data which is our main focus considering that a high prediction accuracy for icebergs (above 85%) has been seen. A lower prediction accuracy for the simulated ship targets is to blame for the lowering of the AUC numbers. Thus, the simulated iceberg data could be used to train iceberg/ship classifiers.
2. With only a simulated-data-trained NN classifier, 72.1% AUC has been found. With reference to the main document, the prediction for iceberg targets is above 85%; thus, the lower prediction accuracy for ship targets lowered this value.
3. With mixed-data-trained classifiers, AUC rapidly increased. A minimum of 72.1% was found for the #2 for RanFor classifier. This suggests that simulated iceberg and ship targets could be supplemented with real data to train these types of classifiers.

4.8 Discussion and Conclusion

Concerning the analysis presented in the previous sections, several observations can be made.

1. With only simulated SAR data, the accuracy is seen as a maximum for all the classifiers (almost 95%) in comparison to the case with the same number of real SAR targets. This is a first indication that the target classifiers can pick up inherent features for the six targets in all possible scene parameter variations from the simulated SAR images.
2. Prediction of real iceberg data with a simulated-data-trained classier (#1) is very much comparable to any data mix ratio (#2 to #8). This confirms the utility and compatibility of simulated SAR data of icebergs for use in this machine learning application.
3. With the progressive mixing of real and simulated SAR data, the 'average absolute change in accuracy' fluctuates between 0.6% to 2.7%. This indicates that the combination of simulated and real data in a single dataset is comparable to the accuracy with real SAR data alone with only minor fluctuation.
4. With #1 and #2 data set, the levels of accuracy are very comparable and the patterns are very similar. This is another indication that the simulated SAR data are compatible with real SAR data within this specific application.

These observations are consistent with the authors' previous research (chapter 2 and 3) that showed the similarity of real SAR targets to simulated targets produced from an EM backscatter model. The simulated SAR data of icebergs was found capable of capturing intrinsic parameters as it was comparable to the real SAR images tested in the classifiers.

4.9 References

Duda, R. O., Hart, P. E., & Stork, D. G. (2012). *Pattern classification* John Wiley & Sons.

Jang, H., Kim, S., & Lam, T. (2017). *Kaggle competitions: Author identification & statoil/C-CORE iceberg classifier challenge.* (). Bloomington, IN, USA: School of Informatics, Computing, and Engineering Indiana University. Retrieved from http://hankyujang.com/Papers/Final_project_paper.pdf

Jun, L., Atharva, P., & Dhruv, S. (2017). Iceberg-ship classifier using SAR image maps.

Power, D., Howell, C., Dodge, K., Scibilia, F., Sagli, J. R., & Hall, R. (2018). Towards automation of satellite-based radar imagery for iceberg surveillance-machine learning of ship and iceberg discrimination. Paper presented at the *OTC Arctic Technology Conference*,

The MathWorks, I. (a). Fitcknn. Retrieved from https://www.mathworks.com/help/stats/fitcknn.html?searchHighlight=fitcknn&s_tid=doc_srchtitle

The MathWorks, I. (b). Fitcsvm. Retrieved from https://www.mathworks.com/help/stats/fitcsvm.html?s_tid=doc_ta

The MathWorks, I. (c). Fitctree. Retrieved from https://www.mathworks.com/help/stats/fitctree.html?searchHighlight=fitctree&s_tid=doc_srchtitle

The MathWorks, I. (d). Nprtool. Retrieved from https://www.mathworks.com/help/deeplearning/ref/nprtool.html?s_tid=doc_ta

Chapter 5 Conclusion

5.1 Summary

This thesis presents the development and validation of EM backscatter modelling of icebergs at C-band in an ocean environment. The research was segmented and progressed through three main steps as outlined in chapter 2, three and four.

Starting with chapter 2, an EM backscatter model of icebergs has been presented, addressing the modelling challenges at large incidence angle beam modes operating at C-band. Modelled backscatter from icebergs was compared with real backscatter in terms of radiometric properties. Given that the EM modelling tool, GRECOSAR, is limited to simulating single layer backscatter, the dielectric of the iceberg target was varied and set to mimic the melt water surface that produces SAR brightness that closely matched observed results. This was the first indication that the GRECOSAR models can accurately mimic a SAR image clip of a wet iceberg target in an ocean environment. Taking advantage of GRECOSAR, it was shown that the same target can vary in brightness and signature as it changes orientation with respect to radar look direction.

Chapter 3 expands on the EM backscatter modeling approach to smaller incidence angle beam modes. GRECOSAR was used to determine the complete scattering matrix (all four channels with phase), which can be used with polarimetric techniques to further analyse scattering mechanisms from the icebergs. The subsequent analysis of both the radiometric and polarimetric properties of the modelled backscatter showed significant promise when compared to observed results.

To supplement the GRECOSAR work, chapter 3 includes the description of a 2D multilayer backscattering model that was developed to include air-water and water-ice interfaces at the iceberg surface. This allowed for an analysis of the sensitivity of the presence of the melt layer and its thickness to the radar return. It was shown that as little as 0.1 mm of melt layer could result in significant surface backscattering, a fact which further endorses the melt layer assumption in chapter 2. Simulations were expanded to generate SAR returns

of iceberg targets in a multitude of ocean environments, including variable wind directions and speeds. Variations in target brightness and signature were observed with changes in wind direction and speed. In summary, chapters 2 and 3 successfully demonstrated the capability to model an iceberg target's SAR signature, radiometric properties, polarimetric properties and realistic backscattering phenomena sensitive to the varying beam modes, target geometry and variation in the surrounding ocean environment.

In chapter 4, the iceberg backscatter simulations were analysed in a holistic sense by passing the simulated SAR images to various machine learning algorithms in the context of a iceberg/ship classifier. This allowed for a myriad of model parameters to be used within the learning phase of the algorithm development. Simulated SAR data of the icebergs and ships were generated to include extensive ranges of scenarios covering varying target sizes, orientations, imaging modes and ocean environments. Classifier accuracy measures were comparable when trained and tested with real and simulated SAR data. This is an indication that the EM model is able to capture intrinsic and holistic properties of the iceberg in addition to the capabilities demonstrated in chapter 2 and three. This last point demonstrates the objective of the original research idea – to exploit the convenience of an EM model to generate many thousands of target image clips for use in deep learning applications.

5.2 Future Directions

Several recommendations can be made based on the research presented herein.

1. A more realistic representation of the iceberg-ocean interface is envisaged to reflect the dynamics of iceberg-ocean interaction.
2. Field work could be extended to capture 3D profiles of colder bergs near Greenland that do not have the same melt layer on the iceberg surface. Simulations can be developed to determine if the melt water surface condition holds for icebergs in any other geographical locations. This will confirm if GRECOSAR can be used to simulate iceberg backscatter irrespective of geographical locations. It might indicate that an alternative to GRECOSAR is necessary to properly simulate

multilayer backscatter. For example, the EM solver HFSS (high-frequency structure simulator) could be used with a SAR wrapper to facilitate this multilayer model.

3. A more extensive set of SAR data of icebergs/ships can be generated to include a larger span of beam modes, target rotations and ocean parameters to determine their effect on classifier accuracy.
4. Since there is an interest in determining the detectability of icebergs in sea ice, these type of simulations could be developed. Sea ice can be profiled and added to the 3D model of the iceberg in the simulation scene to generate EM backscatter of icebergs in a sea ice environment. This will help determine the different scattering mechanisms of targets in different scattering environments.
5. EM modelling could be used to determine the detection limits of SAR by generating simulations of a large variety of icebergs with different shapes and sizes. This could help determine if a particular shape of iceberg is more or less detectable and the exact size limit for detectability. Undetectable iceberg sizes can thus be determined for sets of environment and satellite parameters.

Bibliography

Akbari, V., & Brekke, C. (2018). Iceberg detection in open and ice-infested waters using C-band polarimetric synthetic aperture radar. *IEEE Transactions on Geoscience and Remote Sensing, 56*(1), 407-421.

Atteia, G., & Collins, M. J. (2013). On the use of compact polarimetry SAR for ship detection. *ISPRS Journal of Photogrammetry and Remote Sensing, 80*, 1-9.

Bigg, G. R., Wadley, M. R., Stevens, D. P., & Johnson, J. A. (1997). Modelling the dynamics and thermodynamics of icebergs. *Cold Regions Science and Technology, 26*(2), 113-135.

Brekke, C., & Anfinsen, S. N. (2011). Ship detection in ice-infested waters based on dual-polarization SAR imagery. *IEEE Geoscience and Remote Sensing Letters, 8*(3), 391-395.

C-CORE. (2012). *Analysis of single, dual and polarimetric synthetic aperture radar data for iceberg/ship detection and discrimination.* (No. R-08-090-673).C-CORE.

C-CORE. (2016). *DIR – ship and iceberg detection and discrimination with RCM in support of polar epsilon 2.* (No. R-15-113-1178).C-CORE.

Crisp, D. J. (2004). No title. *The State-of-the-Art in Ship Detection in Synthetic Aperture Radar Imagery,*

Currie, B. W., & Haykin, S. S. (1987). *Detection and classification of ice* Research Studies Press; Toronto: Wiley.

Denbina, M., & Collins, M. J. (2012). Iceberg detection using compact polarimetric synthetic aperture radar. *Atmosphere-Ocean, 50*(4), 437-446.

Dierking, W., & Wesche, C. (2014). C-band radar polarimetry—useful for detection of icebergs in sea ice? *IEEE Transactions on Geoscience and Remote Sensing, 52*(1), 25-37.

Geldsetzer, T., Arkett, M., Zagon, T., Charbonneau, F., Yackel, J. J., & Scharien, R. K. (2015). All-season compact-polarimetry C-band SAR observations of sea ice. *Canadian Journal of Remote Sensing, 41*(5), 485-504.

Gray, A. L., & Arsenault, L. D. (1991). Time-delayed reflections in L-band synthetic aperture radar imagery of icebergs. *IEEE Transactions on Geoscience and Remote Sensing, 29*(2), 284-291.

Haykin, S., Lewis, E. O., Raney, R. K., & Rossiter, J. R. (1994). *Remote sensing of sea ice and icebergs* John Wiley & Sons.

Howell, C. (2008). *Iceberg and ship detection and classification in single, dual and quad polarized synthetic aperture radar* (PhD).

Howell, C., Bobby, P., Power, D., Randell, C., & Parsons, L. (2012). Detecting icebergs in sea ice using dual polarized satellite radar imagery. Paper presented at the *10th Int'L Conference and Exhibition on Performance of Ships and Structures in Ice (ICETECH),*

Howell, C., Mills, J., Power, D., Youden, J., Dodge, K., Randell, C., . . . Flett, D. (2006). A multivariate approach to iceberg and ship classification in HH/HV ASAR data. Paper presented at the *Geoscience and Remote Sensing Symposium, 2006. IGARSS 2006. IEEE International Conference On,* 3583-3586.

Howell, C., Youden, J., Lane, K., Power, D., Randell, C., & Flett, D. (2004). Iceberg and ship discrimination with ENVISAT multipolarization ASAR. Paper presented at the *Geoscience and Remote Sensing Symposium, 2004. IGARSS'04. Proceedings. 2004 IEEE International, , 1*

Jun, L., Atharva, P., & Dhruv, S. (2017). Iceberg-ship classifier using SAR image maps.

Kim, J., Kim, D., Kim, S., & Hwang, B. (2011). Iceberg detection using full-polarimetric RADARSAT-2 SAR data in west antarctica. Paper presented at the *Synthetic Aperture Radar (APSAR), 2011 3rd International Asia-Pacific Conference On,* 1-4.

Liu, C., Vachon, P., & Geling, G. (2005). Improved ship detection with airborne polarimetric SAR data. *Canadian Journal of Remote Sensing, 31*(1), 122-131.

Liu, C., Vachon, P. W., English, R. A., & Sandirasegaram, N. (2010). No title. *Ship Detection using RADARSAT-2 Fine Quad Mode and Simulated Compact Polarimetry Data,*

Mahdianpari, M., Salehi, B., Mohammadimanesh, F., & Brisco, B. (2017). An assessment of simulated compact polarimetric SAR data for wetland classification using random forest algorithm. *Canadian Journal of Remote Sensing, 43*(5), 468-484.

Margarit, G., & Mallorqui, J. (2008). Discretization effects in sea surface simulation applied to ship classification studies. Paper presented at the *Proc. ESA of SEASAR Workshop, , 2*

Margarit, G., Mallorqui, J., & Fabregas, X. (2007). Ship classification performance in single-pass polarimetric SAR interferometry: Evaluation of the sea interaction. Paper presented at the *Proc. ESA of POLINSAR Workshop,*

Margarit, G., & Mallorquí, J. J. (2008). Study of sea clutter influence in ship classification algorithms based on polarimetric SAR inteferometry. Paper presented at the *Synthetic Aperture Radar (EUSAR), 2008 7th European Conference On,* 1-4.

Margarit, G., Mallorqui, J. J., & Fabregas, X. (2007). Single-pass polarimetric SAR interferometry for vessel classification. *IEEE Transactions on Geoscience and Remote Sensing, 45*(11), 3494-3502.

Margarit, G., Mallorqui, J. J., Fortuny-Guasch, J., & Lopez-Martinez, C. (2009). Exploitation of ship scattering in polarimetric SAR for an improved classification under high clutter conditions. *IEEE Transactions on Geoscience and Remote Sensing, 47*(4), 1224-1235.

Margarit, G., Mallorqui, J. J., & Lopez-Martinez, C. (2007). Grecosar, a SAR simulator for complex targets: Application to urban environments. Paper presented at the *Geoscience and Remote Sensing Symposium, 2007. IGARSS 2007. IEEE International,* 4160-4163.

Margarit, G., Mallorqui, J. J., Rius, J. M., & Sanz-Marcos, J. (2006). On the usage of GRECOSAR, an orbital polarimetric SAR simulator of complex targets, to vessel classification studies. *IEEE Transactions on Geoscience and Remote Sensing, 44*(12), 3517-3526.

Margarit, G., & Tabasco, A. (2011). Ship classification in single-pol SAR images based on fuzzy logic. *IEEE Transactions on Geoscience and Remote Sensing, 49*(8), 3129-3138.

Marino, A., & Hajnsek, I. (2012). Icebergs detection with TerraSAR-X data using a polarimetric notch filter. Paper presented at the *Geoscience and Remote Sensing Symposium (IGARSS), 2012 IEEE International*, 3273-3276.

Marino, A., & Walker, N. (2011). Ship detection with quad polarimetric TerraSAR-X data: An adaptive notch filter. Paper presented at the *Geoscience and Remote Sensing Symposium (IGARSS), 2011 IEEE International*, 245-248.

Marino, A., Walker, N., & Woodhouse, I. (2010). Ship detection with RADARSAT-2 quad-pol SAR data using a notch filter based on perturbation analysis. Paper presented at the *Geoscience and Remote Sensing Symposium (IGARSS), 2010 IEEE International*, 3704-3707.

McNairn, H., Homayouni, S., Hosseini, M., Powers, J., Beckett, K., & Parkinson, W. (2017). Compact polarimetric synthetic aperture radar for monitoring crop condition. Paper presented at the *2017 IEEE International Geoscience and Remote Sensing Symposium (IGARSS)*, 4358-4361.

Meyer, F., & Hinz, S. (2009). Automatic ship detection in space-borne SAR imagery. *Int.Arch.Photogram.Remote Sens.Spatial Inform.Sci*, *38*(1), 1682-1750.

Murthy, H., & Haykin, S. (1987). Bayesian classification of surface-based ice-radar images. *IEEE Journal of Oceanic Engineering*, *12*(3), 493-502.

Orlando, J. R., Mann, R., & Haykin, S. (1990). Classification of sea-ice images using a dual-polarized radar. *IEEE Journal of Oceanic Engineering*, *15*(3), 228-237.

Pastina, D., Fico, F., & Lombardo, P. (2011). Detection of ship targets in COSMO-SkyMed SAR images. Paper presented at the *Radar Conference (RADAR), 2011 IEEE*, 928-933.

Power, D., Bobby, P., Howell, C., Ralph, F., & Randell, C. (2011). State of the art in satellite surveillance of icebergs and sea ice. Paper presented at the *OTC Arctic Technology Conference,*

Power, D., Youden, J., Lane, K., Randell, C., & Flett, D. (2001). Iceberg detection capabilities of RADARSAT synthetic aperture radar. *Canadian Journal of Remote Sensing, 27*(5), 476-486.

Randell, C., Freeman, R., Power, D., & Stuckey, P. (2009). SS: Canadian: Atlantic development; technological advances to assess, manage and reduce ice risk in northern developments. Paper presented at the *Offshore Technology Conference,*

Shirvany, R., Chabert, M., & Tourneret, J. (2012). Ship and oil-spill detection using the degree of polarization in linear and hybrid/compact dual-pol SAR. *IEEE Journal of Selected Topics in Applied Earth Observations and Remote Sensing, 5*(3), 885-892.

Tello, M., López-Martínez, C., Mallorquí, J. J., & Greidanus, H. (2005). A novel algorithm for ship detection in envisat SAR imagery based on the wavelet transform. Paper presented at the *Envisat & ERS Symposium, , 572*

Touzi, R., Charbonneau, F., Hawkins, R., & Vachon, P. (2004). Ship detection and characterization using polarimetric SAR. *Canadian Journal of Remote Sensing, 30*(3), 552-559.

Ulaby, F. T., Long, D. G., Blackwell, W. J., Elachi, C., Fung, A. K., Ruf, C., . . . Van Zyl, J. (2014). *Microwave radar and radiometric remote sensing* University of Michigan Press Ann Arbor.

Vachon, P. W., & Wolfe, J. (2011). C-band cross-polarization wind speed retrieval. *IEEE Geoscience and Remote Sensing Letters, 8*(3), 456-459.

Vachon, P., Campbell, J., Bjerkelund, C., Dobson, F., & Rey, M. (1997). Ship detection by the RADARSAT SAR: Validation of detection model predictions. *Canadian Journal of Remote Sensing, 23*(1), 48-59.

Wang, Y., Li, H., Zhang, Y., & Guo, L. (2015). Marine target detection in quad-pol synthetic aperture radar imagery based on the relative phase of cross-polarized channels. *Journal of Applied Remote Sensing, 9*(1), 096092.

Wesche, C., & Dierking, W. (2012). Iceberg signatures and detection in SAR images in two test regions of the weddell sea, antarctica. *Journal of Glaciology, 58*(208), 325-339.

Yin, J., Yang, J., & Zhang, X. (2011). On the ship detection performance with compact polarimetry. Paper presented at the *Radar Conference (RADAR), 2011 IEEE,* 675-680.

Yin, J., Yang, J., Zhou, Z., & Song, J. (2014). The extended bragg scattering model-based method for ship and oil-spill observation using compact polarimetric SAR. *IEEE Journal of Selected Topics in Applied Earth Observations and Remote Sensing, 8*(8), 3760-3772.

Appendix

A. MATLAB Code to Generate 2D Backscatter Model of Iceberg

```
clc
clf
clear
close all

%% script to compute back-scatter contribution from two-layered IB model
% sig0=sig0_ws+sig0_is+sig0_ss+sig0_iv------ws=water surface, iv=ice volume
% ---------------------------
% water |
%---------------------------
% ice (with air bubble)|
%---------------------------
% sea-water |
%---------------------------
%% common parameters
fc=5.4e9;
theta_air=linspace(10,60,60); % incident angle in (degree)
thickness_w=1*.001; % in (mm)----assumption
thickness_ib=30*1; % in (m)----assumption

% air bubble density calculation
```

```
d_by_dice=.5; % gray et al. d/dice=.5, .8, .9 and .95
radius_air_bubble=1e-3; % air bubble radius (mm) Laurence gray et al. 1991
(greenland--1mm)/in dierking et al. .15-.25 mm (antartica)
N_air_bubble=(3/4/pi/radius_air_bubble^3)*(1-d_by_dice) % /m3
rms_height_w=1.5*.001; % rms height of water surface (mm)------partington et.
al--1.5 mm
corr_length_w=8*.01; % corr. length of water surface (cm)------partington et.
al--8 cm
weight_rms_height_sea=1; %
weight_corr_length_sea=1; %
rms_height_sea=weight_rms_height_sea*rms_height_w; % rms height of water
surface (mm)
corr_length_sea=weight_corr_length_sea*corr_length_w; % corr. length of water
surface (cm)
rms_height_i=rms_height_w; % rms height of water surface (mm)
corr_length_i=corr_length_w; % corr. length of water surface (cm)
vol_air_bubble=(4/3)*pi*radius_air_bubble^3*N_air_bubble; % volume fraction
of air bubbles

% water dielectric constant
e_water=my_seawater_permittivity(0,fc./1e9,0); %(T,fc,S)
% e_water=3-1i*.1;
er_water=real(e_water);
eim_water=-imag(e_water);
ep_a=1; % air
lamda_air=3e8/fc;
k_air=(2*pi/lamda_air);
k_water=k_air*sqrt(er_water);
n_air=sqrt(ep_a);
n_water=sqrt(e_water);
theta_water=my_snellslaw(theta_air,er_water,eim_water,fc);
ke_water=-2*k_air*imag(sqrt(e_water));

k_water*rms_height_w;
k_water*corr_length_w;

% reflection/transmission coefficient calculation-----air/water
[R_horizontal_a_to_w,R_vertical_a_to_w,R_horizontal_w_to_a,R_vertical_w_to_a,
T_horizontal_a_to_w,T_vertical_a_to_w,T_horizontal_w_to_a,T_vertical_w_to_a]=
my_my_reflection_transmission(theta_air,theta_water,n_air,n_water);
% figure
%
plot(theta_air,abs(R_horizontal_a_to_w),theta_air,abs(R_vertical_a_to_w),'r')
% legend('h','v')
% back-scatter from------ air-ice interface
W_water_gauss=(2*pi*corr_length_w.^2)./(1+corr_length_w.^2.*(2*k_air.*sind(th
eta_air)).^2).^1.5; % komarov 2017 pp-5705
%
W_water_exp=4*corr_length_w.^2./(1+corr_length_w.^2.*k_air.^2.*sind(theta_air
).^2.*(1)^2).^2;
sigma0_vv_ws=8.*k_air.^4.*rms_height_w.^2.*abs(R_vertical_a_to_w.*cosd(theta_
air).^2+sind(theta_air).^2.*(1+R_vertical_a_to_w).^2*.5.*(1-
(ep_a/e_water))).^2.*W_water_gauss;

sigma0_hh_ws=8*k_air.^4.*rms_height_w.^2.*abs(R_horizontal_a_to_w.*cosd(theta
_air).^2).^2.*W_water_gauss;
```

```
% plot(theta_air,10.*log10(sigma0_vv_ws),'r')
% legend('hh','vv')

% %%%%%%%%%%%%%%%
% iceberg dielectric constant
e_i_re=3.15; % gray et al--IEEE TGRSS-1991
losstangent=2e-3; % haykin
e_i_im=e_i_re * losstangent;
e_ice=e_i_re-1i*e_i_im;
vi=vol_air_bubble; % volume inclusion of air bubble in ice
e_iceberg=e_ice+3*vi*e_ice*((ep_a-e_ice)/(ep_a+2*e_ice)); % ulaby---pp-131
k_ice=k_air*sqrt(real(e_iceberg));
n_ice=sqrt(e_iceberg);
theta_ice=my_snellslaw(theta_water,real(e_iceberg),imag(e_iceberg),fc);
% %
E_i=ep_a/e_ice; % ulaby pp-474
K_ice=(E_i-1)/(E_i+2); % ulaby pp-474
ka_iceberg=3*vol_air_bubble*k_ice*imag(E_i)/(abs(E_i+2))^2; % ulaby pp-474
ks_iceberg=2*vol_air_bubble*k_ice^4*radius_air_bubble^3*(abs(K_ice))^2; %
ulaby pp-474
ke_iceberg=ka_iceberg+ks_iceberg;
% %
% reflection/transmission coefficient-------- water-ice
[R_horizontal_w_to_i,R_vertical_w_to_i,R_horizontal_i_to_w,R_vertical_i_to_w,
T_horizontal_w_to_i,T_vertical_w_to_i,T_horizontal_i_to_w,T_vertical_i_to_w]=
my_my_reflection_transmission(theta_water,theta_ice,n_water,n_ice);
% % correlation spectrum--ice
W_ice_gauss=(2*pi*corr_length_i.^2)./(1+corr_length_i.^2.*(2*k_water.*sind(th
eta_water)).^2).^1.5; % komarov 2017 pp-5705
%
sigma0_vv_is1=8.*k_ice.^4.*rms_height_i.^2.*abs(R_vertical_w_to_i.*cosd(theta
_water).^2+sind(theta_water).^2.*(1+R_vertical_w_to_i).^2*.5.*(1-
(e_water/e_ice))).^2.*W_ice_gauss;
sigma0_hh_is1=8*k_ice.^4.*rms_height_i.^2.*abs(R_horizontal_w_to_i.*cosd(thet
a_water).^2).^2.*W_ice_gauss;

% %
sigma0_vv_is=sigma0_vv_is1.*T_vertical_a_to_w.*T_vertical_w_to_a.*exp(-
2*ke_water*thickness_w./cosd(theta_water));
sigma0_hh_is=sigma0_hh_is1.*T_horizontal_a_to_w.*T_horizontal_w_to_a.*exp(-
2*ke_water*thickness_w./cosd(theta_water));


%% volume scattering in IB
% % f_iva=4*(2*pi*radius_air_bubble/lamda_air)^4*(abs(K_ice))^2;
rho_m=10; % range-ambiguous distance
sig0_vol=N_air_bubble*4*pi*radius_air_bubble^6.*k_air.^4.*(abs(K_ice)).^2*rho
_m;

sigma0_vv_iv=...

sig0_vol.*T_vertical_i_to_w.*T_vertical_w_to_i.*T_vertical_a_to_w.*T_vertical
_w_to_a...
```

```
 .*((1-exp(-
2*ke_iceberg*thickness_ib./cosd(theta_ice))).(2*ke_iceberg*thickness_ib./cos
d(theta_ice)))...
 .*(exp(-2*ke_water*thickness_w./cosd(theta_water)));
sigma0_hh_iv=...

sig0_vol.*T_horizontal_i_to_w.*T_horizontal_w_to_i.*T_horizontal_a_to_w.*T_ho
rizontal_w_to_a...
 .*((1-exp(-
2*ke_iceberg*thickness_ib./cosd(theta_ice))).(2*ke_iceberg*thickness_ib./cos
d(theta_ice)))...
 .*(exp(-2*ke_water*thickness_w./cosd(theta_water)));


%% scattering from IB-sea interface
e_sea=my_seawater_permittivity(5,fc/1e9,35); %(T,fc,S)
er_sea=real(e_sea);
eim_sea=-imag(e_sea);
k_sea=k_air*sqrt(er_sea);
n_sea=sqrt(e_sea);
theta_sea=my_snellslaw(theta_ice,er_sea,eim_sea,fc);

% reflection/transmission coefficient ice-sea
[R_horizontal_i_to_s,R_vertical_i_to_s,R_horizontal_s_to_i,R_vertical_s_to_i,
...

T_horizontal_i_to_s,T_vertical_i_to_s,T_horizontal_s_to_i,T_vertical_s_to_i]=
...
 my_my_reflection_transmission(theta_ice,theta_sea,n_ice,n_sea);
% % correlation spectrum--ice
W_sea_gauss=(2*pi*corr_length_sea.^2)./(1+corr_length_sea.^2.*(2*k_ice.*sind(
theta_ice)).^2).^1.5; % komarov 2017 pp-5705
%
sigma0_vv_ss1=8.*k_ice.^4.*rms_height_sea.^2.*abs(R_vertical_i_to_s.*cosd(the
ta_ice).^2 ...
 +sind(theta_ice).^2.*(1+R_vertical_i_to_s).^2*.5.*(1-
(e_iceberg/e_sea))).^2.*W_sea_gauss;
sigma0_hh_ss1=8*k_ice.^4.*rms_height_sea.^2.*abs(R_horizontal_i_to_s.*cosd(th
eta_ice).^2).^2.*W_sea_gauss;
%
sigma0_vv_ss=sigma0_vv_ss1.*T_vertical_a_to_w.*T_vertical_w_to_a.*T_vertical_
w_to_i.*T_vertical_i_to_w.*...
 exp(-2*ke_water*thickness_w./cosd(theta_water)).*exp(-
2*ke_iceberg*thickness_ib./cosd(theta_ice));
sigma0_hh_ss=sigma0_hh_ss1.*T_horizontal_a_to_w.*T_horizontal_w_to_a.*T_horiz
ontal_w_to_i.*T_horizontal_i_to_w.*...
 exp(-2*ke_water*thickness_w./cosd(theta_water)).*exp(-
2*ke_iceberg*thickness_ib./cosd(theta_ice));

 %% plot
figure
plot(theta_air,10.*log10(sigma0_hh_ws),'b1')
hold on
plot(theta_air,10.*log10(sigma0_hh_is))
hold on
plot(theta_air,10.*log10(sigma0_hh_iv),'c')
```

```
hold on
plot(theta_air,10.*log10(sigma0_hh_ss),'g')
hold on
total=10.*log10(sigma0_hh_ws+sigma0_hh_is+sigma0_hh_iv+sigma0_hh_ss);
plot(theta_air,total)

xlabel('incident angle (\circ)')
ylabel('\sigma_0 (dB)')
legend('surface (water)','surface (ice)','volume (ice)','surface
(sea)','total')
title('HH')
%
```